ESA Living Planet Fellowship: ICEFLOW
Short term movements in the Cryosphere

final report
4000125560 18 I-NS

Bas Altena

ESA contract number:	4000125560 18 I-NS
date	June 19, 2020
project period	Feb. 2018 - Feb. 2020
period update	Dec. 2018 - Feb. 2020
authors	Bas Altena, Andreas Kääb
UIO website	mn.uio.no/geo/english/research/projects/iceflow/index.html
ESA website	eo4society.esa.int/projects/iceflow-short-term-movements-in-the-cryosphere/

Project abstract

The cryosphere is changing at a rapid pace, and at the same time Earth observation is revolutionized through lower thresholds for space access. Consequently, it is only recently that constellations and fleets of Earth observation platforms sense the cryosphere with both very high spatial and temporal resolution. Opportunities arise from the broken barrier to space and nowadays big volumes of data are acquired. One overlooked aspect is the **opportunities that exist within multi-mission data** to enhance information extraction. Therefore we want to **highlight the potential of short-term Earth observation** for cryospheric applications by combining different satellite systems. Consecutive satellite overpasses make it possible to analyse moving objects, on glaciers, sea ice, ice bergs and river ice. This is of importance for maritime management in the Arctic, and flood mitigation for Northern communities. These case studies are **a billboard for future applications**, where even more temporal data will be available, and movement information will be a key source of information, next to current analysis tools like classification and change detection.

Contents

Research activities performed during the project

task 1 Glacier ice

Land-terminating mountain glaciers react for the most passively to climate change and are therefore an ideal terrestrial indicator for climate change. While the Sentinel-1 SAR constellation is at operational level for the icesheet velocity products its use in high-mountain glaciers is not optimal. For this case optical satellites can be used, correlating two images from different times to get planar displacements. However, due to its pairwise matching, a large unstructured dataset is constructed. Post-processing of this patchwork of velocity fields is part of this working package.

task 1.1 High-resolution glacier flow time-series

Figure 1: Seeds following the temporally evolving glacier flow occuring at the Chugach mountain range, Alaska.

Synthesizing velocity fields A robust post-processing scheme has been implemented, and during the project period this work has been published in "the Cryopshere" journal. This methods is able to produce a reliable and consistent time-series with regular spacing in space and time of 300 by 300 meters at an resolution of 32 days. The velocity fields used are the freely available GoLIVE dataset, which is based on Landsat 8. However, the methodology is independent of sensor, so can be implemented with the sentinels.

SciHub downloadtool In order to extract large volumes of data from the Sentinel archive an efficient download tool had to be set into place, this was done by us. A similar batch procedures is available for Python (link), but now also for a matlab environment.

GoLIVE for Sentinel-2 & RapidEye GoLIVE is the portal for Landsat 8 velocity data is available. A similar pipeline is developed for Landsat 7, Sentinel-2 and RapidEye in this project. This includes an automatic downloading and geo-referencing procedure.

Third-party sensor integration It was envisioned to include more velocity fields from different sattelites. For example, the Indian satellites have acquired imagery over the Alaskan mountains. Several scenes were selected, and an offical proposal was made and submitted to the ESA third part mission program, to get access to this data. Unfortunately, the proposal was rejected.

Glacier icefall velocities High repeat observations of Sentinel-2 make it possible to look at weekly flow changes. Our previous work explored this potential, through the Spot5 Take 5 campaign, but was limited to the dominant flow direction. However, with the build-up of data from Sentinel-2 other techniques become possible. One of these is to use time-for-space with image matching, this makes it possible to get higher resolution velocity fields, by the use of matching multiple imagery at the same time.

An application to use this technique, is the flow calculation through ice falls. Glacier length is a common indicator of local climate, but similarly this is can also be the case for icefalls. As the ice flux going through is funneled, makes the ice velocity fast and therfor very sensitive. Hence, developing this technique and making it operational gives glaciologist another tool to assess glacier change. Currently, the downloading tool is working in full swing and ice fall velocities are estimated automatically. For this to work an automatic cloud detection algorithm had to be developed, as elevation models are imprecise in this high mountain terrain, and snow cover is abundant.

Figure 2: Mount Everest and Lhotse mountain at night. In the center a glowing line is present, this stems from climbers with torches. They move through the ice fall along a predefined path with fixed ropes. The picture is taken by Eric Draft.

Finally, the ice fall of Khumbu glacier was taken as an example. A climbing route goes through this ice fall to climb Mount Everest from the Nepali side. Because of its popularity, ropes and ladders are fixed over crevasses and ice walls, marking a pre-defined route. This path is also beautifully illustrated in Figure 2. Because, this route is fixed, the climbing route will change its possition, as time progresses and glacier ice flows. Hence, the trajectory of a climber is recorded with satellite navigation, the glacier velocity can be extracted from a round trip to Mount Everest.

In order to acquire positioning data from high altitude mountaineers, a series a e-mails has been send out to mountain guides, professional high altitude climbers, Nepali travel agencies etc. Eventually, some data was provided and used in the study as validation.

Short-term glacier velocities and elevation change Sentinel-2 has a wide swath width and high repeat. Its converging orbits at the poles result in increased acquisiting over high latitudes and the Arctic. For example, in Svalbard a point can be seen from multiple orbits, while this is only a single orbit at the equator. This increased sampling can be exploited to simulataniously extract velocity (from time difference) and elevation change (from different acquistion geometry).

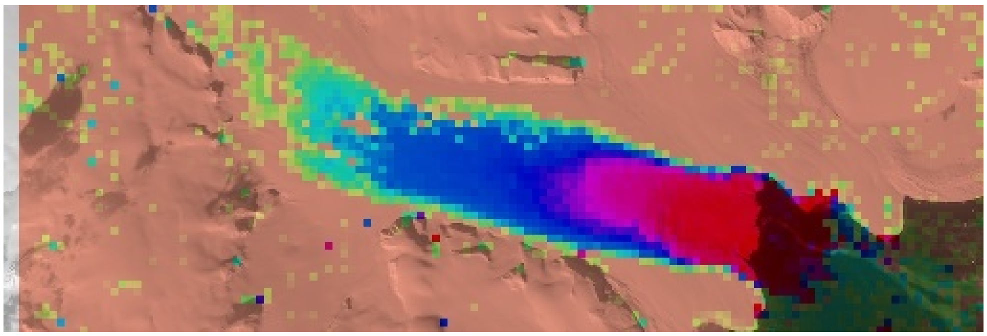

Figure 3: Glacier speed in colours of the surging glacier of Negribreen.

As a demonstration of this potential, velocity fields from different orbits were calculated. These were integrated into a model estimation, where the temporal and geometrical parameters were distangled. The glacier under study is Negribreen, a surging glacier on the peninsula of Spitsbergen. This glacier has accelarated noticably since the launch of Sentinel-2. However, due to the polar night, the observation excludes this period. Nonetheless, its evolution can be observed at a resolution of two weeks, giving information both about the velocity and the mass-transfer. This was Published in the ISPRS Annals of Photogrammetry and Remote Sensing, and a more elaboratiev study is work in progress.

task 1.2 Long-term glacier dynamics from archived data

Reproducing time-series An effort has been made to reproduce a study based on archieved Landsat imagery. However, during the project period the archive of Landsat has been re-processed and transferred to a tier-structure. Consequently, some time has been put in alligning the old scene-ID to the new structure of product-IDs, as the scene-IDs are not queriable in the typical USGS earthexplorer portal. However, this code is now available on the Mathworks file exchange.

In addition, the metadata structure and archive of Landsat has changed as well. Nonetheless, this off-line repository is of great value for querying. A similar database would be helpfull to have for the Sentinel-2 system as well, as currently online querrying is the only option.

State-of-the-art image matching CosiCorr is the *de facto* procedure for image matching and this methodology is superior over other methods. However, the algorithm was implemented within a closed software package, now this is re-written by us and build into our own pipeline. This makes it possible to adjust freely and improve upon.

task 2 Fjord ice

The circulation within fjords is depended on several forces. Short term-forces as wind occur, as well as, circulation of ocean currents, and fresh and salt water interaction due to ice berg melt. On a seasonal scale melt water from the glaciers and icesheet interfere. The icebergs function as tracers as they are influenced by the intermediate current, while the drift sea ice reacts to the surface current. And in order to see the influence of all these components, the velocity fields throughout different seasons are constructed. This makes it possible for the first time to look at the influence of these components within the fjord system on such a large-scale with ultra-high resolution.

Figure 4: Fjord ice and ice bergs in Semerlik fjord, Greenland.

A methodology was developed to extract and decompose iceberg and fjord ice velocity from Sentinel-2 and PlanetScope imagery. This approach was applied over the full stretch of Semerlikfjord, which is over 100 kilometers long, while the resolution of the velocity was at 300 meters. These results were presented during AGU, highlighted by Landsat Science and at the Living Planet webpage. More development into this direction is ongoing, as Bas Altena works as a postdoc situated at the institute or marine and atmospheric research, Utrecht university.

task 3 River ice

Discharge in Arctic rivers is not only depended on snow melt, but is influenced by land cover and permafrost changes. 30% of these rivers are not gauged in-situ, while for the others uncertainty exists about their measurement quality. Fortunately, rivers can be gauged through stage measurements with spaceborne altimeters. However, for high flow it might be more precise to use velocity estimates of broken river-ice to infer discharge. This working package explores the use of velocity time-series of river ice to calibrate hydrological modelling on basin scale.

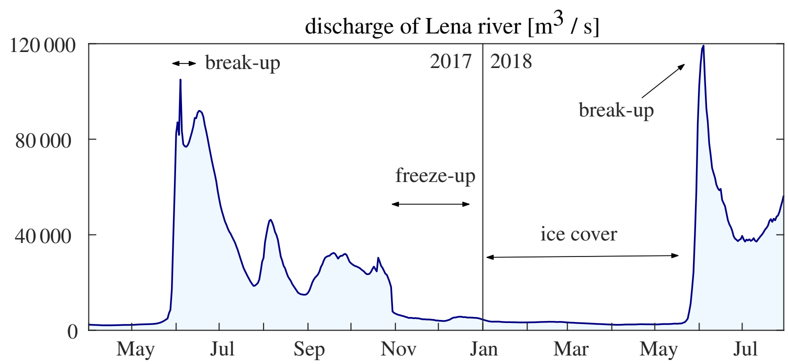

Figure 5: Discharge estimates from gauging station along Lena river, data from Arctic Great Rivers Observatory.

For the demonstration of potential new techniques, we use the Lena river as test bed. In figure 5 a hydrograph is shown from one of the gauging stations along this river. In here, different regimes can be clearly identified. The figures starts with a situation of ice cover and low discharge. Then when June starts a large peak peak discharge occurs, which is mostly accompanied by ice break-up. Discharge slowly decays and when November starts discharge lowers and a period of freeze-up starts. Tyically, in January the whole river cover is frozen over and the seasonal cycle repeats. This working package, is divided in two subjects depended on the season, the break-up and the freeze-up. Both subtasks are different processes, but also different satellite systems are combined.

task 3.1 Break-up

Every spring the potential of mechanical river ice break-up and associated ice-runs and flooding poses a thread to communities at Northern latitudes. For these long and remote Arctic rivers monitoring and mitigation efforts are possible but logistically complex. However, in recent years monitoring programs have emerged based on spaceborne sensors that sense large parts of the Earth surface with short and at a regular interval. All have a similar sun-synchronous orbit, and have thus a similar ground track. This results in near-simultaneous optical acquisitions, which make it possible to monitor displacements at or near the Earth surface. Hence, by combining multiple monitoring programs it is possible to generate a new service; one for monitoring river ice movement. In this sub-task we demonstrate the feasibility of such a service by combining data from freely available data of Sentinel-2 and Proba-V. The ice floe velocities during spring 2016 are estimated over a more than 700 kilometer long stretch of the Lena River in Russia (see Figure 6).

The implemented pipeline is fully automatic, making use of a global river map product. However, the data is coming from two different sub-systems; the Copernicus system and the virtual environment of VITO. Both systems are not coupled, so off line processing was done. However, the study shows the potential of combining multiple satellites, and even the geometric potential of coarse resolution satellites. A manuscript is ready for submission on this work. This work is written into a manuscript and is almost ready for submission, we envision to submit this work in the near future.

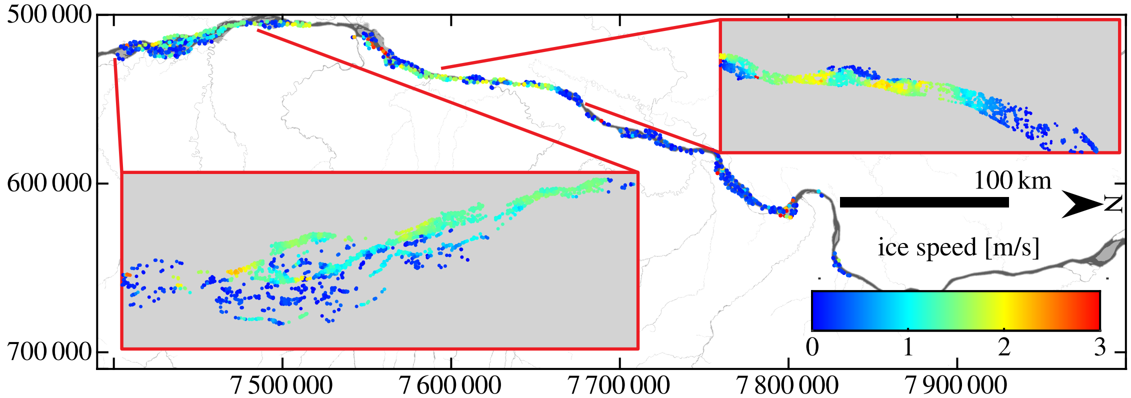

Figure 6: River ice velocity on the 25th of May over the northern stretch of Lena river, Russia.

task 3.2 Freeze-up

During freeze-up the water temperature lowers, thus becoming less viscous. Additionally, at the interface with the atmosphere ice particles are formed and mixed through a large part of the water column, helped by turbulence. Through contact with other ice particles, merging and growing is possible, eventually resulting in a size big enough to overcome the turbulent force through their buoyancy. These ice floes are growing further as they flow along on top of the river, accumulating and organizing each other side by side. However, movement will halt when 80-90% of the free surface is covered with pans, and there touching parts will form a stagnant ice cover. But water is still flowing through the river, when velocity is slow juxtaposition of ice floes will grow the ice cover up-stream. However, when the water flow velocity is significant, the forces on the pans at the edge are pushed under the ice cover. These floes travel further underneath the forming ice cover, eventually halting and cause additional thickening. When velocities stay high, this mechanism is able to construct a “hanging dam” underneath the ice cover.

Hanging dams can be a serious thread, during the melting season, these sections are the latest to melt away. Hence, the location of these dams is of interest for mitigation measures, however they are invisible from the surface. But if the flow regime , and especially the maximum velocity, of the freeze-up period is analyzed, there might be clues extractable.

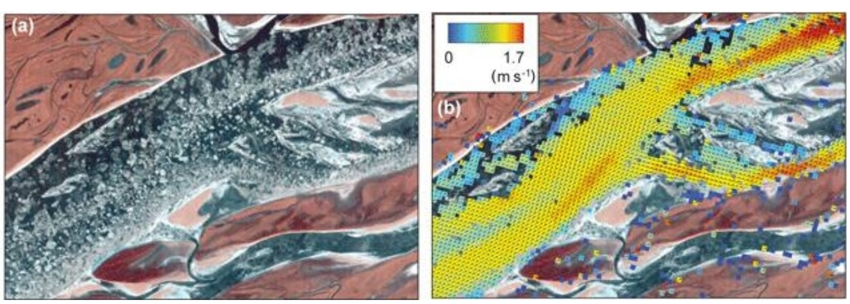

Figure 7: River ice velocity on the 1st of November 2016 over the Amur river, Russia.

The article published during this project shows the potential of the Planet constellation to derive such datasets. Differences in break-up and freeze-up situations are highighted and assesed. An example of such a product is shown in Figure 7.

task 4 Outreach

During the project period, I continued to be active with reviewing, blogging, tweeting and even won a ESA EO's "Where on Earth" challenge.

task 4.1 Cross-over tool

Near-simultaneous acquisitions of spaceborne imagery from satellites can be used to extract movement of large scale dynamic natural phenomena at or above the Earth's surface. However, such acquisition pairs are in essence composed from multiple platforms. Because of different ownership of satellites, the discoverability of data to generate such products is limited. Hence to enhance this type of data through pairing, we have developed a toolbox that tries to find satellite overpasses in time and space. For a given region of interest and satellite combination(s) the orbital configuration is estimated for a set timespan. When a potential overpass is coming or has occurred, this will be listed.

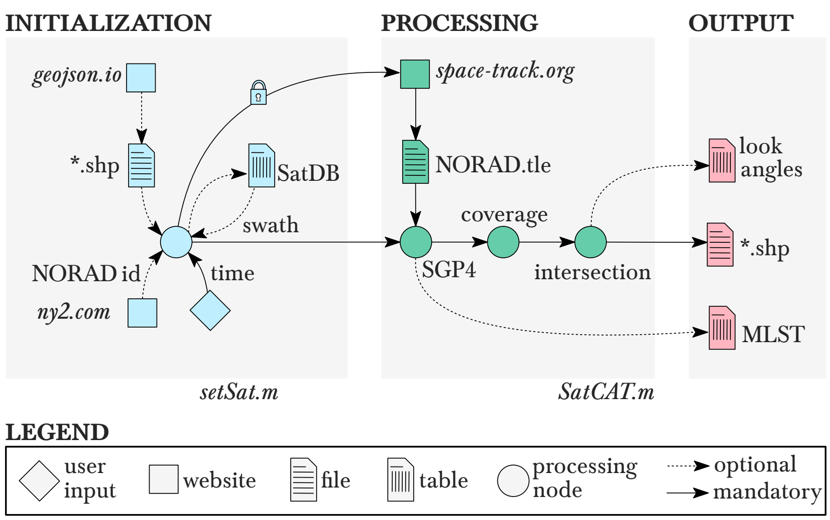

Figure 8: Schematic overview of the Satellite overpass toolbox.

The routine makes use of the satellite tracking catalog, so atmospheric drag or maneuvers are accounted for. A high level workflow is shown in Figure 8. However, an update was made to SGP4 during the project period. This module is the backbone of the processing chain. This update encompassed a whole new structure, resolving into a re-rewriting of the whole toolbox too, which is thus still work in progress.

task 4.2 Other short-term movements - Palu earthquake

On 28 September 2018 an earthquake occurred right outside of the coast at Sulawesi island, Indonesia. It resolved in a rift and a devastating tsunami. Optical satellites can be a great means to estimate vast displacements, especially within build-up terrain, such as the city of Palu. In these palces, inSAR looses coherence, thus optical sensors can complement such data. Unfortuneatly, the Sentinel-2 system had just acquired a day before the earthquake, and due to the low latitude of Indonesia, a total of five days had to be waited upon before another overflight was possible. Fortunately, the Planet constellation was able to sense at the same day as the earthquake. Hence, we used this data to extract a displacement field over the area of Palu (Figure 9).

The importance of this data is mostly found in disaster relief, as the value of the data is enormous right after the event. We where able to communicate our results to disaster relief, which in this way were able to get an idea of the scope of disaster. However, the results in Figure 9 showcast two different disasters. On the one hand the rift is clearly visible,

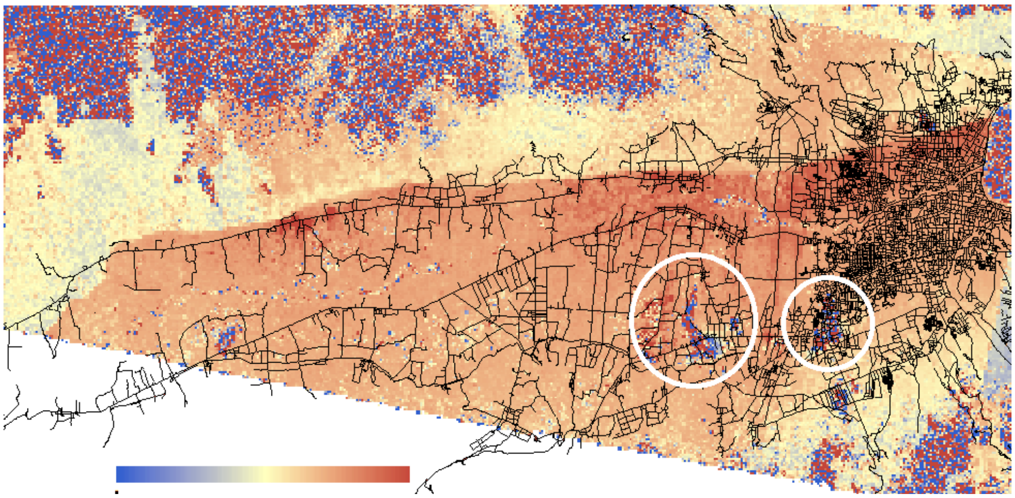

Figure 9: Surface displacement of Palu Earthquake, based upon PlanetScope imagery. The colorbar extents from +10 to -10 meters in North-South direction and the landslides are highlighted by the white circles.

while coherence loss occurs at two different sites. These were landslides triggered by the earthquake and its mapping through our results where crucial for disaster relief.

task 4.3 Other short-term acquisitions - topography from different time-of-day

An exploratory study was conducted, and a manuscript can be found in the Annex. A small summary is given below. Nowadays the amount of satellites with high-resolution optical sensors has increased considerably. Most of these satellites are situated in a Sun-synchronous orbit and pass over around local noon. In recent years single constellations have been set into orbit to acquire daily on a global scale. To increase the revisit rate further, it can be expected that other orbits will be used to acquire imagery at different time of the day. Such data has many potential applications, of which topographic extraction can be of interest for image interpretation. In this sub-task we explored the feasibility of topographic extraction, through cast shadow at different times of the day. This is possible by combining data from current satellite constellations, or in the near-future from single commercial endeavors (e.g.: BlackSky, DigitalGlobe). The technique is similar to visual hull or shape-from-silhouette, a technique well established in computer vision, but now finding an application in Earth observation. Topographic opportunities of the kind we present in this Annex are commonly overlooked by the remote sensing community, but this niche might spark new real-world applications.

task 5 CopernicusDEM

Since the start of 2020, the CopernicusDEM has been released, this is a global elevation product, which is now used in the Sentinel-2 processor. This product is based upon the TanDEM-X elevation product, where manual checking was conducted, and holes were filled with ASTER GDEM or SRTM data products. Three different products are available at three different resolutions (10, 30 and 90 meters). The highest resolution is used for the orthorectification of Sentinel-2 data, while the 90 meter products is freely available.

The geometric quality of Sentinel-2 is diretly related to this issue, especially for high mountain terrain with steep slopes. A first aspect is related incorrect elevation representation, that propagate into such pushbroom imagery, see Figure 10. This results in displacement of pixels in across-track direction of the orbital path. When differences exist between the terrain and the elevation dataset, an orthorectified image will have an incorrect absolute geo-referencing.

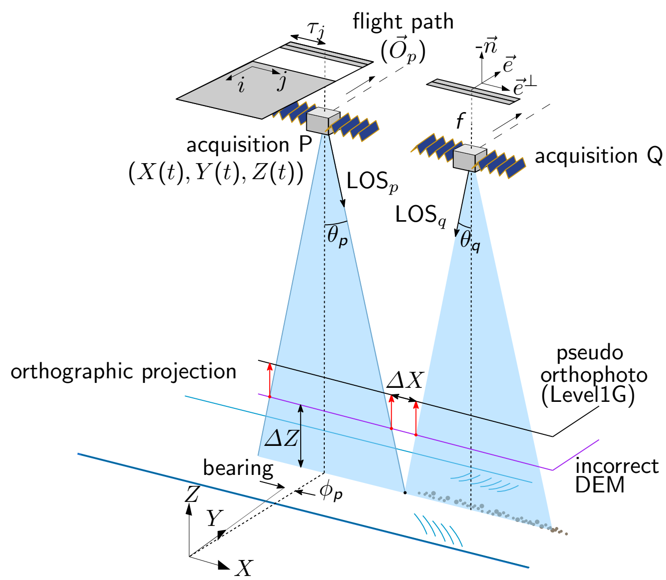

Figure 10: Schematic of orthorectifaction errors due to off-date elevation model, from Altena & Kääb.

Thus land mapping products or other delineations, might have such systematic biasses within.

A second component, that can corrupt the geometric quality are deviations in the flight path location of the satellite. Currently, the satellite localization and viewing angles are estimated by the startrackers and GNSS instrumentation onboard. Resulting in along track errors deviating ± 10 meters, especially for Sentinel-2B. Such errors, propagate into the orthorectifacated product, but these are minimal, and are most significant on steep terrain. For both errors, the viewing angle of the instrument is of importance, where these effects are minimal in the nadir direction and largest at the edge of the imagery.

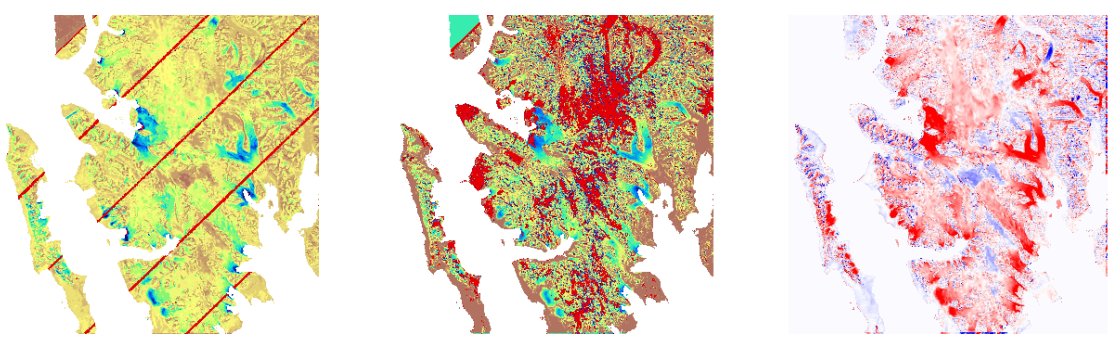

(a) displacement (b) along track displacement (c) DEM elevation change

The new CopernicusDEM, does reduce the absolute georeferencing errors within an orthorectified image, in respect to the former elevation model (which was closed). In Figure 11a the displacement between two orthorectified imagery, with different elevation models are shown. These, strongly correlate with the displacements observed between imagery from the same day, but different orbits, (shown in Figure 11b). This signal is very strong, as the PlanetDEM used an outdated elevation model (from the 1980s), and significant elevation change has occured on Svalbard. Another benefit, is the open data structure of the CopernicusDEM. This gives the possibility to reverse engineer elevation change, or calculate corrections of acquisitions. In this way, the absolute georeferencing can be improved, for exmaple when elevation has changed significantly in respect to the CopernicusDEM time span.

Action item status list

Research publications

[under submission] River ice movement through a combination of European satellite monitoring services.
Altena & Kääb, International journal of applied Earth observation & geoinformation.

[under review] Ensemble matching: measuring ice flow from repeat satellite images over fast-changing glacier parts. Demonstration for Khumbu icefall, Mount Everest.
Altena & Kääb, Journal of glaciology.

[accepted] From high friction zone to frontal collapse: dynamics of an ongoing tidewater glacier surge, Negribreen, Svalbard.
Haga, McNabb, Nuth, Altena, Schellenberger & Kääb, Journal of glaciology.

[minor revisions] On the possibility of a 1000 km long subglacial river or wet sediment flow under the north Greenland ice sheet.
Chambers, Greve, Altena & Lefeuvre, The crysosphere.

[published] River-ice and water velocities using the Planet optical cubesat constellation.
Kääb, Altena & Mascaro, Hydrology and Earth system sciences.

[published] Observing the ice of our planet with daily cubesat imagery
Altena, Proceedings of the Innsbruck summer school of Alpine research.

[published] Monitoring sub-weekly evolution of surface velocity and elevation for a high-latitude surging glacier using Sentinel-2
Altena, Haga, Nuth & Kääb, ISPRS archives of photogrammetry, remote sensing and spatial information sciences.

[published] Closing the mass budget of a tidewater glacier: the example of Kronebreen, Svalbard.
Deschamps-Berger, Nuth, van Pelt, Berthier, Kohler & Altena, Journal of glaciology.

[published] Extracting recent short-term glacier velocity evolution over southern Alaska and the Yukon from a large collection of Landsat data.
Altena, Scambos, Kääb & Fahnestock, The cryosphere.

[published] Observing change in glacier flow by using optical satellites
Altena, Doctoral thesis university of Oslo.

Popular publications

Copernicus Sentinels observe vast and fast movements in the Arctic
Sentinel online

Speurtocht met satellietbeelden.
Geografie. (magazine for Dutch geography teachers)

Guest appearance in Berillium newsletter.

Har fått ESA-stipend for å bruke satellittdata til å forstå Jordens frosne overflate
Titan (university news outlet)

Should we send Hans Brinker to the Greenland ice sheet?
Tvergastein : interdisciplinary journal of the environment

Presentions

Automatic extraction of velocity time-series at mountain range scale from Landsat 8. Altena, Scambos, Fahnestock & Kääb at EGU.
Daily cubesat imagery to observe and assess processes in the cryosphere. Altena & Kääb at EGU.
Poster presentation on; "Sensing a moving Arctic from space" during the Arctic day in Oslo.
Presented during GeoHyd Lunch Seminar at University of Oslo about the ICEFLOW project.
Gave a talk at NVE (HB-lunsj) entitled *Kinematics in the Cryosphere from space*
Seminar talk at TUDelft; From satellite snapshots towards snow and ice services.
Co-convening session at *AGU fall meeting*: Glacier processes from large scale remote sensing
High-resolution surface and upper fjord circulation of greenland fjords from optical remote sensing. Altena & Kääb, at AGU.
Cold-regions river flow using a cubesat constellation. Kääb, Altena & Mascaro, at AGU.
Hot spots and large basal rivers? Effects on Greenland ice sheet simulations of proposed geographic features hidden at the base of the ice.. Chambers, Greve, Altena & Lefeuvre, at AGU.
An invited talk at GI-Forum, Münster (Germany).
Convening session at *ESA Living Planet*: Opportunities brought by constellations of small satellites to help understand process on the Earth's surface or to explore new services
Poster presentation at LPS entitled: River ice velocity from Sentinel-twogether and PROBA-VELOCITY.
Poster presentation at LPS entitled: Cold-regions river flow using a cubesat constellation.
Gave a talk at LPS entitled: Bringing together remote sensing data to produce region-wide glacier velocities.
Gave a talk at the Peace Research Institute Oslo entitled: Sensors in space for society.
Gave a conference presentation during the ISPRS Geopsatial week, Enschede.
I have given a keynote presentation during the ISPRS summer school on close range remote sensing, Innsbruck.
Gave an invited presentation during the IUGG general assembly, Montreal.
Presented my new postdoc work during the Earth Observation, Science & Society Symposium, The Hague.
Gave a presentation and got feedback during the mid-term review in Frascati.
Presented my work at Very High ResOlution satellite Data Assessment (VH-RODA), Frascati.
Presented "Sensing surface shifts with high-repeat Sentinel-2 imagery" in Φ-Lab.
Co-convening session at *EGU general assembly*: Remote sensing of the cryosphere
Presented work on icecliff backwasting during the EGU general assembly, see also the associated website.

Research visits

Two months research visit at *Institute of Low Temperature Studies*, Hokkaido University, Japan. Done within the CryoJano-program.

Through the RemoteEx-programa it was possible to conduct a one month research visit to the *Laboratory for Cryospheric Research*, University of Ottawa, Canada.

A one month visit to ESA ESRIN was made possible by the Living Planet Fellowship.

Journal of Glaciology

Paper

Cite this article: Haga ON, McNabb R, Nuth C, Altena B, Schellenberger T, Kääb A (2020). From high friction zone to frontal collapse: dynamics of an ongoing tidewater glacier surge, Negribreen, Svalbard. *Journal of Glaciology* 1–13. https://doi.org/10.1017/jog.2020.43

Received: 3 February 2020
Revised: 16 May 2020
Accepted: 18 May 2020

Keywords:
Glacier surges; ice velocity; remote sensing

Author for correspondence:
Odin Næss Haga,
E-mail: haga.odin.n@gmail.com

cambridge.org/jog

From high friction zone to frontal collapse: dynamics of an ongoing tidewater glacier surge, Negribreen, Svalbard

Odin Næss Haga[1], Robert McNabb[1,2], Christopher Nuth[1,3], Bas Altena[1,4], Thomas Schellenberger[1] and Andreas Kääb[1]

[1]Department of Geosciences, University of Oslo, Oslo, Norway; [2]School of Geography and Environmental Sciences, Ulster University, Coleraine, United Kingdom; [3]The Norwegian Defense Research Establishment, Kjeller, Norway and [4]Institute for Marine and Atmospheric Research, Utrecht University, Utrecht, The Netherlands

Abstract

Negribreen, a tidewater glacier located in central eastern Svalbard, began actively surging after it experienced an initial collapse in summer 2016. The surge resulted in horizontal surface velocities of more than 25 m d^{-1}, making it one of the fastest-flowing glaciers in the archipelago. The last surge of Negribreen likely occurred in the 1930s, but due to a long quiescent phase, investigations of this glacier have been limited. As Negribreen is part of the Negribreen Glacier System, one of the largest glacier systems in Svalbard, investigating its current surge event provides important information on surge behaviour among tidewater glaciers within the region. Here, we demonstrate the surge development and discuss triggering mechanisms using time series of digital elevation models (1969–2018), surface velocities (1995–2018), crevasse patterns and glacier extents from various data sources. We find that the active surge results from a four-stage process. Stage 1 (quiescent phase) involves a long-term, gradual geometry change due to high subglacial friction towards the terminus. These changes allow the onset of Stage 2, an accelerating frontal destabilization, which ultimately results in the collapse (Stage 3) and active surge (Stage 4).

Introduction

Glacier surges are cyclic phenomena whereby glaciers switch between periodic phases of low activity with slow ice flow during a century- to decadal-long 'quiescent' phase, and rapid flow during a short-lived peak ('surge' phase) where velocities increase by a factor of 10–1000 times (Meier and Post, 1969; Murray and others, 2003a). While only ~1% of the glaciers in the world are thought to be of surge-type (Jiskoot and others, 1998; Sevestre and Benn, 2015), the Svalbard archipelago contains one of the densest population of such glaciers in the world with estimates varying between 13% (Jiskoot and others, 1998) and 54–90% (Lefauconnier and Hagen, 1991). Small glaciers and ice caps are expected to be large contributors to sea-level rise in the near-future (Zemp and others, 2019), and from Svalbard, tidewater glaciers are the largest contributors (Nuth and others, 2010). Hence, a better understanding of surge-type tidewater glaciers in Svalbard that have the ability to quickly discharge large ice masses into the ocean will provide more accurate sea-level projection from this region.

Similar to most Arctic tidewater glaciers, Svalbard glaciers also lose most of their mass through frontal ablation (calving + submarine melt) (e.g. Rignot and others, 2008; Błaszczyk and others, 2009; Burgess and others, 2013; Van Wychen and others, 2014; Khan and others, 2015; McNabb and others, 2015). In Svalbard, historical synthesis of remote-sensing studies has shown that marine-terminating surge-type glaciers commonly have different surge behaviour than land-terminating surge-type glaciers (Murray and others, 2003b), although this does not exclude that both types can be explained by the same theoretical principles (Sevestre and Benn, 2015). Earlier studies on tidewater glaciers in Svalbard and in particular on Osbornebreen, Fridtjovbreen and Monacobreen (Hodgkins and Dowdeswell, 1994; Rolstad and others, 1997; Luckman and others, 2002; Murray and others, 2003b) have suggested that the surge initiates over the lower part of the glacier and then spreads over the entire glacier surface based upon the evolution of surface velocities and crevasses patterns. Down-glacier surge initiation and up-glacier spread of surface velocities was also observed on Sortebrae, a tidewater glacier in East Greenland, albeit with various propagation nuclei (Pritchard and others, 2005). By contrast, on land-terminating glaciers in Svalbard such as Usherbreen and Bakaninbreen (Hagen, 1987; Murray and others, 1998), the active surge starts from the upper accumulation area following a surge front travelling down glacier, which is similar to observations from Variegated Glacier and Trapridge Glacier in Alaska and Yukon (Clarke and others, 1984; Kamb and others, 1985; Frappé and Clarke, 2007).

Despite the potentially large number of surge-type tidewater glaciers in Svalbard (Błaszczyk and others, 2009), the typically long periods between the active phases have historically given few opportunities to study repeating surge events in detail (Mansell and others, 2012). However, more recent surge events and the improved availability of remotely sensed data have yielded higher spatial and temporal observations in the time leading up to an active surge on such glaciers. Evidence from these events shows that the active surge phase initiates

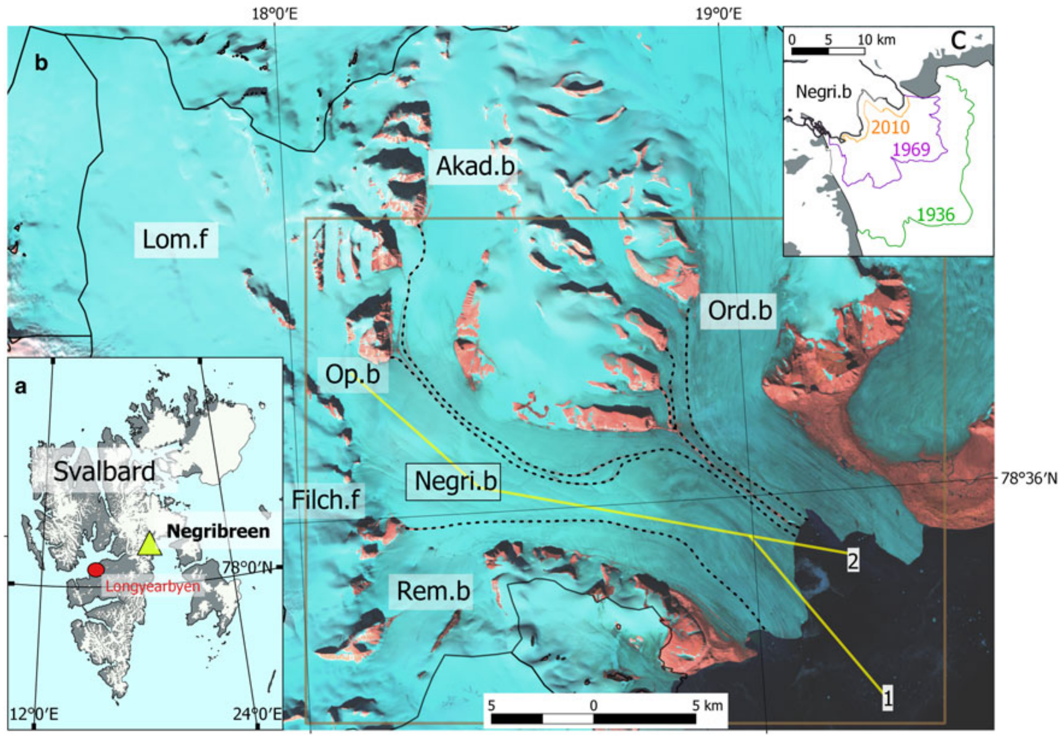

Fig. 1. (a) Map of Svalbard. (b) Overview of the Negribreen Glacier System: location of Negribreen (Negri.b) and neighbouring glaciers Ordonnansbreen (Ord.b), Akademikarbreen (Akad.b) and Rembebreen (Rem.b) are indicated as well as reservoir area Filchnerfonna (Filch.f) and main reservoir Lomonosovfonna (Lom.f), connected to Negribreen through Opalbreen (Op.b). Background image is a summer 2015 Landsat-8 scene and black dashed lines designate glacier boundaries. The brown box represents the approximate extent of maps in other figures. The yellow lines show location of the two centreline profiles used to extract velocity and elevation (line no. 1 for Stage 1 and no. 2 for Stage 2–4). (c) Outline of the glacier in 2015 in black with general retreat patterns since the last surge in 1936 in colour.

after a frontal destabilization (Strozzi and others, 2017; Sevestre and others, 2018; Willis and others, 2018; Nuth and others, 2019). During the destabilization, crevassing often initiates or intensifies close to the terminus and propagates up-glacier (Flink and others, 2015; Sevestre and others, 2018). Crevasses have been shown to be able to cause a cycle of positive feedbacks in glacier dynamics by increasing surface melt-water input to the glacier bed, a feedback that was documented in detail during the surge on Basin-3 of Austfonna (Dunse and others, 2015), and has been observed on other glaciers (e.g. Gilbert and others, 2020). Because the accelerating destabilization prior to the active surge probably only lasts for a few seasons on Svalbard tidewater glaciers, high temporal resolution analysis is necessary to understand both how the destabilization begins and further evolves.

In 2016, an active surge occurred on Negribreen, a tidewater glacier located on the eastern coast of Svalbard (Fig. 1). The surge activated after a frontal collapse, with a signature similar to the collapse of the Nathorst Glacier System (NGS) (Nuth and others, 2019) or Stonebreen (Strozzi and others, 2017). With remotely sensed data, this paper documents the Negribreen surge event by investigating the dynamic evolution of the glacier via surface velocities, elevation changes, surface structural changes and external conditions, including sea-ice and ocean surface temperatures. We map out a timeline of the dynamic evolution by dividing the surge cycle into four stages, from which we discuss how Negribreen evolved towards an active surge.

Study area

According to radio echosounding investigations from Dowdeswell and others (1984), Negribreen is polythermal with a layered cold to temperate thermal ice column. The glacier has two reservoir areas: Filchnerfonna and a section of Lomonosovfonna (main reservoir), which are both connected to the glacier through Filchnerfallet and Opalbreen, respectively (Fig. 1). The Negribreen terminus drains into Storfjorden in Olav V and Sabine Land along with the neighbouring glaciers Ordonnansbreen, Akademikarbreen and Rembebreen. These glaciers, along with some smaller unnamed tributaries, make up the Negribreen Glacier System. In total, this covers an area of 1180 km^2, making it one of the largest glacier systems on the island of Spitsbergen.

The last time Negribreen surged is thought to be between 1935 and 1936 (Liestøl, 1969; Lefauconnier and Hagen, 1991). Photos and observations from that time show a significant advance and visible crevasses in the accumulation areas of Negribreen, Akademikarbreen and Ordonnansbreen, suggesting that most of the glacier systems contributed to the terminus advance at that time (Lefauconnier and Hagen, 1991). Liestøl (1969) estimated that the front advanced with an average speed of 35 $m\,d^{-1}$. Recent sea-floor mapping shows mostly fine-grained sediments beyond this surge and suggests that the 1936 terminal moraine position is most likely the largest extent of Negribreen during the Holocene (Ottesen and others, 2017). After the last surge, aerial images show little signs of surface deformation and the terminus has been in continuous retreat (Lefauconnier and Hagen, 1991). Outside of Negribreen's 2010 extent, eskers are present on the sea-floor which prolong out in the fjord up to the 1969 extent, indicating that there has been an efficient subglacial drainage system for at least the last decades (Ottesen and others, 2017) while the front position has been retreating (Nuth and others, 2013).

Data and methods

Glacier surface velocities

To get a sufficient temporal coverage of surface velocities, we used data from several sources (Table 1). The earliest observations come from the European Remote Sensing (ERS) satellites ERS-1 and ERS-2 using their tandem-mode observations in 1995 and 1997, which we have processed using standard single-azimuth differential interferometry using the GAMMA radar software (i.e. co-registration, formation of interferogram, flattening, removal of topographic phase, unwrapping; e.g. Luckman and others, 2002). In contrast to tracking, simple radar interferometry provides only one velocity component in the satellite looking direction (line of sight). We also used standard offset tracking on a RADARSAT-1 radar image pair of 11 March–4 April 2008 (e.g. Schellenberger and others, 2015).

A timeline with higher temporal resolution was created for 2014–18. Within the day-lit months (approximately March through October), surface velocity data mostly come from the Global Land and ice Velocity Extraction (GoLIVE) dataset (Fahnestock and others, 2016; Scambos and others, 2016). The GoLIVE velocity fields are created by normalized cross-correlation (NCC) on a sampling grid of 300 m, based on the Landsat-8 panchromatic bands. All fields covering Negribreen with a path between 209 and 219 and row 003 or 004 (WRS-2 path/row grid system) were downloaded and re-projected to WGS84/UTM33N. We used the highest temporal resolution available with a 16 d repeat cycle and the recommended correlation threshold of 0.3 (Sam and others, 2018). To supplement this dense velocity record and fill potential gaps during polar day, we used additional Sentinel-2 optical data to achieve even higher temporal resolution. For specific implementation details, see (Altena and others, 2019).

To obtain surface velocities during polar night or whenever light conditions were insufficient, we used Sentinel-1 C-band synthetic aperture radar (SAR) data. A total of 15 image pairs were downloaded from Sentinel Open Access Hub and velocity fields were generated using the Sentinel Application Platform (ESA, 2019). Before offset tracking, we applied orbital files and co-registered image pairs with the Altimeter Corrected Elevations Global Digital Elevation Model (ACE GDEM; Berry and others, 2000). The GRD-format amplitude images were also calibrated so that the pixel values represent radar backscatter values. Velocities were estimated using NCC image matching on subset views covering only Negribreen. The window dimension used was 300 m in both azimuth and range spacing. This makes the search box large enough so that texture, not noise, is matched, but also not too large, which would degrade the matching accuracy under the presence of spatial velocity gradients.

To estimate the uncertainty in the velocity measurements, we selected multiple regions over assumed stable terrain and averaged the displacement values for each image pair. We found that all Sentinel-1 image pairs had stable ground velocities below $0.5\ \mathrm{m\,d^{-1}}$. In general, the stable terrain velocities from Sentinel-2 and Landsat-8 also gave values below $0.5\ \mathrm{m\,d^{-1}}$, but were in some cases higher in the range of $0.5–1\ \mathrm{m\,d^{-1}}$. During some periods, we found these sources of error to be significant. For instance, for the pre-surge image pair covering 18 September–4 October 2015, the average displacement over stable ground exceeded some of the measured on-glacier velocities. However, the fact that we have multiple measurements showing the same underlying trend lends confidence to the velocity measurements.

Table 1. Overview of the data acquisitions used for surface velocity extraction and their stable terrain velocities. Data from several sensors were needed to get sufficient information to produce a timeline of events. Data sources include the European Remote Sensing satellites (ERS), RADARSAT-1 (R1), Landsat-8 (L8), Sentinel-1 (S1) and Sentinel-2 (S2)

Year	Sensor	First scene	Second scene	Stable terrain vel. (mean/standard dev.)
Pre 2010	ERS	08-11-1995	09-11-1995	0.003/0.0004
	ERS	09-10-1997	10-10-1997	0.010/0.003
	R1	11-03-2008	04-04-2008	–
2014	L8	04-08-2014	20-08-2014	0.117/0.131
2015	L8	18-09-2015	04-10-2015	0.633/0.549
	S1	30-11-2015	24-12-2015	0.157/0.029
	S1	24-12-2015	01-17-2016	0.110/0.027
2016	L8	19-03-2016	04-04-2016	1.066/0.667
	L8	04-04-2016	20-04-2016	0.562/0.377
	L8	13-04-2016	29-04-2016	0.418/0.255
	S2	23-07-2016	02-08-2016	0.591/0.321
	S2	05-08-2016	15-08-2016	0.471/0.152
	S2	02-09-2016	12-09-2016	0.874/0.510
	S1	19-10-2016	31-10-2016	0.225/0.061
2017	S1	23-01-2017	29-01-2017	0.119/0.025
	L8	05-03-2017	21-03-2017	0.530/0.627
	L8	21-03-2017	06-04-2017	0.420/0.237
	L8	31-03-2017	16-04-2017	0.227/0.308
	L8	06-04-2017	22-04-2017	0.180/0.144
	L8	22-04-2017	08-05-2017	0.388/0.211
	L8	27-05-2017	12-06-2017	0.884/0.561
	L8	21-06-2017	07-07-2017	0.638/0.280
	L8	07-07-2017	23-07-2017	0.552/0.487
	L8	23-07-2017	08-08-2017	0.333/0.258
	L8	08-08-2017	24-08-2017	0.930/0.293
	S1	14-10-2017	26-10-2017	0.340/0.111
	S1	07-11-2017	19-11-2017	0.587/0.168
	S1	01-12-2017	13-12-2017	0.357/0.109
2018	L8	11-03-2018	27-03-2018	0.438/0.504
	L8	03-04-2018	19-04-2018	0.283/0.281
	S2	27-04-2018	07-05-2018	0.310/0.504
	S2	03-07-2018	13-07-2018	0.911/0.437
	S2	30-07-2018	14-08-2018	0.479/0.228
	S1	02-11-2018	14-11-2018	0.179/0.043
	S1	08-12-2018	20-12-2018	0.147/0.028
2019	S2	30-04-2019	10-05-2019	0.125/0.111
	S2	11-08-2019	21-08-2019	0.100/0.123

Digital elevation models

To study elevation and elevation changes on Negribreen, we use digital elevation models (DEMs) derived from multiple sources (Table 2). The earliest DEM we have available is photogrammetrically derived from aerial photos acquired in 1969 over the lowermost zone of the glacier, processed by the Norwegian Polar Institute (NPI). Additionally, we used a DEM produced by NPI from aerial photos acquired in 1990, which covered most of the Negribreen system.

Most of the later DEMs we have used are from optical stereo satellite imagery such as the Advanced Spaceborne Thermal Emission and Reflection Radiometer (ASTER) (e.g. Toutin, 2008) and ArcticDEM strips (Porter and others, 2018). ASTER DEMs are processed using MicMac ASTER (MMASTER Girod and others, 2017) with jitter correction performed by comparisons to the ArcticDEM v3.0 mosaic.

Finally, we used the TanDEM-X Intermediate DEM (IDEM; Balzter and others, 2016) product over Negribreen, resampled from 12 to 30 m resolution. This DEM is a mosaicked product of six separate acquisitions between 15 December 2010 and 26 March 2012. Five of these acquisitions are from December 2010 and January 2011, with the final acquisition from March 2012. The X-band radar signal penetrates dry snow to an unknown depth of up to a few metres, resulting in a negative bias as the

Table 2. DEMs used for elevation changes. To increase the spatial coverage of the ArcticDEM strips, we mosaicked strips acquired within a short time of each other; uncertainties reported for both the mosaicked product, as well as the individual strips in parentheses

Source	Scene date(s) dd-mm-yyyy	Vertical uncertainty (m)
Norwegian Polar Institute	1969	5.1
	1990	5
ASTER	07-07-2004	10.3
	14-08-2018	8.2
TanDEM-X	15-12-2010–26-3-2012 (treated as late summer 2010)	4.6
ArticDEM	2013: 14-07-2013, 18-07-2013, 27-07-2013	2.9 (1.7, 1.6, 2.9)
	2014: 22-04-2014, 24-04-2014	1.8 (2.3, 1.7)
	2015: 12-07-2015, 30-07-2015	3.1 (1.5, 3.6)
	2016: 22-07-2016, 03-08-2016	2.4 (2, 2.4)
	2017: 31-07-2017, 02-08-2017	1.9 (1.9, 1.9)

elevation values represent a surface that is below the actual snow surface (e.g. Dehecq and others, 2016). Because most of the acquisitions come from winter 2010/2011, we assume that the elevation reflects the surface conditions of late summer 2010.

To achieve minimum biases in the elevation differences, we co-registered all DEMs using the same methodology as Nuth and Kääb (2011). Before applying this method, we re-sampled all data to 40 m resolution and re-projected them to the same coordinate system (WGS84/UTM33N). The co-registration process was done using the ArcticDEM mosaic as a reference, as it has consistent high-quality coverage over the study area. Due to the narrow spatial coverage of the ArcticDEM strip files, we created mosaics of 2–3 co-registered strips that were acquired relatively close in time (Table 2) using bilinear resampling.

The final root mean square error (RMSE) comparison over stable terrain shows that the ArcticDEM strip files have the highest accuracy, with errors ~2.5 m. Uncertainties for the NPI DEMs and the IDEM are ~5 m while the ASTER scenes have the lowest accuracy, with RMSE values of 10.3 and 8.2 m for the 7 July 2004 and 14 August 2018 acquisitions, respectively.

We used the following equation to estimate the uncertainty in elevation change calculated by differencing two individual DEM products:

$$\varepsilon_{ab} = \frac{\sqrt{\varepsilon_a^2 + \varepsilon_b^2}}{t} \tag{1}$$

where ε_a and ε_b are the vertical uncertainties in the older and newer DEM, respectively, and t is the time difference in years between the product acquisition dates.

We find that the error propagation of the vertical uncertainties is in fact significant for DEM differences when the rate of elevation change is small and the time interval between products is short. For example, during the 1990–04 and 2004–10 periods, vertical uncertainties of 1.09 and 2.48 m a^{-1}, respectively, exceed the measured elevation change rates over the entire glacier. Even for the ArcticDEM strip files, which have higher accuracy, uncertainties are still significant in the upper portions of the glacier between 2010 and 2016, as elevation change rates are still low. After 2016, the elevation change is significant, exceeding the vertical uncertainties. We do acknowledge the limitation of these uncertainties. However, similar to the velocity-related errors, we have more confidence in the data through the confirmation of several calculations which show a underlying trend, at least in a qualitative way. We argue that these differences are sufficient for this study.

Driving stress

As there are only sparse measurements of bed topography and ice thickness available for Negribreen, we used a simple calculation to get an indication of driving stress τ_b:

$$\tau_b = \rho g h \tan \alpha \tag{2}$$

where ρ is ice density (assumed to be 917 kg m^{-3}), g is the gravitational acceleration (9.8 m s^{-2}), h is the ice thickness and α is the surface slope.

To estimate ice thickness, we subtracted the radio echo sounding profile of bed elevation collected in 1980 by Dowdeswell and others (1984) from DEM surface elevations. We restricted this calculation to follow this profile, which is approximately along the glacier centreline. We calculated average driving stresses for two intervals of 2 km length each along this profile, one at the front portion of the glacier and another further up-glacier. We averaged estimated ice thickness from three sample points along each interval and averaged surface elevation and slope from DEMs to approximate driving stress.

Glacier length changes and crevasses

We manually digitized ice front positions from aerial photographs and satellite imagery acquired between 1969 and 2017. Additionally, we digitized approximate front positions pre-1969 based on mapped positions presented by Lefauconnier and Hagen (1991). To estimate length changes, we used the so-called 'box method' (e.g. Moon and Joughin, 2008; Howat and others, 2010), as this method yields a less arbitrary measure of length than estimates along a single centreline location.

We also manually outlined crevasse expanse using Landsat and ASTER imagery from 2004 to 2019. Further information about crevasses in the 1990s was obtained by visually interpreting radar backscatter in ERS images.

Sea surface conditions

Fjord or ocean conditions can have a significant impact on calving behaviour, either through amplifying calving from increased ocean temperature (Luckman and others, 2015) or by ice mélange buttressing the glacier (Todd and Christoffersen, 2014). In our investigation, we examined two ocean surface variables such as sea-ice concentration and sea surface temperature close to the terminus of Negribreen. We used monthly averaged reanalysis products between 1990 and 2018 provided by the Arctic Marine Forecasting Center, available at http://marine.copernicus.eu/.

The sea surface temperature assimilated dataset combines observations from infrared sensors, microwave sensors and in situ data from ships and surface drifting buoys, provided by the European Space Agency Sea Surface Temperature Climate Change Initiative (ESA SST CCI). It has a spatial resolution of ~6 km. The sea-ice fraction dataset is obtained from Special Sensor Microwave/Imager (SSM/I) at The Ocean and Sea Ice Satellite Application facility (OSI SAF). This has a sampling grid of 12.5 km, which is used to be consistent with other operational OSI SAF products. However, this sampling grid does not represent the true spatial resolution of the product. The dataset already had a correction for coastal effects, since the radiometric signature of land is similar to sea ice at the wavelengths used for estimating sea-ice concentration. The pixels used to extract data from both products were more than 10 km from land, and we expect only a coarse interpretation of sea surface conditions outside Negribreen. More information about these datasets can be found in Sakov and others (2015).

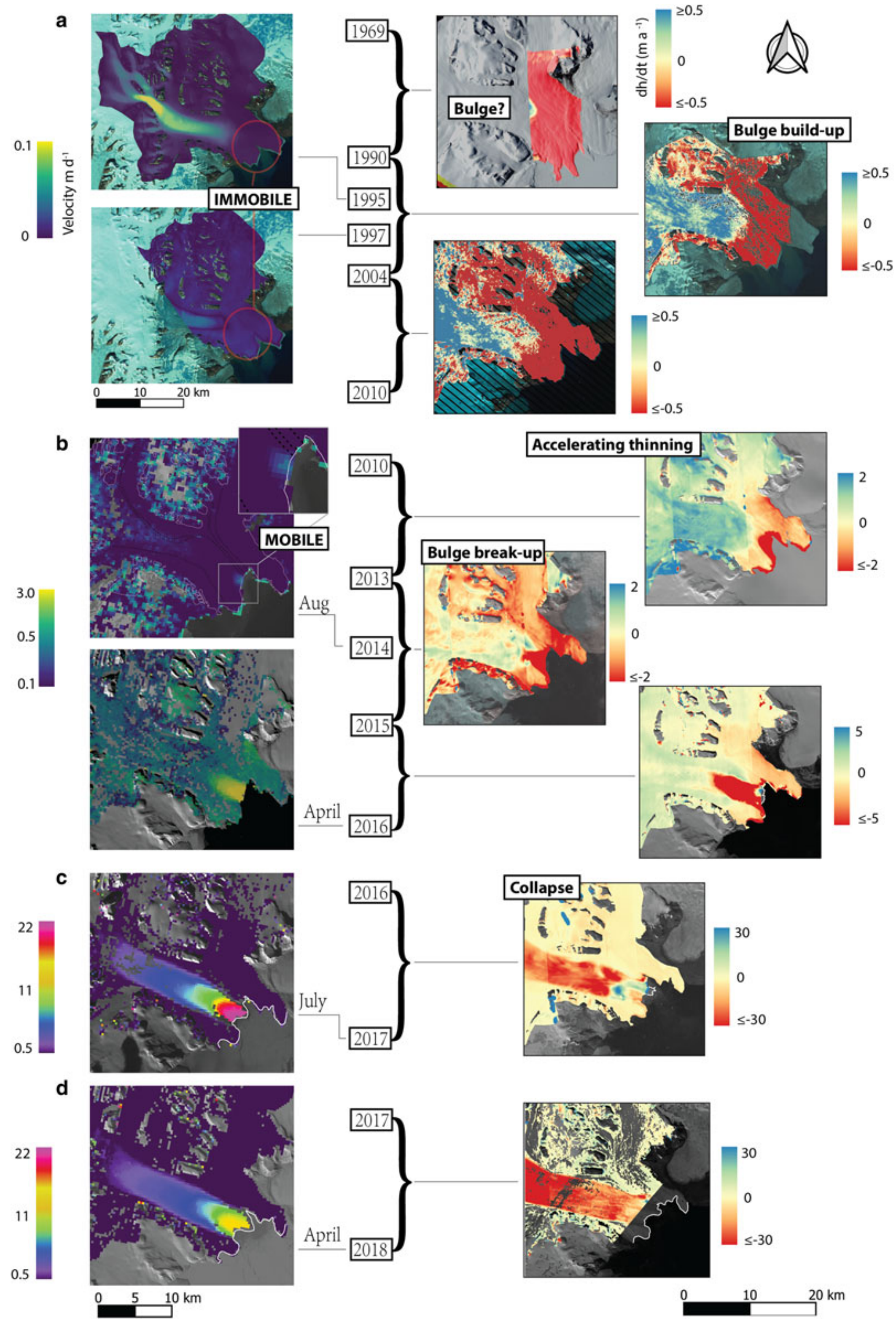

Fig. 2. A timeline of the surge on Negribreen, divided into stages of dynamic behaviour. Left column shows surface velocities given in metres per day (not corrected for stable ground velocities), and right column shows elevation differences given in metres per year. (a) Stage 1, bulge build-up and frontal thinning. (b) Stage 2, dynamic initiation towards the glacier front. (c) Stage 3, collapse and onset of active surge. (d) Stage 4, velocity deceleration.

Observations and interpretation

In this section, we present the dynamic evolution of Negribreen since 1969. Through interpretation, mainly of surface velocities and elevation changes, we have divided our observations into four stages based on changes in glacier behaviour. A total overview of the stages can be seen in Figure 2. The stages are in relation to the frontal collapse that occurred on Negribreen in early 2016, which is where we interpret the active surge phase to start.

Stage 1, Pre-collapse: long-term surface geometry change

Elevation change mapping shows that Negribreen underwent a persistent long-term change in surface geometry, which includes thinning towards the terminus and a gradual thickening further up-glacier (Figs 2a and 3b). Between 1969 and 1990, thinning affected the lower portion of the glacier and continued throughout 1990–04 and 2004–10. The thinning rates measured in all sub-periods have approximately similar values. Between 1969 and

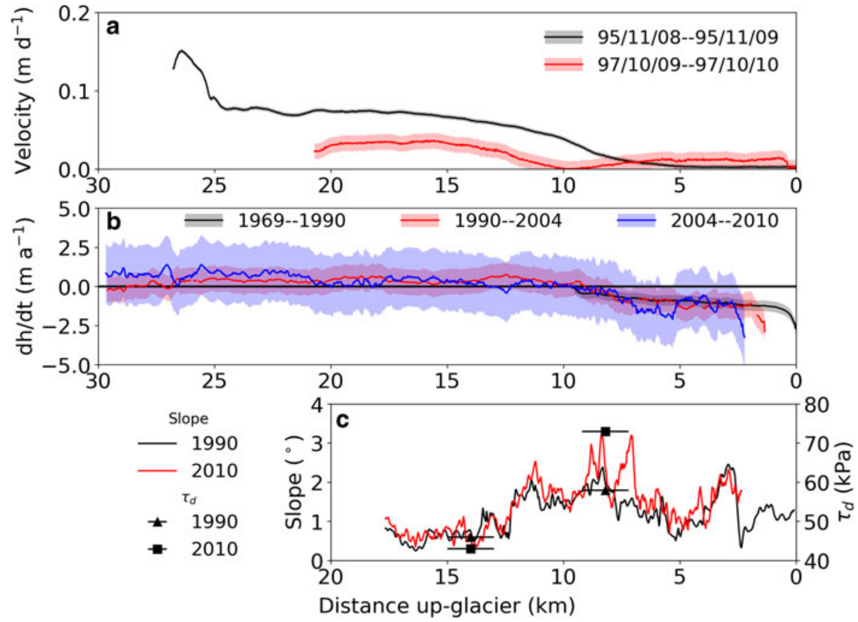

Fig. 3. Centreline data on Negribreen during Stage 1. Shaded colour are respective data uncertainties. (a) Velocities in metres per day from ERS interferometry during a 1 d interval in 1995 and 1997. Note that the ERS velocities have different look-directions. (b) Elevation changes in metres per year between elevation products, 1969–2010. The black horizontal bars show no change. (c) Surface slope and averaged local driving stress values in 1990 and 2010.

1990, the thinning rates were ~3 ± 0.5 m a^{-1} closest to the terminus, gradually decreasing to 0 m a^{-1} ~9 km from the terminus. Between 1990 and 2004, the surface at the front thinned at 1 ± 1 m a^{-1}, approaching zero 8 km from the terminus, and in 2004–10 areas close to the terminus thinned by ~3 ± 2.5 m a^{-1}, reaching equilibrium ~9 km from the terminus.

Up-glacier from the thinning area, the surface showed a gradual increase in elevation since at least the 1990–04 and 2004–10 periods, with ranges between $0 - 0.5$ and $0 - 1 \pm 2.5$ m a^{-1}, respectively. The limited DEM coverage from the 1969 dataset makes it difficult to investigate this area pre-1990, but we still see elevation changes approaching 0 m a^{-1} in the same location as in the 1990–04 and 2004–10 differences. This could indicate that surface elevation was increasing pre-1990, although the limited DEM coverage makes any conclusions difficult.

Over time, the elevation changes resulted in a modification of the glacier's geometry, with long-term thinning and steepening of the front since at least 1969, and a small bulge development. From Figure 2a, the extent of the bulge seems to have little spatial fluctuation, and the steepening is most profound in the areas closest to the bulge front, ~7–9 km from the terminus (Fig. 3c). The surface slope in this area increases from values ranging between 1.5 and 2.5° in 1990 and up to 3.5° in 2010. The average driving stress at this area shows a 1.25-fold increase from 58 kPa in 1990 to 73 kPa in 2010 (Fig. 3c). At 13–15 km from the terminus, ~3–5 km up-glacier from the bulge front, we see little change in slope and driving stresses are more or less constant with 46 kPa in 1990 and 43 kPa in 2010.

Interferometric surface velocity from the ERS satellites in 1995 and 1997 provides further important observations of Stage 1 (Figs 2a and 3a). In both acquisitions, velocities are especially low, likely because the acquisitions are from early winter. These velocities are in the satellite's look direction, which conveniently is along the flow direction in the accumulation area for the 1995 pair, and along flow in the ablation area for the 1997 pair. Both of these velocity snapshots together show the existence of mobile ice in the accumulation area, and mostly immobile ice towards the glacier front. Additional velocity measurements from offset tracking in 2008 RADARSAT data show no real difference to the 1995/1997 measurements, with very low velocities (< 0.05 m d^{-1}) at the glacier front, increasing to ~0.12 m d^{-1} in the ablation area. All of this suggests the presence of high basal friction near the glacier front, a likely factor in the bulge development as the zone of higher friction may have been acting as a barrier for the mobile ice coming from the accumulation area, thus forcing the surface to 'pile up'.

In the 1995 velocity field, which has a greater coverage of the glacier, highest velocities are seen on Opalbreen, ~25 km from the terminus of Negribreen. This narrow valley glacier acts as a funnel between Negribreen and Lomonosovfonna, the main reservoir area. Here, we also see a consistent presence of crevasses throughout Stage 1 (e.g. ASTER scene from 2004, Fig. 4a), another indication of mobile ice. The mobile nature of the upper basin of Lomonosovfonna suggests that this area has been acting as a source of ice contributing to the bulge development. In the southern part of this reservoir where elevation data are available between 1990 and 2014, we detect a distinct area of surface thinning (Fig. 5b). It covers a surface of 27 km^2 with a mean thinning rate of 1.4 m a^{-1} and a cumulative elevation loss of 33.6 m. This area could be representative of such a source of ice, and similar thinning might have occurred elsewhere on the upper basin of Lomonosovfonna. However, this specific area touches the drainage divide of the upper basin of Tunabreen, another known surge-type tidewater glacier (Flink and others, 2015). Therefore, it is unclear if the outflow from this specific area contributed completely to the bulge of Negribreen, flowing east, or partly to Tunabreen, flowing south.

Between 1969 and 2010, Negribreen retreated nearly 8 km (Fig. 6). There is very little observational evidence for seasonal variation in terminus position during this time period, which is consistent with the immobile ice at the front evidenced by the ERS velocities. The retreat was not consistent across the entire terminus, but was rather stronger in small embayments that appear to be related to subglacial drainage features, as evidenced by the eskers highlighted in Figure 6a. Additional ERS images from the 1990s show small regions of increased radar backscatter near the terminus, an indication that crevassing was mostly limited to the glacier terminus. Between 2000 and 2010, we also see an extended period of reduced sea-ice concentration relative to the 18-year timeline of available data (Fig. 6b).

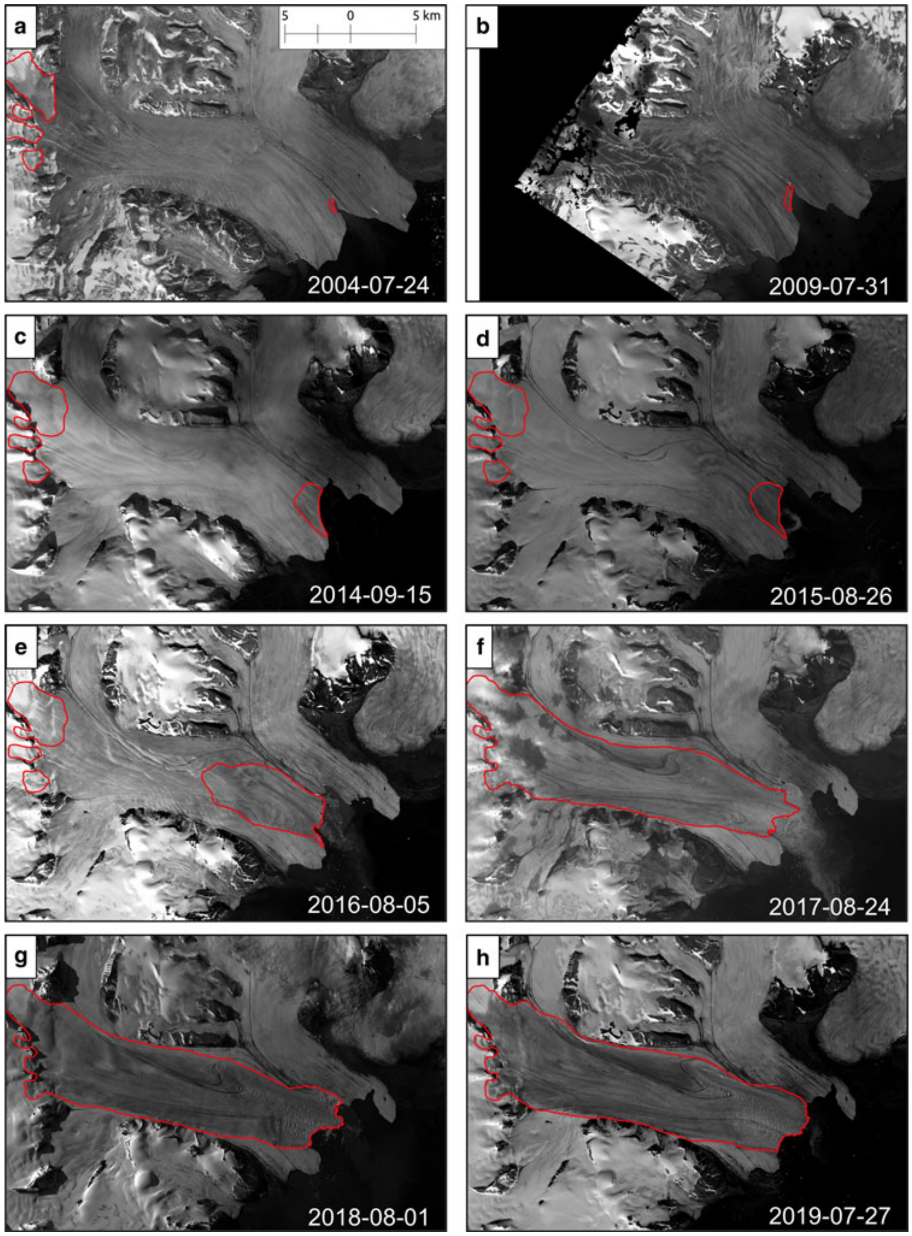

Fig. 4. Extent of visibly crevassed areas (red outline) as digitized from ASTER (a, b) and Landsat 8 (d–h) imagery acquired on the dates shown.

Stage 2, Pre-collapse: surface dynamic initiation/accelerating geometry change

Distinct signs imply that Negribreen underwent a dynamic transition beginning around 2010 (Figs 2b and 7). After decades of the rather gradual changes described in Stage 1, Stage 2 reflects a trend of accelerating dynamics at the glacier front, causing a process of destabilization. In this stage, surface lowering accelerated in all sub-periods analysed (Fig. 7b). From 2010 to 2013, the surface elevation decreased by 7 m a^{-1} and already showed a substantial change from the previous periods. We do not have any surface velocity observations in this window, but we would expect them to still be low, owing to the low velocities observed in both 2008 and 2014 (Fig. 7a). At this time, the bulge was still unaffected and continued to increase in elevation at 2 m a^{-1}, a behaviour similar to the previous stage.

Between 2013 and 2015, the surface lowering increased to a maximum of 12 m a^{-1} near the front, and signs of the bulge breaking up began to appear. Within this time, a minor increase in surface velocities is seen from 0.25 to 0.5±0.6 m d^{-1} between August 2014 and June 2015 near the front. By 2015–16, the yearly thinning rate reached a maximum of 25 m a^{-1}, and a significant bulge break-up had occurred, since the surface areas affected by thinning expanded 5 km further up-glacier from the terminus. It is here where we observed a shift towards greater acceleration in velocities, and the speed at the glacier front increased from 0.5 to 2±0.6 m d^{-1} over the melt-season of 2015.

We observed little frontal deceleration towards December 2015, as velocities were still at 1.5 ± 0.11 m d^{-1}. A distinct velocity slowdown in winter would be a common behaviour for a non-surge-type tidewater glacier (e.g. Schellenberger and others, 2015), as in winter there is less surface melt-water and rainfall lubricating the glacier bed. The insignificant decrease in winter velocity on Negribreen could suggest that a fundamental change in glacier dynamics was ongoing. In spring 2016, velocities increased to an even higher rate, with measurable changes

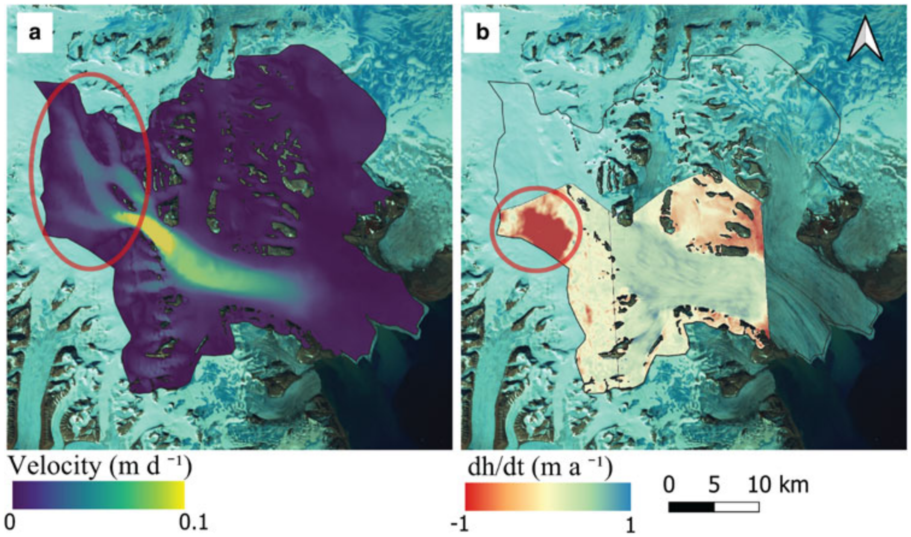

Fig. 5. (a) Surface velocities from ERS interferomtery in metres per day from 1995. (b) Elevation differencing between 1990 and 2014 in m a^{-1}. Together the figures highlight an area of mobile ice on the Lomonosovfonna reservoir area.

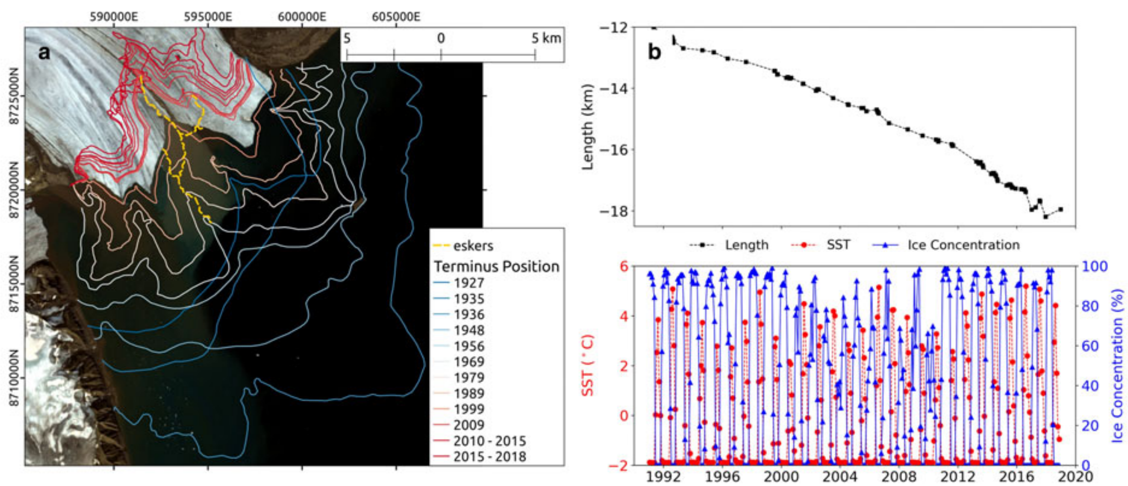

Fig. 6. (a) Terminus positions from Lefauconnier and Hagen (1991), optical and radar imagery, as well as location of eskers identified by Ottesen and others (2017). Notice the amplifying retreat pattern where the eskers are. (b) Time series of glacier length (relative to 1936 terminus position), sea surface temperature and sea-ice concentration.

occurring from week to week, e.g. from 2.6 to 3.2±0.42 m d^{-1} over two successive weeks in April. Our observations show a strong correlation between surface elevation decrease and increasing velocities.

Optical imagery reveals that crevasses began to rapidly evolve from the terminus region after summer 2015 (Fig. 4d). By 2016, crevasses had spread up-glacier with a distinct crevasse field covering the first 5 km upstream of the glacier front. The shape of the crevasses is perpendicular to flow, indicative of extension. It is also obvious that the area of accelerating surface thinning or velocities coincided with the area where crevasses were present. Measurements of the terminus position show a seasonal pattern developing after 2013, indicating that Negribreen underwent a change from mostly immobile ice to more classical tidewater glacier behaviour (Fig. 6b).

Stage 3, Collapse: activation of high surface velocities

In late summer 2016, the frontal portion of the glacier collapsed. High surface velocities were no longer restricted to the frontal zone, with velocities in excess of 3 m d^{-1} observed 10 km upstream of the glacier terminus (Fig. 8a). This rapid velocity acceleration, affecting the entire glacier, lasted the rest of 2016 until the beginning of 2017. In the spring of 2017, this acceleration ceased and velocities remained at a constant high at ~14–16 m d^{-1} near the terminus, with velocities > 3 m d^{-1} observed 15 km from the terminus. At this time, extensional crevasses covered the entire surface of Negribreen (Fig. 4f). Within the year since the collapse, the glacier surface lowered by over 30 m in some areas (Fig. 2). A final short-term peak in velocities occurred in the following melt-season in 2017, reaching the maximum recorded velocity of 25±0.8 m d^{-1}.

Stage 4, Post-collapse: deceleration

After the velocity peak detected in the melt-season of 2017, the glacier entered a period of deceleration. At the end of 2017, peak velocities decreased to ~15 m d^{-1}, by the end of 2018 down to ~10 m d^{-1}, and in late summer 2019 down to 5 m d^{-1} (Fig. 8b). As seen in Figure 7c, this slowdown happened rather

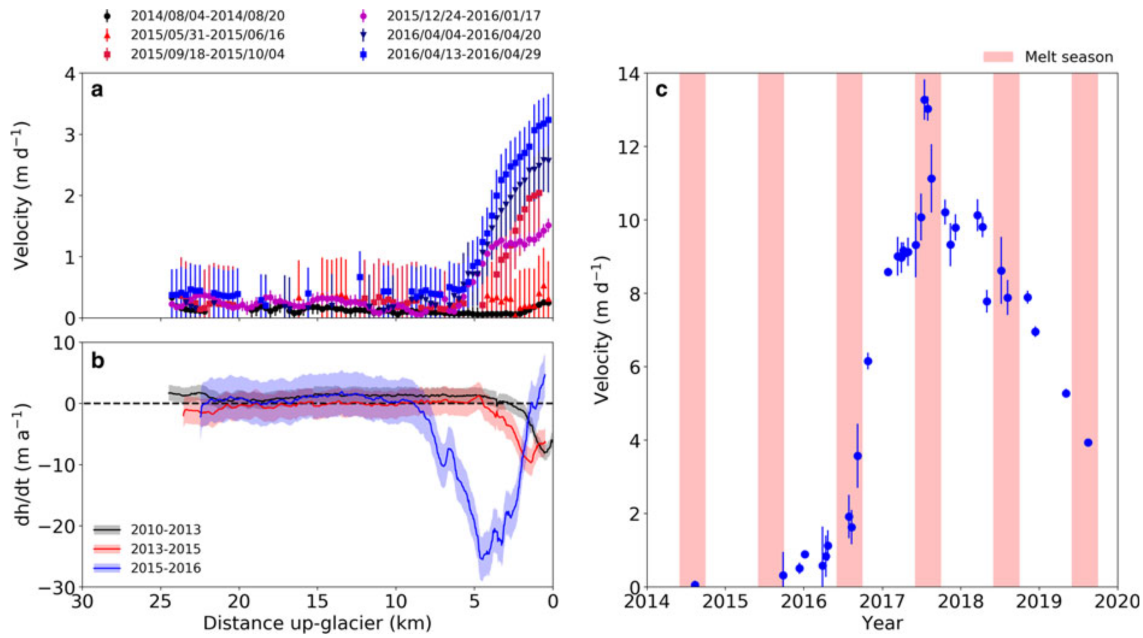

Fig. 7. Evolution of glacier dynamics along centre line during Stage 2. (a) Surface velocities (m d^{-1}). Velocities are calculated every 300 m (points). Error bars are stable ground velocities. (b) Change in surface elevation between elevation products (m a^{-1}). Shaded area shows vertical uncertainties. (c) Average velocities from all pixels between 3 and 5 km (from the coast) of Negribreen.

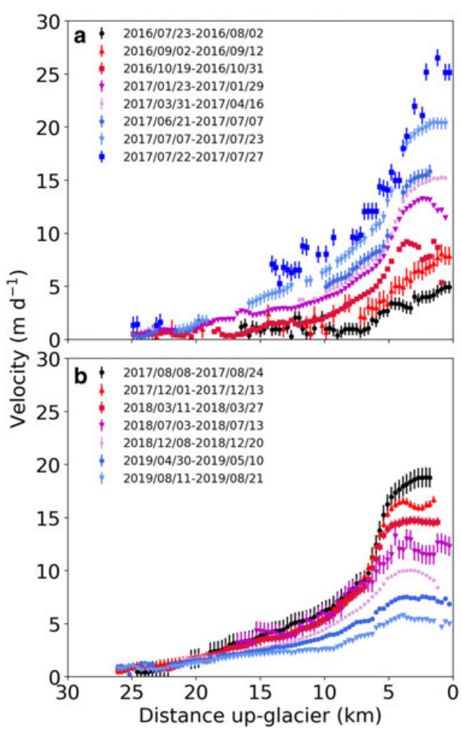

Fig. 8. Centreline surface velocities (metres per day) over Negribreen. (a) Rapidly accelerating velocities during Stage 3, from after the collapse of summer 2016 until melt-season in 2017. (b) Gradual deceleration of velocities during Stage 4 after the melt-season in 2017.

gradually. Since velocities are still high early post-collapse and stretching the ice, the glacier surface elevation continued to lower in this stage (Fig. 2). Figures 4g, h show similar crevasse extents in 2018 and 2019 as to 2017, but crevassing had become noticeably more intensified, even spreading to Rembebreen and Akademikarbreen.

Discussion

We have interpreted the recent surge event at Negribreen in four stages. All stages show distinct behaviour, and each stage provided the conditions necessary for the next. In this section, we compare our observations to other observed surges in Svalbard. We discuss in detail the basal friction, geometry change and spread of crevasses, all important processes occurring in Stages 1 and 2 which led towards the final onset of this surge event. To help compare observations of recent surges in Svalbard, Table 3 summarizes our observations for Negribreen as well as a number of recent studies of other glaciers.

High basal friction and bulge formation

A critical factor related to the surge at Negribreen is the distribution of friction beneath the glacier. At polythermal glaciers such as Negribreen, basal friction is itself related to both the glacier's thermal regime and the amount of liquid water at the bed of the glacier (i.e. the enthalpy of the glacier; Aschwanden and others, 2012; Sevestre and Benn, 2015; Benn and others, 2019), as well as the properties of the bed itself. Persistent, long-term high friction at Negribreen is suggested by the presence of immobile ice near the terminus and the subsequent 'bulge' formation (Fig. 2), as well as the presence of eskers in the fjord in front of Negribreen indicating a long-established efficient drainage system. Similar observations of areas with high basal friction and stagnant ice near the terminus have been noted for other surge-type tidewater glaciers in the region, such as for the NGS (Nuth and others, 2019), Basin-3 of Austfonna (Dunse and others, 2015), Stonebreen (Strozzi and others, 2017) and Perseibreen (Dowdeswell and Benham, 2003).

On Svalbard, influence of the thermal regime on surge-type glaciers varies according to size and whether they terminate on land or in water, with tidewater glaciers having predominantly temperate conditions at their beds (Sevestre and others, 2015). The observation of a cold-temperate transition surface along the centreline of Negribreen by Dowdeswell and others (1984)

Table 3. Summary of observations across a selection of tidewater glacier surges in Svalbard. In each column, 'yes' indicates that a particular observation was confirmed in the literature, 'no' indicates it was confirmed to be absent, and '–' indicates it was not reported. For observations of eskers, the survey year(s) are given. Additionally, 'SV' = 'Surface Velocity', 'Crev. init.' = 'Crevasse Initiation'

Glacier name/time of surge	Eskers on seafloor	Frontal thinning	Bulge detected	SV accel. phase	Frontal steepening	Crev. init. at front	Immobile pre-surge
Negribreen 2016–	yes 2007–2009[r]	yes	yes	3 yr (min)	yes	yes	yes
Osbornebreen 1986–1990[a,b]	–	–	no	–	–	yes	–
Monacobreen 1992–1996[c,d,e,f]	–	–	no	1 yr (min)	–	yes	–
Fridtjovbreen 1995–1997[g,h]	–	yes	no	3 yr (min)	yes	yes	–
Perseibreen 2000–2002[i]	–	–	no	–	–	yes	yes
Tunabreen 2003–05[j,k]	no 2011[k]	–	no	–	–	yes	–
Blomstrandbreen 2007[e]	no 2010[t]	–	–	–	–	–	–
Wahlenbergbreen ca. 2009[l]	–	yes	no	yes	yes	yes	–
NGS Jan 2009[m,n]	yes 2006[s]	yes	yes	–	yes	yes	yes
Basin-3 2012[o]	–	yes	–	4 yr	–	–	yes
Stonebreen 2013[p]	–	yes	–	3 yr (min)	yes	–	yes
Aavatsmarkbreen 2013–2015[l]	–	yes	no	yes	yes	yes	–
Moršnevbreen 2016[q]	–	yes	yes	–	–	–	–

[a] Dowdeswell and others (1991); [b] Rolstad and others (1997); [c] Luckman and others (2002); [d] Strozzi and others (2002); [e] Mansell and others (2012); [f] Murray and others (2003b); [g] Murray and others (2003a); [h] Murray and others (2012); [i] Dowdeswell and Benham (2003); [j] Fleming and others (2013); [k] Flink and others (2015); [l] Sevestre and others (2018); [m] Sund and others (2014); [n] Nuth and others (2019); [o] Dunse and others (2015); [p] Strozzi and others (2017); [q] Benn and others (2019); [r] Ottesen and others (2017); [s] Ottesen and others (2008); [t] Burton and others (2016).

suggests that the zone of high friction was not due to the thermal regime alone; that is, it is unlikely that the entire terminus region was frozen to the bed. Nuth and others (2019) showed, with a thermo-mechanical model, that it is sufficient to have localized cold patches at the bed. These cold patches would then act to reduce mean basal sliding, which eventually stabilizes an efficient drainage system through large channels in the sediments, promoting higher friction. This interpretation, which we hypothesize was also the case at Negribreen during Stage 1, is further supported by the observed submarine eskers in the fjord.

Eskers are also found in association with non-surging glaciers and are thus not thought to be diagnostic of surge activity (Dowdeswell and Ottesen, 2016). As all proposed theories of surge behaviour require an inefficient subglacial hydrological system during the active phase of a surge cycle, the eskers are likely to have formed after a surge termination or during quiescence (Ottesen and others, 2008). Also, any pre-surge eskers are likely to be erased with the passage of the surge front. This may explain why such depositions are not seen in front of the surge glaciers Blomstrandbreen and Tunabreen, as sea-floor surveys were conducted too soon after their respective surges (Flink and others, 2015; Burton and others, 2016).

Over time, the zones of high friction near the front served as an impediment to ice as it flowed from the accumulation area, causing a 'bulge' to form. The long duration of the thickening signal (pre-1990 to 2010), as well as its relatively low magnitude ($<2\,\mathrm{m\,a^{-1}}$), suggests that the bulge formed as a result of ice steadily flowing down from the accumulation area and building up as it encountered the high friction zone. This is contrasting with ice being 'pushed' through the glacier system from a destabilizing reservoir area, which has been observed during land-terminating surges in Svalbard like the 1985–1995 surge event on Bakaninbreen (Murray and others, 1998). Besides Negribreen and Bakaninbreen, the only other Svalbard surge events with a well-documented bulge formation are the recent events from NGS (Sund and others, 2014; Nuth and others, 2019) and Moršnevbreen (Benn and others, 2019). In other remote-sensing analyses of Svalbard glacier surges, including on Osbornebreen (Rolstad and others, 1997), Perseibreen (Dowdeswell and Benham, 2003), Tunabreen (Flink and others, 2015), Monacobreen (Luckman and others, 2002; Murray and others, 2003b) and Fridtjovbreen (Murray and others, 2003a, 2012), examination of crevasse patterns or DEM differencing shows the absence of a surge bulge travelling down-glacier, which does not necessarily preclude a bulge presence like the one observed on Negribreen.

Furthermore, the extent of the bulge gives information about the footprint of areas with enhanced subglacial friction. In the case of Negribreen, this footprint was stable since at least 1990 as the bulge front did not change its extent before it broke up during Stage 2. This contrasts to one of the bulges from the NGS surge and the bulge on Moršnevbreen, which were reported to migrate down-glacier, indicating a dynamic sub-glacial footprint.

Bulge weakening and collapse

During Stage 2, the bulge weakened, leading to the activation of the surge and the onset of collapse. DEM differencing between 2010 and 2013 (Fig. 2b) shows strong thinning in the terminus region, in the same areas where we observed crevasses in 2004 and 2009 (Fig. 4), and where velocities first began to increase in 2014 and 2015. It is also where we first observe seasonal fluctuations in the glacier length, beginning in 2013. These different lines of evidence strongly suggest that the zones of high friction were shrinking/disappearing.

Between 1990 and 2010, the growth of the bulge led to an increase in surface slope, with the largest increase occurring near the bulge front. Surface steepening at the glacier front is a common observation before a tidewater surge in Svalbard, and it is known to cause increased driving stresses, as observed prior to the respective surges of Aavatsmarkbreen, Nathorstbreen and Stonebreen (Strozzi and others, 2017; Sevestre and others, 2018; Nuth and others, 2019). This increase in surface slope led to an increase in driving stress from 58 to 73 kPa, a 1.25-fold increase. Because the basal melt rate is proportional to τ_d^4 (e.g. van der Veen, 2013), this increase would lead to a 2.4-fold increase in basal melt rate. Between 2010 and 2015, the driving stress increased slightly from 73 to 79 kPa, which would lead to a further 1.6-fold increase in basal melt rate. This increase in melt rate could have led to a reduction in basal friction near the terminus, encouraging an increase in velocity. While the increase in basal melt rate was likely not the sole cause of the destabilization, the decrease in basal friction and subsequent increase in surface velocities observed could have started a feedback cycle that eventually led to the collapse.

Ocean forcing has been shown to be able to influence rates of frontal ablation (submarine melt + calving; e.g. Motyka and others, 2003; Bartholomaus and others, 2013) at several tidewater glaciers in Svalbard (Luckman and others, 2015). In that study, Luckman and others (2015) argued that the observed strong correlation between frontal ablation rate and ocean temperature indicated melt-driven convection at the ice-ocean interface, which is highly sensitive to ambient ocean temperatures (Jenkins, 2011). During Stage 1, Negribreen was retreating into deeper water (Ottesen and others, 2017), exposing more of the glacier terminus to submarine melt throughout the year, which could have aided in its destabilization. However, Negribreen outlets on the eastern coast of Svalbard, where ocean temperatures are typically lower than on the west coast (Jakowczyk and Stramska, 2014), suggesting that the influence of the ocean may not be as strong as at other glaciers. We also do not see any strong correlation between ocean surface temperatures and either length change or surface velocity, further suggesting a smaller influence of the ocean in this case.

Another external influence could come from sea-ice conditions, which have been shown to influence calving rates, glacier dynamics and terminus stability in other regions like Greenland (e.g. Joughin and others, 2008; Amundson and others, 2010) and Novaya Zemlya (Carr and others, 2014). However, despite a reduction of sea ice from 2000 to 2010, the true significance of this might be negligible in Stage 1, as ice near the terminus is mostly immobile, and no clear signals are seen in length changes. Potentially, there could be higher sea-ice influence in Stage 2, when the glacier front becomes mobile, but to what degree is difficult to speculate based on the available data.

Dating to the 1990s, we observe small zones of crevasses near the terminus of Negribreen. During Stage 1, there are few signs of expansion of these zones, which tend to occur near or overtop areas of assumed efficient subglacial channels, observed as submarine eskers. As none of our observations suggest increased dynamics during Stage 1, it seems likely that these crevasses were not deep enough to influence the bed of the glacier via input of surface meltwater. However, this seems to have been the case in Stage 2. The up-glacier expansion of the crevassed regions correlates well with both the strong thinning and increase in surface velocity. This points towards a positive feedback cycle where increasing velocities feed the appearance of crevasses, leading to more surface water lubricating the bed, further allowing velocities to increase. This feedback cycle was observed on both Basin-3 of Austfonna (Dunse and others, 2015) and Stonebreen (Strozzi and others, 2017) during their pre-surge acceleration. On Basin-3, high temporal resolution Global Positioning System (GPS) measurements showed that the at least 4-year long multi-annual acceleration was not gradual, but occurred in steps, each following a summer speedup. A similar trend can be seen in Figure 7c, where Negribreen between at least two successive summers had detectable step increases in velocity, though the detail of documentation during this period is not as high as on Basin-3. Surface melt-water input to the bed would provide an increase in enthalpy, as it is both an efficient heat source and a source of liquid water. The warming caused by this meltwater input would help to remove any remaining cold patches at the bed causing high friction, and together with frictional heating from deformation, would further enhance sliding and promote increased crevassing at the glacier surface.

Conclusion

We have investigated the ongoing surge of Negribreen, a tidewater glacier on the east coast of Svalbard. From remotely sensed data with high temporal resolution, we have shown that this surge of a tidewater glacier is composed of four distinct stages. The initiation of the active surge itself occurred after a long-term geometric change and frontal destabilization in Stages 1 and 2, respectively. We find that the 'onset' of the surge is a chain of connected processes, which began in Stage 1 with the establishment of high friction beneath the lower portion of the glacier. Our interpretation is that the zone of enhanced friction was a combination of cold patches of ice as well as an established efficient subglacial drainage system, indicated by eskers imprinted on the seafloor in front of the glacier. Consequently, the high-friction barrier divided the glacier flow regime into an immobile zone at the front and a mobile zone further up-glacier. This caused a gradual modification of the glacier geometry with the development of a bulge at the high-friction boundary, increasing of surface slope at the bulge head, and thinning of the glacier front.

The frontal thinning is a very important process in the feedback proposed here. First, it lowered a potential driving-stress threshold by increasing the surface slope, which eventually decreased the subglacial friction and promoted a rapid frontal destabilization through increasing basal lubrication by surface melt-water through enhanced crevassing. This in turn caused accelerating thinning rates due to rapidly accelerating surface velocities. A pattern of up-glacier propagating crevassing, initiated at the terminus, shows similar dynamic evolution as has been documented on other surging tidewater glaciers in Svalbard. Our study demonstrates how a combination of the wealth of remotely-sensed data currently available enables us to decipher surge evolutions in an unprecedented way, and to newly interpret past events with less comprehensive data coverage.

Acknowledgments. This research has been supported by the European Research Council (project: FP/2007-2013/ERC; grant no. 320816) and the European Space Agency Glaciers-CCI, CCI+, ICEFLOW, and EE10 HARMONY projects (4000109873/14/I-NB, 4000127593/19/I/NB, 4000125560/18/I-NS, 4000127656/19/NL/FF/gp). Additional support was provided by the Norwegian Space Centre project Copernicus Glacier Service for Norway (NIT.06.15.5). The study is a contribution to the Svalbard Integrated Arctic Earth Observing System SIOS. Radarsat data were provided by NSC/KSAT under the Norwegian-Canadian Radarsat agreements 2007–2019. ERS-1/2 data were provided by ESA through PRODEX. TanDEM-X DEM was provided through DLR grant IDEM GLAC0435. We are very grateful to USGS for Landsat data, and the Norwegian Polar Institute for the historical map data/DEMs. Acquisition of ASTER images was guided by NASA JPL through the ASTER science team and the Global Land Ice Measurements from Space (GLIMS) initiative. ArcticDEM DEMs provided by the Polar Geospatial Center under NSF-OPP awards 1043681, 1559691 and 1542736. We thank the GoLIVE project for providing free velocity data for the public. We also thank Scientific Editor Hester Jiskoot and two anonymous reviewers for their constructive comments which helped improve the clarity of the manuscript.

References

Altena B, Haga ON, Nuth C and Kääb A (2019) Monitoring sub-weekly evolution of surface velocity and elevation for a high-latitude surging glacier using Sentinel-2. *International Archives of Photogrammetry, Remote Sensing and Spatial Information Sciences* **XLII-2/W13**, 1723–1727. doi:10.5194/isprs-archives-XLII-2-W13-1723-2019

Amundson JM and 5 others (2010) Ice mélange dynamics and implications for terminus stability, Jakobshavn Isbræ, Greenland. *Journal of Geophysical Research* **115**(F01005). doi:10.1029/2009JF001405

Aschwanden A, Bueler E, Khroulev C and Blatter H (2012) An enthalpy formulation for glaciers and ice sheets. *Journal of Glaciology* **58**(209), 441–457. doi:10.3189/2012JoG11J088

Balzter H, Baade J and Rogers K (2016) Validation of the TanDEM-X intermediate digital elevation model with airborne LiDAR and differential GNSS in Kruger National Park. *IEEE Geoscience and Remote Sensing Letters* **13**(2), 277–281. doi:10.1109/LGRS.2015.2509500

Bartholomaus TC, Larsen CF and O'Neel S (2013) Does calving matter? Evidence for significant submarine melt. *Earth and Planetary Science Letters* **380**, 21–30. doi:10.1016/Journalepsl.2013.08.014

Benn DI and 6 others (2019) Mass and enthalpy budget evolution during the surge of a polythermal glacier: a test of theory. *Journal of Glaciology* **65**, 1–15. doi:10.1017/jog.2019.63

Benn DI, Fowler AC, Hewitt I and Sevestre H (2019) A general theory of glacier surges. *Journal of Glaciology* **65**(253), 701–716. doi:10.1017/jog.2019.62

Berry PAM, Pinnock RA, Hilton RD and Johnson CPD (2000) ACE: A new GDEM incorporating satellite altimeter derived heights. ESA Pub. SP-461.

Błaszczyk M, Jania JA and Hagen JO (2009) Tidewater glaciers of Svalbard: recent changes and estimates of calving fluxes. *Polish Polar Research* **30**(2), 85–142.

Burgess EW, Forster RR and Larsen CF (2013) Flow velocities of Alaskan glaciers. *Nature Communications* **4**, 2146. doi:10.1038/ncomms3146

Burton DJ, Dowdeswell JA, Hogan KA and Noormets R (2016) Marginal fluctuations of a Svalbard surge-type tidewater glacier, Blomstrandbreen, since the Little Ice Age: a record of three surges. *Arctic, Antarctic and Alpine Research* **48**(2), 411–426. doi:10.1657/AAAR0014-094

Carr JR, Stokes CR and Vieli A (2014) Recent retreat of major outlet glaciers on Novaya Zemlya, Russian Arctic, influenced by fjord geometry and sea-ice conditions. *Journal of Glaciology* **60**(219), 155–170. doi:10.3189/2014JoG13J122

Clarke GKC, Collins SG and Thompson DE (1984) Flow, thermal structure, and subglacial conditions of a surge-type glacier. *Canadian Journal of Earth Sciences* **21**(2), 232–240. doi:10.1139/e84-024

Dehecq A and 5 others (2016) Elevation changes inferred from TanDEM-X data over the Mont-Blanc area: impact of the X-band interferometric bias. *IEEE Journal of Select Topics in Applied Earth Observations and Remote Sensing* **9**(8), 3870–3882. doi:10.1109/JSTARS.2016.2581482

Dowdeswell JA and Benham TJ (2003) A surge of Perseibreen, Svalbard, examined using aerial photography and ASTER high resolution satellite imagery. *Polar Research* **22**(2), 373–383. doi:10.1111/Journal1751-8369.2003.tb00118.x

Dowdeswell JA, Drewry DJ, Liestøl O and Orheim O (1984) *Airborne radio echo sounding of sub-polar glaciers in Spitsbergen*. Norsk Polarinstitutt.

Dowdeswell JA, Hamilton GS and Hagen JO (1991) The duration of the active phase on surge-type glaciers: contrasts between Svalbard and other regions. *Journal of Glaciology* **37**(127), 388–400. doi:10.3189/S0022143000005827

Dowdeswell JA and Ottesen D (2016) Eskers formed at the beds of modern surge-type tidewater glaciers in Spitsbergen. *Geological Society Memoirs* **46**(1), 83–84. doi:10.1144/M46.70

Dunse T and 5 others (2015) Glacier-surge mechanisms promoted by a hydro-thermodynamic feedback to summer melt. *The Cryosphere* **9**(1), 197–215. doi:10.5194/tc-9-197-2015

ESA (2019) SNAP – ESA Sentinel Application Platform v7.0.3. http://step.esa.int/.

Fahnestock M and 5 others (2016) Rapid large-area mapping of ice flow using landsat 8. *Remote Sensing of Environment* **185**, 84–94. doi:10.1016/Journalrse.2015.11.023

Fleming EJ and 6 others (2013) Magnetic fabrics in the basal ice of a surge-type glacier. *Journal of Geophysical Research: Earth Surface* **118**(4), 2263–2278. doi:10.1002/jgrf.20144

Flink AE and 5 others (2015) The evolution of a submarine landform record following recent and multiple surges of Tunabreen glacier, Svalbard. *Quaternary Science Reviews* **108**, 37–50. doi:10.1016/Journalquascirev.2014.11.006

Frappé TP and Clarke GKC (2007) Slow surge of Trapridge Glacier, Yukon Territory, Canada. *Journal of Geophysical Research: Earth Surface* **112**(F03S32). doi:10.1029/2006JF000607

Gilbert A and 6 others (2020) The influence of water percolation through crevasses on the thermal regime of a Himalayan mountain glacier. *The Cryosphere* **14**(4), 1273–1288. doi:10.5194/tc-14-1273-2020

Girod L, Nuth C, Kääb A, McNabb RW and Galland O (2017) MMASTER: improved ASTER DEMs for elevation change monitoring. *Remote Sensing* **7**, 704–729. doi:10.3390/rs9070704

Hagen JO (1987) Glacier surge at Usherbreen, Svalbard. *Polar Research* **5**(2), 239–252. doi:10.3402/polar.v5i2.6879

Hodgkins R and Dowdeswell JA (1994) Tectonic processes in Svalbard tidewater glacier surges: evidence from structural glaciology. *Journal of Glaciology* **40**(136), 553–560. doi:10.3189/S0022143000012430

Howat IM, Box JE, Ahn Y, Herrington A and McFadden EM (2010) Seasonal variability in the dynamics of marine-terminating outlet glaciers in Greenland. *Journal of Glaciology* **56**(198), 601–613. doi:10.3189/002214310793146232

Jakowczyk M and Stramska M (2014) Spatial and temporal variability of satellite-derived sea surface temperature in the Barents Sea. *International Journal of Remote Sensing* **35**(17), 6545–6560. doi:10.1080/01431161.2014.958247

Jenkins A (2011) Convection-driven melting near the grounding lines of ice shelves and tidewater glaciers. *Journal of Physical Oceanography* **41**(12), 2279–2294. doi:10.1175/JPO-D-11-03.1

Jiskoot H, Boyle P and Murray T (1998) The incidence of glacier surging in Svalbard: evidence from multivariate statistics. *Computers & Geosciences* **24**(4), 387–399. doi:10.1016/S0098-3004(98)00033-8

Joughin I and 7 others (2008) Continued evolution of Jakobshavn Isbrae following its rapid speedup. *Journal of Geophysical Research: Earth Surface* **113**(F04006). doi:10.1029/2008JF001023

Kamb B and 7 others (1985) Glacier surge mechanism: 1982-1983 surge of Variegated Glacier, Alaska. *Science (New York, N.Y.)* **227**(4686), 469–479. doi:10.1126/science.227.4686.469

Khan SA and 5 others (2015) Greenland ice sheet mass balance: a review. *Reports on Progress in Physics* **78**(4), 046801. doi:10.1088/0034-4885/78/4/046801

Lefauconnier B and Hagen JO (1991) *Surging and calving glaciers in eastern Svalbard*. Oslo: Norsk Polarinstitutt.

Liestøl O (1969) Glacier surges in west Spitsbergen. *Canadian Journal of Earth Sciences* **6**(4), 895–897. doi:10.1139/e69-092

Luckman A and 5 others (2015) Calving rates at tidewater glaciers vary strongly with ocean temperature. *Nature Communications* **6**, 8566. doi:10.1038/ncomms9566

Luckman A, Murray T and Strozzi T (2002) Surface flow evolution throughout a glacier surge measured by satellite radar interferometry. *Geophysical Research Letters* **29**(23), 10-1-10-4. doi:10.1029/2001GL014570

Mansell D, Luckman A and Murray T (2012) Dynamics of tidewater surge-type glaciers in northwest Svalbard. *Journal of Glaciology* **58**(207), 110–118. doi:10.3189/2012JoG11J058

McNabb RW, Hock R and Huss M (2015) Variations in Alaska tidewater glacier frontal ablation, 1985-2013. *Journal of Geophysical Research: Earth Surface* **120**(1), 120–136. doi:10.1002/2014JF003276

Meier MF and Post A (1969) What are glacier surges? *Canadian Journal of Earth Sciences* **6**(4), 807–817. doi:10.1139/e69-081

Moon TK and Joughin I (2008) Retreat and advance of Greenland tidewater glaciers from 1992 to 2007. *Journal of Geophysical Research* **113**(345), F02022. doi:10.1029/2007JF000927

Motyka RJ, Hunter L, Echelmeyer KA and Connor C (2003) Submarine melting at the terminus of a temperate tidewater glacier, LeConte Glacier, Alaska, USA. *Annals of Glaciology* **36**, 57–65.

Murray T and 5 others (2012) Geometric changes in a tidewater glacier in Svalbard during its surge cycle. *Arctic, Antarctic and Alpine Research* **44**(3), 359–367. doi:10.1657/1938-4246-44.3.359

Murray T, Dowdeswell JA, Drewry DJ and Frearson I (1998) Geometric evolution and ice dynamics during a surge of Bakaninbreen, Svalbard. *Journal of Glaciology* **44**(147), 263–272. doi:10.3189/S0022143000002604

Murray T, Luckman A, Strozzi T and Nuttall AM (2003a) The initiation of glacier surging at Fridtjovbreen, Svalbard. *Annals of Glaciology* **36**, 110–116. doi:10.3189/172756403781816275

Murray T, Strozzi T, Luckman A, Jiskoot H and Christakos P (2003b) Is there a single surge mechanism? Contrasts in dynamics between glacier surges in Svalbard and other regions. *Journal of Geophysical Research: Solid Earth* **108**(B5), 2237–2252. doi:10.1029/2002JB001906.

Nuth C and 7 others (2013) Decadal changes from a multi-temporal glacier inventory of Svalbard. *The Cryosphere* **7**(5), 1603–1621. doi:10.5194/tc-7-1603-2013

Nuth C and 9 others (2019) Dynamic vulnerability revealed in the collapse of an Arctic tidewater glacier. *Scientific Reports* **9**(5541). doi:10.1038/s41598-019-41117-0

Nuth C and Kääb A (2011) Co-registration and bias corrections of satellite elevation data sets for quantifying glacier thickness change. *The Cryosphere* **5**(1), 271–290. doi:10.5194/tc-5-271-2011

Nuth C, Moholdt G, Kohler J, Hagen JO and Kääb A (2010) Svalbard glacier elevation changes and contribution to sea level rise. *Journal of Geophysical Research: Earth Surface* **115**(F01008). doi:10.1029/2008JF001223

Ottesen D and 9 others (2008) Submarine landforms characteristic of glacier surges in two Spitsbergen fjords. *Quaternary Science Reviews* **27**(15–16), 1583–1599. doi:10.1016/Journalquascirev.2008.05.007

Ottesen D, Dowdeswell JA, Bellec VK and Bjarnadóttir LR (2017) The geomorphic imprint of glacier surges into open-marine waters: examples from eastern Svalbard. *Marine Geology* **392**, 1–29. doi:10.1016/Journalmargeo.2017.08.007

Porter C and 28 others (2018) ArcticDEM doi:10.7910/DVN/OHHUKH.

Pritchard H, Murray T, Luckman A, Strozzi T and Barr S (2005) Glacier surge dynamics of Sortebræ, East Greenland, from synthetic aperture radar feature tracking. *Journal of Geophysical Research: Earth Surface* **110** (F03005).

Rignot E and 6 others (2008) Recent Antarctic ice mass loss from radar interferometry and regional climate modelling. *Nature Geoscience* **1**(2), 106. doi:10.1038/ngeo102

Rolstad C, Amlien J, Hagen JO and Lundén B (1997) Visible and near-infrared digital images for determination of ice velocities and surface elevation during a surge on Osbornebreen, a tidewater glacier in Svalbard. *Annals of Glaciology* **24**, 255–261. doi:10.3189/S026030550001226X

Sakov P, Counillon F, Bertino L, Finck N and Renkl C (2015) Quality Information Document For Arctic Physical Reanalysis Product–EU Copernicus Marine Service. Technical report, Tech. rep., Bergen.

Sam L, Bhardwaj A, Kumar R, Buchroithner MF and Martín-Torres FJ (2018) Heterogeneity in topographic control on velocities of Western Himalayan glaciers. *Scientific Reports* **8**(1), 12843. doi:10.1038/s41598-018-31310-y

Scambos T, Fahnestock M, Moon T, Gardner A and Klinger M (2016) Global Land Ice Velocity Extraction from Landsat 8 (GoLIVE), Version 1. [subsets: p209_r004, p210_r004, p211_r004, p212_r004, p213_r003, p213_r004, p214_r003, p214_r004, p215_r003, p216_r003, p217_r003, p218_r003, p219_r003]. Boulder, Colorado USA. NSIDC: National Snow and Ice Data Center, doi:10.7265/N5ZP442B [Accessed December 2018].

Schellenberger T, Dunse T, Kääb A, Kohler J and Reijmer CH (2015) Surface speed and frontal ablation of Kronebreen and Kongsbreen, NW Svalbard, from SAR offset tracking. *The Cryosphere* **9**(6), 2339–2355. doi:10.5194/tc-9-2339-2015

Sevestre H and 6 others (2018) Tidewater glacier surges initiated at the terminus. *Journal of Geophysical Research: Earth Surface* **123**(5), 1035–1051. doi:10.1029/2017JF004358

Sevestre H and Benn DI (2015) Climatic and geometric controls on the global distribution of surge-type glaciers: implications for a unifying model of surging. *Journal of Glaciology* **61**(228), 646–662. doi:10.3189/2015JoG14J136

Sevestre H, Benn DI, Hulton NRJ and Bælum K (2015) Thermal structure of Svalbard glaciers and implications for thermal switch models of glacier surging. *Journal of Geophysical Research: Earth Surface* **120**(10), 2220–2236. doi:10.1002/2015JF003517

Strozzi T, Kääb A and Schellenberger T (2017) Frontal destabilization of Stonebreen, Edgeøya, Svalbard. *The Cryosphere* **11**, 553–566. doi:10.5194/tc-11-553-2017

Strozzi T, Luckman AJ, Murray T, Wegmüller U and Werner CL (2002) Glacier motion estimation using SAR offset-tracking procedures. *IEEE Transactions on Geoscience and Remote Sensing* **40**(11), 2384–2391. doi:10.1109/TGRS.2002.805079

Sund M, Lauknes TR and Eiken T (2014) Surge dynamics in the Nathorstbreen glacier system, Svalbard. *The Cryosphere* **8**(2), 623–638. doi:10.5194/tc-8-623-2014

Todd J and Christoffersen P (2014) Are seasonal calving dynamics forced by buttressing from ice mélange or undercutting by melting? Outcomes from full-Stokes simulations of Store Gletscher, West Greenland. *The Cryosphere* **8**(6), 2353–2365. doi:10.5194/tc-8-2353-2014

Toutin T (2008) ASTER DEMs for geomatic and geoscientific applications: a review. *International Journal of Remote Sensing* **29**(7), 1855–1875. doi:10.1080/01431160701408477

van der Veen CJ (2013) *Fundamentals of glacier dynamics* 2nd Edn. CRC Press, Boca Raton, FL, USA, 389 pp.

Van Wychen W and 6 others (2014) Glacier velocities and dynamic ice discharge from the Queen Elizabeth Islands, Nunavut, Canada. *Geophysical Research Letters* **41**(2), 484–490. doi:10.1002/2013GL058558

Willis MJ and 11 others (2018) Massive destabilization of an Arctic ice cap. *Earth and Planetary Science Letters* **502**, 146–155. doi:10.1016/Journalepsl.2018.08.049

Zemp M and 14 others (2019) Global glacier mass changes and their contributions to sea-level rise from 1961 to 2016. *Nature* **568**(7752), 382. doi:10.1038/s41586-019-1071-0

Hydrol. Earth Syst. Sci., 23, 4233–4247, 2019
https://doi.org/10.5194/hess-23-4233-2019

Hydrology and Earth System Sciences
Open Access

River-ice and water velocities using the Planet optical cubesat constellation

Andreas Kääb[1], **Bas Altena**[1], **and Joseph Mascaro**[2]

[1]Department of Geosciences, University of Oslo, Oslo, 0316, Norway
[2]Planet, San Francisco, 94103, USA

Correspondence: Andreas Kääb (kaeaeb@geo.uio.no)

Received: 5 February 2019 – Discussion started: 10 April 2019
Revised: 10 July 2019 – Accepted: 13 September 2019 – Published: 22 October 2019

Abstract. The PlanetScope constellation consists of ∼ 150 optical cubesats that are evenly distributed like strings of pearls on two orbital planes, scanning the Earth's land surface once per day with an approximate spatial image resolution of 3 m. Subsequent cubesats on each of the orbital planes image the Earth surface with a nominal time lag of approximately 90 s between them, which produces near-simultaneous image pairs over the across-track overlaps of the cubesat swaths. We exploit this short time lag between subsequent Planet cubesat images to track river ice floes on northern rivers as indicators of water surface velocities. The method is demonstrated for a 60 km long reach of the Amur River in Siberia, and a 200 km long reach of the Yukon River in Alaska. The accuracy of the estimated horizontal surface velocities is of the order of $\pm 0.01\,\mathrm{m\,s^{-1}}$. The application of our approach is complicated by cloud cover and low sun angles at high latitudes during the periods where rivers typically carry ice floes, and by the fact that the near-simultaneous swath overlaps, by design, do not cover the complete Earth surface. Still, the approach enables direct remote sensing of river surface velocities for numerous cold-region rivers at a number of locations and occasionally several times per year – which is much more frequent and over much larger areas than currently feasible. We find that freeze-up conditions seem to offer ice floes that are generally more suitable for tracking, and over longer time periods, compared with typical ice break-up conditions. The coverage of river velocities obtained could be particularly useful in combination with satellite measurements of river area, and river surface height and slope.

1 Introduction

Knowledge about water surface velocities on rivers supports the understanding of a wide range of processes. In cold regions, river-ice freeze-up, and in particular break-up, and the associated transport of and action by ice debris is often the most important hydrological event of the year; this transport produces flood levels typically exceeding those of other periods (Fig. 1) and associated dramatic consequences for river ecology and infrastructure (e.g. Prowse et al., 2007; Kääb and Prowse, 2011; Rokaya et al., 2018a). River discharge measurements are complicated during freeze-up and break-up due to the physical impact of ice on instrumentation, and the determination of water surface speeds from tracking river ice floes can aid with estimating discharge (Beltaos and Kääb, 2014). This possibility is of particular importance for the major Arctic rivers of North America and Siberia, which transport large amounts of freshwater into the Arctic Ocean; however, the discharge of these rivers is least known for the ice break-up period – notably the period during which annual discharge peaks (Zakharova et al., 2019).

In addition to in situ measurements and ground-based remote sensing (e.g. Lin et al., 2019), water surface velocities are mainly retrieved using airborne or space-borne radar interferometry (Romeiser et al., 2007). During periods when rivers carry ice floes, or other visible surface objects, water velocities can be measured using near-simultaneous satellite (or airborne) images, optimally with time separations of the order of minutes (Kääb and Leprince, 2014). Such near-simultaneous imaging of the Earth surface is provided by satellite stereo sensors, where two or more stereo image partners are, by necessity, temporally separated by approximately 1–2 min (Kääb and Leprince, 2014). Ice floes (or

Published by Copernicus Publications on behalf of the European Geosciences Union.

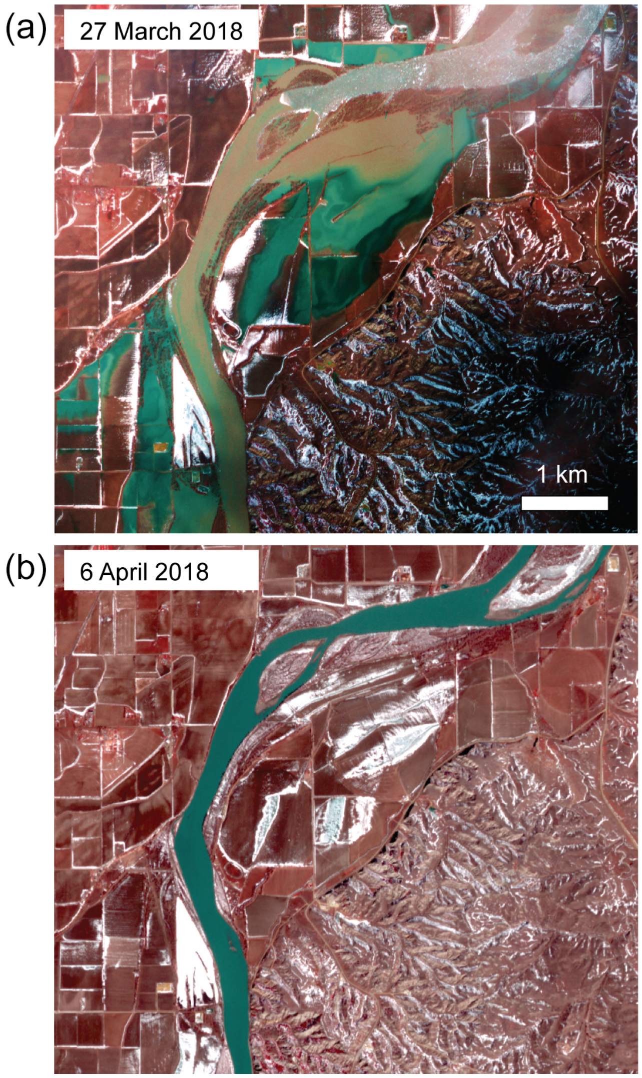

Figure 1. Planet images over an ice jam on the Yellowstone River at Sidney, Nebraska, USA (47.75° N, 104.09° W). The river flows from bottom to top (north). **(a)** The ice jam (top) and associated flooding. **(b)** After break of the ice jam.

other floating objects) are then tracked over this time lag to estimate water surface velocities during the image acquisition period. Satellite stereo imaging that is useful for this purpose stems from either fixed stereo or agile stereo. (In principle, satellite video could also be used to track ice floes but has to our knowledge not been demonstrated for this purpose yet; d'Angelo et al., 2014, 2016.) Fixed stereo is provided by two or more fixed cameras with different along-track viewing angles, e.g. the ASTER or ALOS PRISM sensors. Agile stereo is provided by one single camera that is rotated during overflight to point repeatedly to the same ground target, e.g. the WorldView or Pleiades satellites. Kääb and Prowse (2011) demonstrated the method deriving river-ice and water velocities over reaches of a few tens of kilometres of the Mackenzie and St. Lawrence rivers in Canada, using both types of satellite stereo images. Kääb et al. (2013) used ASTER fixed satellite stereo to measure and analyse river-ice flux and water velocities over a 600 km long reach of the Lena River in Siberia. Finally, Beltaos and Kääb (2014) demonstrated how water surface velocity fields derived in this way can be used to estimate river discharge. While Kääb and Leprince (2014) may have indicated other seasons and satellite constellations to track river ice floes over short time spans, all of the above studies have the following in common: (i) they use images during ice break-up for the most part, (ii) they use dedicated stereo systems, and (iii) they mostly use rare and opportunistic acquisitions. Point (i) limits the application of the method to one short time period of the year, and (ii) and in particular (iii) prevent the method from being applied operationally and systematically over large reaches of many rivers. The PlanetScope cubesat constellation offers the new, currently unexplored possibility of performing systematic worldwide observations of river-ice velocities and the water velocities indicated by them. The primary aim of the present study is to demonstrate and explore these possibilities, and the secondary aim is to evaluate the estimation of water velocities during river freeze-up, instead of during break-up. As the main focus of this study is a methodological one, we do not study the selected hydrological, hydraulic, or geomorphological applications that seem possible in detail.

The PlanetScope optical cubesat constellation scans the Earth surface systematically and daily (Figs. 2 and 3) involving the overlap of consecutive acquisitions with a time lag of around 1.5 min. A time lag of this order is perfectly suited to track floating matter, in particular river ice floes. Thus, PlanetScope offers the possibility of systematic daily measurement of water surface velocities, as long as ice floes are present on the water and sky conditions are clear. In this study, we first introduce the PlanetScope cubesat constellation in more detail. After a description of the methods used to track ice floes over minute-scale time lags, we demonstrate and discuss the typical ice-floe conditions suitable for tracking, and derive velocities over a 60 km long reach of the Amur River, Siberia, and a 200 km long reach of the Yukon River, Alaska. We also discuss the error budget of the measurements in detail. Finally, we draw conclusions regarding the potential for systematically measuring river-ice and water velocities from the PlanetScope constellation and briefly sketch out the possible fields for the application of this method.

2 The Planet cubesat constellation

The following descriptions of the PlanetScope constellation and data, and the methods used, are an update and specification of the descriptions given by Kääb et al. (2017). The Planet cubesat constellation, referred to as PlanetScope, consists of small 10 cm × 10 cm × 30 cm satellites. Their main components are a telescope and CCD area array sensor. One

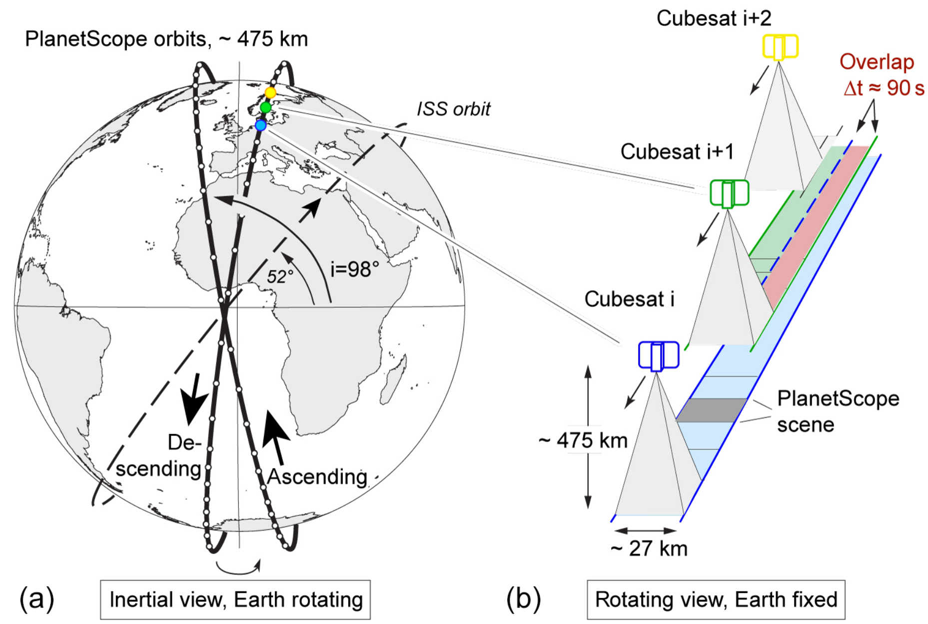

Figure 2. Planet orbits. **(a)** Inertial view: the final PlanetScope descending and ascending orbits (bold) and the ISS test-bed orbit (dashed). Cubesat positions (white dots on the orbits) are only schematically indicated. **(b)** Rotating view: the complete scan scheme of the Earth surface by successive PlanetScope cubesats in the same orbit producing a time lag of around 90 s over the swath overlaps.

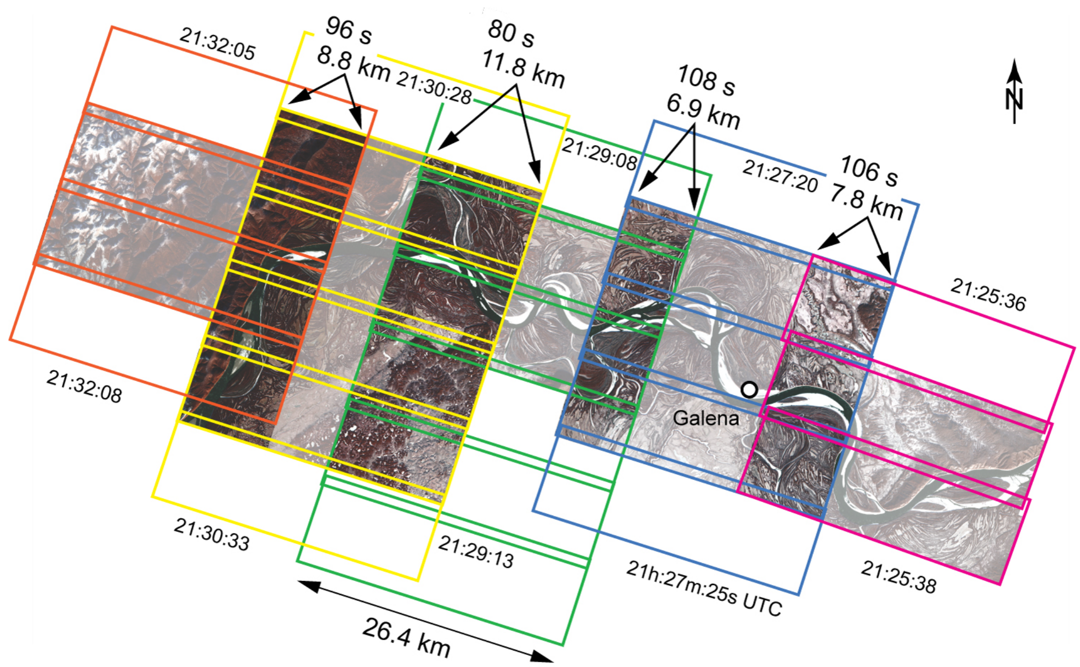

Figure 3. Typical PlanetScope acquisition pattern on a cloud-free day during freeze-up (28 October 2018) over the Yukon River at Galena, Alaska (64.75° N, 157° W). Each colour indicates one satellite swath with individual scenes. Non-dimmed parts of the image indicate scene sections where two images with a time lag between them exist and river ice floes can be tracked. The time lag and width of the overlaps are given along with the time (UTC) of the acquisitions.

half of the 6600 pixel × 4400 pixel CCD array acquires red–green–blue (RGB) data and the other half acquires near-infrared (NIR), both in 12 bit radiometric resolution. At the time of writing, the majority of the PlanetScope satellites provides images of about 3.7 m spatial resolution at an altitude of 475 km (delivered as resampled to 3 m; Fig. 1), and an individual scene size of roughly 25–30 km × 8–10 km (Planet Application Program Interface, 2019). While most other optical Earth observation instruments in space acquire in push-broom geometry (i.e. 1-D sensor arrays scanning in orbit direction), the data from the Planet satellites are 2-D frame images. Each complete image is taken at one single point in time, and has one single acquisition position and one single bundle of projection rays. For comparison, push-broom sensors integrate an image over a time interval of a few seconds so that acquisition time, position, and attitude angles vary throughout an image (Nuth and Kääb, 2011; Kääb et al., 2013; Girod et al., 2015).

Currently, the Planet cubesat constellation consists of around 150 cubesats following each other on two near-polar orbits of roughly 8 and 98° inclination respectively, and at an altitude of approximately 475 km (Fig. 2), imaging the Earth at local morning from both an ascending and descending orbit. The distance along the orbit between the cubesats is constructed such that the longitudinal progression between them over the rotating Earth leads to a void-less scan of the surface. Thus, the full constellation provides sun-synchronous coverage of the entire Earth (except the polar hole) with daily resolution (Fig. 2 in this paper ;Foster et al., 2015; Kääb et al., 2017). To guarantee this void-less surface imaging at all latitudes as well as when satellite positions and pointing angles are not exactly nominal, the swaths of subsequent cubesats overlap in the across-track direction by some kilometres (Figs. 2, 3). Within these swath-overlaps Earth surface targets are imaged twice (sometimes even more) with a time lag of roughly 1.5 min. This time lag is exploited in the present study and constitutes its core principle. The PlanetScope constellation also involves other time lags; however, these are not considered here (e.g. less than 1 s between RGB and NIR acquisitions; or a few hours, depending on the latitude, between acquisitions from ascending and descending orbits).

During the PlanetScope constellation's technological demonstration phase, the cubesats were mostly launched from the International Space Station into an orbit with a 52° inclination and an approximate 375 km height (Fig. 2 in this paper; Kääb et al., 2017). Data from these satellites form the majority of Planet's cubesat data archive holding for 2016 and into early 2017, before acquisitions from the near-polar sun-synchronous orbits took over. The build-up of the PlanetScope constellation and frequent replacement of its cubesats enables, among others, fast technological turnover and improvement of the image sensors. As a result, images from the more recent cubesat generations used in this study typically have better radiometric contrast than images from earlier generations.

3 Data and methods

Within the swath overlaps and over the corresponding approximate 1.5 min time lag we track river ice floes using standard image matching techniques. For image matching purposes, the geometric characteristics of repeat imagery are of particular interest. PlanetScope images are available at different processing levels, and here we use "analytic" data. Analytic data are radiometrically processed and orthorectified. We do not apply "unrectified" data, another processing level available, which comes with minimal radiometric processing and in the original central projection. The image orientation from on-board measurements is refined by Planet by matching the scenes onto a global reference mosaic (at the time of writing from Landsat, ALOS, and Open Street Map layers) and the images are orthoprojected using a digital elevation model (DEM). As for all orthoprojected satellite data, vertical errors in the orthorectification DEM cause lateral distortions in the resulting PlanetScope orthoimages. The size of these offsets is proportional to the DEM error and the off-nadir viewing angle (Kääb et al., 2016, 2017; Altena and Kääb, 2017). In a worst-case scenario for PlanetScope data (Kääb et al., 2017), a DEM error of 10 m results in orthorectification offsets of around 30 cm in the scene centre and 65 cm at the outer scene margin. For repeat river observations, the differential effect of these offsets can be reduced by co-registering the near-simultaneous images using stable points along shorelines. Over the limited width of rivers (a few kilometres at most), water surface topography is approximately planar. This means that a first-order polynomial co-registration model is sufficient to bring repeat unrectified frame images into overlap. This co-registration procedure will also greatly reduce offsets between the orthorectified analytic images used here, as the same DEM is used for both near-simultaneous images (Kääb et al., 2017). Errors in the DEMs used for orthorectifying PlanetScope images are a composite of (i) DEM elevation errors with respect to the real topography at the time of DEM acquisition, and of (ii) real-world elevation changes between the elevations at DEM acquisition and the elevations at satellite image acquisition. Orthorectification DEMs are, by necessity, outdated (although generally with limited consequences) unless acquired simultaneously with image acquisition. For river surfaces, the latter elevation deviations will primarily stem from water level variations between the DEM acquisition and the image acquisition dates. However, the small field of view of PlanetScope cubesats and the resulting low sensitivity to orthorectification DEM errors, the frame geometry of the PlanetScope cameras, and the accessibility of unrectified images, if needed, all contribute to minimize topographic distortions.

Bright ice floes on a dark water surface constitute features of strong visual contrast and tracking them over short time intervals is a particularly easy task for image matching algorithms. Thus, for matching the repeat PlanetScope data, we use a standard method – normalized cross-correlation (NCC) – solving the cross-correlation in the spatial domain and reaching sub-pixel accuracy by interpolation of the image (Kääb and Vollmer, 2000; Debella-Gilo and Kääb, 2011b; Kääb, 2014). NCC solves for translations between corresponding image elements. We apply the Correlation Image Analysis software (Kääb, 2014), but established scripts or routines for normalized cross-correlation between images exist for many programming languages. As the tracking of ice floes over short time intervals represents little challenge for image matching, we expect that other image matching methods (Heid and Kääb, 2012; Lin et al., 2019) would not provide a substantial advantage. However, over longer time intervals or strong horizontal water turbulence conditions, such as backwaters, ice-floe rotation over time would become significant; therefore, in these cases, image matching methods that are able to model feature rotation in addition to translation could be advantageous (Debella-Gilo and Kääb, 2012). The matching window sizes used in this study for the PlanetScope data are 30 pixels $\times$ 30 pixels (90 m $\times$ 90 m) as was found to be roughly optimal from a few tests. However, tests with different window sizes are not the focus of this study (Debella-Gilo and Kääb, 2011a). Measurements with a correlation coefficient smaller than 0.7 are removed and no other post-processing is applied (Kääb et al., 2017).

For comparing and supplementing our results based on Planet cubesats, we also use data from other satellites. A Landsat 8 scene from 16 September 2013 (i.e. ice-free conditions) is employed to automatically delineate the river water surface over the Yukon River study reach used in this work. Indexes used for the purpose of mapping water areas from multispectral satellite data are typically based on the reflectance contrast of water between blue (high reflectance) and near-infrared wavelengths (low reflectance) (McFeeters, 1996; Pekel et al., 2016). However, for our study site and conditions, we find that the contrast between the blue and thermal infrared Landsat bands is larger than the blue vs. infrared contrast due to a high suspended sediment concentration that increases the near-infrared reflectance and, thus, reduces the contrast to reflectance at blue wavelengths. To increase index sensitivity compared with the commonly used normalized difference indexes (McFeeters, 1996), we apply a band ratio. Thus, river outlines were obtained from a raster-to-vector conversion of a noise-filtered (3 $\times$ 3 median filter) and thresholded band ratio image (Paul et al., 2002) between the blue and thermal infrared bands of Landsat 8. The Landsat 8 blue band has 30 m spatial resolution, and the thermal infrared bands are also provided at a 30 m resolution, although they were originally taken at 60 m resolution.

For one of our Planet cubesat acquisition pairs over the Yukon River, a Sentinel-2 scene exists that was taken with a 1 h time difference. Sentinel-2 multispectral data have a spatial resolution of up to 10 m (Drusch et al., 2012; Kääb et al., 2016). We visually identified the position of a number of large ice floes corresponding between the Planet and Sentinel-2 images and measured the associated displacement along the river to estimate average velocities over the 1 h time period.

In order to compare the velocity retrieval from Planet cubesat data to a method used earlier for the same purpose we also measure short-term ice-floe displacements over the Yukon River reach from an Advanced Spaceborne Thermal Emission and Reflection Radiometer (ASTER) stereo strip. The ASTER fixed satellite stereo, taken at a 15 m spatial resolution and in near-infrared, implies a time lag of around 55 s between the two images of a stereo pair that can be exploited to track ice floes in a very similar fashion to the Planet cubesat images. The exact procedures, performance, and accuracies are presented in Kääb et al. (2013). As a speciality, satellite vibrations (so-called jitter) were modelled and corrected for when using the ASTER data. The results presented here for the Yukon River are based on a specially tasked ASTER acquisition, and have not been published before.

The river flow results of this study are presented as simple maps of measured velocity vectors or magnitudes, or as longitudinal profiles of water flow speed and derived parameters. For the latter we have to average the velocity vectors along the river reach. For that purpose, we move a running window, which is 4 km long in the reach direction and has infinite width, in 100 m steps along the mean direction of a study reach. The window length of 4 km and the step size of 100 m are experimentally chosen for our study sites to smooth the measurements substantially but at the same time leave enough detail.

At each window position, the number of measurement grid points within the river mask from Landsat 8 data as well as the average (or median) speeds and directions for the velocity measurements within the correlation threshold are computed. Dividing the number of grid elements within the river mask by the window length then gives an approximate river width for each step. This river width is then corrected for the deviation between the mean flow direction per window step against the overall mean direction of the river reach studied, essentially rotating the window at each step to align with the actual flow direction. (Note that other procedures exist that are more specialized for estimating river width when the flow vectors are not available; Allen and Pavelsky, 2018.) The surface area flux is then the multiplication of the average river speed and (corrected) width for each window step.

4 Results

4.1 River-ice conditions

Figure 4 illustrates a small subset of the typical river-ice conditions in Planet images that are suitable for tracking ice floes or ice features, and estimating water velocities. During break-up we find predominantly smaller ice floes with very variable densities of ice-floe cover (Fig. 4b, d, f, h). During freeze-up we typically find bigger ice floes and a more equal distribution of ice-floe cover density over the river surface. This simple description of differences between freeze-up and break-up ice conditions is an overall and qualitative one based on a substantial, although visual, exploration of Planet archive holdings; however, a range of exceptions and natural variations to this description certainly exist. Our extensive searches in the Planet image archive clearly suggest that the ice conditions that are suitable for tracking are more constant over time during river freeze-up and they stretch over longer time periods (up to approximately several days or even a week) compared with break-up conditions. Break-up ice conditions that are suitable for tracking typically only last one or several ice pulses of a few days at most, and often just a day or two. This makes it more probable to acquire/find images of suitable ice conditions during freeze-up than during break-up. However, for the northernmost latitudes, the freeze-up period reaches into the season of low sun angle, during which Planet cubesats (and other optical satellite instruments) no longer acquire data due to that fact that too little solar radiation reaches and reflects at the Earth's surface. Still, our clear overall impression is that it is typically easier to find Planet images that are suitable for tracking ice floes over freeze-up than over break-up periods.

4.2 Amur River, Siberia

For a first example of river-ice velocities retrieved from near-simultaneous Planet cubesat images, we mosaic two respective overlapping sets of 12 scenes into two image strips covering an approximately 60 km long reach of the Amur River near the city of Komsomolsk-on-Amur in eastern Siberia. The image strip pair was acquired on 1 November 2016 ($\sim$ 22:46 UTC) from an International Space Station (ISS) orbit, with a 73 s time lag. Figure 5a shows one of the two image strips as an infrared false colour composite. The freeze-up river-ice conditions during the acquisition were close to perfect for matching velocities. Ice floes densely covered most of the water surface, but were concurrently not colliding with each other in most areas; thus, the ice-floe velocities should to a large extent indicate water velocities at their locations. Ice-floe collisions would transfer additional lateral forces that overly the downstream drag by the river flow. Ice conditions on 1 November 2016 are shown in Fig. 6a. The diameter of visible ice floes generally ranges from around one pixel (3 m) to roughly 100 m, with a number of individual

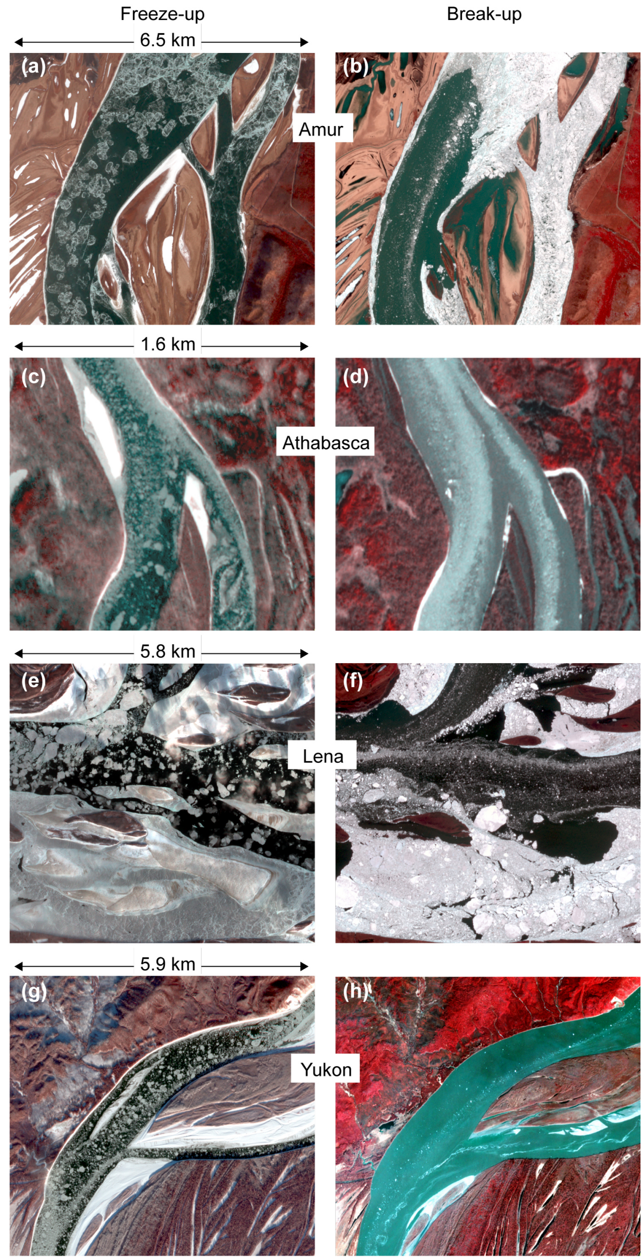

Figure 4. Typical river-ice conditions in Planet imagery (shown in infrared false colour) that are suitable for tracking ice floes to estimate water velocities. **(a, c, e, g)** During freeze-up; **(b, d, f, h)** during break-up.

floes reaching up to 200–300 m. Figure 5b shows the magnitudes of the velocities derived, with maximum speeds of $1.7\,\mathrm{m\,s^{-1}}$ close to the lowest elevation of the river reach investigated (right margin of Fig. 5b). The displacement measurements were carried out within a manually digitized polygon roughly delineating the river floodplain around the river. The same correlation threshold of 0.7 was applied to all measurements, both on the river and outside. Successful displacements (i.e. measurements that passed the correlation threshold) are dense on the river but sparse on the floodplain surrounding the river, as the surface there seems to consist mostly of homogenous shrubs that offer little visual contrast to match at the 3 m image resolution. The images used in this example over Amur River stem from an early generation of Planet cubesats providing images with lower radiometric contrast compared with images from the current Planet cubesats (see Sect. 2). In addition, the contrast is reduced by the low sun angle during the acquisition. Despite these two complications, matches of ice floes seem robust, with the accuracy and reliability affected little, as the bright floes offer particularly strong visual contrast against the surrounding dark water surface. In summary, on the one hand, the sparse displacements surrounding the river (scattered blue results in Fig. 5) reflect the lack of good visual contrast to match between the two images on the floodplain. On the other hand, the small magnitude of these sparse displacements confirms that the two images co-register well. Figure 6 shows the original velocity vectors measured in more detail (rectangle in Fig. 5). The grid spacing of the vectors is 75 m.

Figure 7 presents the longitudinal profile of speeds for the 1 November 2016 data set as well as the river width, which was automatically derived from the velocity vectors. Furthermore, we also compute the 2-D surface area flux as a function of transverse velocity profiles. As an example for the interpretation of the longitudinal profile, at approximately 25 km the 2-D surface area flux is relatively low, suggesting under mass conservation that the Amur River should be relatively deep at this part of the reach. In contrast, the river should be relatively shallow on average at, for instance, roughly 55 km. Interpretation of the longitudinal profile is influenced by the multi-branch geomorphology of the Amur River reach studied. In the individual speed measurements (grey dots in Fig. 7) branches become expressed by clusters of different speeds at the same reach section. For instance, at approximately 15–20 km, speeds on one branch are around $0.7\,\mathrm{m\,s^{-1}}$, whereas on the other branch they are up to $1.2\,\mathrm{m\,s^{-1}}$. Two clusters with different mean speeds on different branches are also clearly visible at around 30 km.

4.3 Yukon River, Alaska

For a second case study we chose an approximate 200 km long reach of the Yukon River in Alaska (Fig. 8). Over this reach, the overall river azimuth coincides with the azimuth of the near-polar descending orbit of the Planet cubesats. We mosaic respective sequences of around 25 scenes to obtain two image strips for 16 May 2017 ($\sim$ 21:12 UTC) with a 15 s time lag, and two images strips for 4 November 2018 ($\sim$ 21:30 UTC) with a 171 s time lag. Typical ice conditions for these acquisitions are demonstrated in Fig. 4h and g respectively. The diameter of visible ice floes on the 4 November 2018 images ranges from around one pixel (3 m) to 100 m or more. There are many large ice floes of up to around 100 m in diameter. Larger ice floes of up to around 200 m can be found but are less frequent than on the Amur River images (Sect. 4.2). For 16 May 2017, the ice-floe diameters are significantly smaller and typically do not exceed a few pixels. The velocity magnitudes derived are shown in Fig. 8c and e, speed differences between them are shown in Fig. 8d, and details of these three items are displayed in Fig. 9. For comparison to a method that was used earlier, we add river-ice speeds derived for 13 May 2014 from a strip of ASTER stereo pairs (i.e. 55 s time lag) following the method by Kääb et al. (2013) and compute differences to the 16 May 2017 Planet data set (Fig. 8a, b). On 13 May 2014, river-ice cover was comparably sparse and subsequently so was the density of successful velocity matches. The freeze-up conditions on 4 November 2018 clearly offered the most complete cover by river-ice floes and, thus, the most complete velocity field. The river outlines used in Figs. 8 and 9 were obtained from a Landsat scene from 16 September 2013 as described in Sect. 3. Visually, these outlines represent the actual outlines from May 2014 and May 2017 very well, without significant changes over time. At shallow river sections, outlines from November 2018 (i.e. low water conditions) were, of course, more narrow than for September 2013. However, the outlines produced here are only used for visualization and the initial result segmentation into the "river" and "outside river" classes for accuracy assessment on stable ground.

The closest river discharge measurements to the Yukon River reach used in this study are carried out at Pilot Station (no. 15565447), some 300 km downstream of the lower end of the reach studied. For 13 May 2014, 16 May 2017, and 4 November 2018 discharge estimates at Pilot Station are 11 383, 8410, and $5437\,\mathrm{m^3\,s^{-1}}$ respectively. Taking the distance between the reach investigated and Pilot Station into account, we also give the discharges 3 d later: 13 450, 11 213, and $4927\,\mathrm{m^3\,s^{-1}}$ for 16 May 2014, 19 May 2017, and 7 November 2018 respectively. Similar to the discharges, the surface velocities measured for 13 May 2014 are also higher than for 16 May 2017, and the latter values are higher than for 4 November 2018, as can be seen from Fig. 8b and d. The mean speed on 4 November 2018 is 0.80, whereas it is $1.35\,\mathrm{m^3\,s^{-1}}$ on 16 May 2017. Due to the sparse coverage by successful measurements in the ASTER data (Fig. 8a), only a few differences can be computed to the Planet data (Fig. 8b). The differences between the two Planet data sets (Fig. 8d) are much denser, demonstrating the advantage of the high-resolution Planet cubesat data in combination with the denser coverage by ice floes during the freeze-up. Speeds between 19 May 2017 and 7 November 2018 vary both with respect to the longitudinal average (Fig. 10b) and across the river (Figs. 8d, 9). In future applications, these measured spatio-temporal variations of surface water speed could be analysed in combination with known bathymetry and/or hydraulic formulae.

Figure 10a shows the longitudinal profile of speeds for the 4 November 2018 data set and the river width automatically derived from the velocity vectors. Furthermore, we also com-

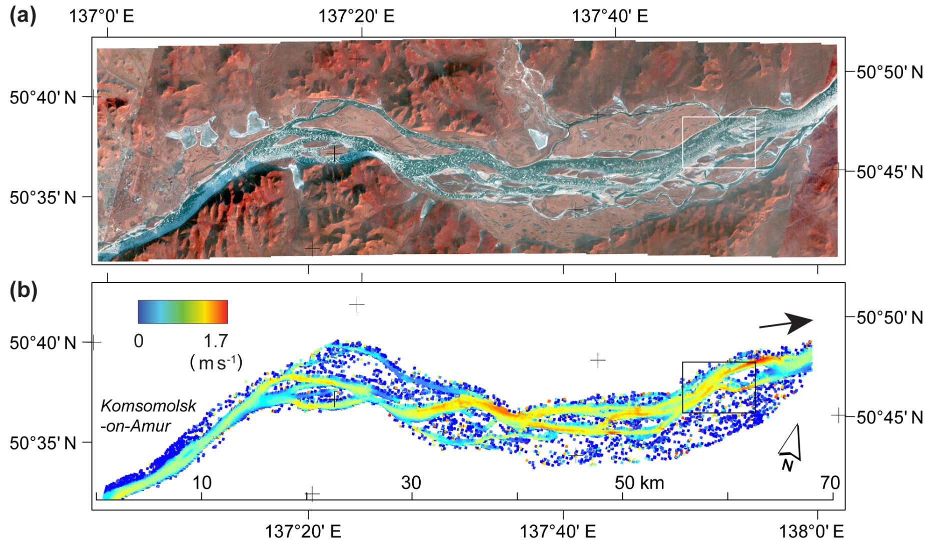

Figure 5. Amur River near the city of Komsomolsk-on-Amur, Siberia (lower left corner). River surface velocities on 1 November 2016 are tracked over a 73 s time lag between overlapping Planet cubesat images. **(a)** A false colour composite of one of the image strips, and **(b)** the derived surface speeds. The overall flow direction is from left to right. The small rectangle marks the location of the detailed image shown in Fig. 6.

pute the 2-D surface flux as a function of the transverse velocity profiles. As an example for interpretation of the longitudinal profile, at approximately 80 km, the 2-D surface flux is relatively low, suggesting under mass conservation that the Yukon River should be relatively deep at this part of the reach. In contrast, the river should be relatively shallow at on average, for instance, approximately 120 km.

From a similar profile of river surface speed along 400 km of the Lena River on 27 May 2011, Kääb et al. (2013) found a striking peak in the power spectrum of the river surface speed at 20.8 km. For the Yukon River profile in Fig. 10, we find a somewhat less prominent but still significant peak in the power spectrum of speeds at 20.5 km. The similar number for both river reaches might point to similar processes and parameters for the development of the respective river morphologies (Lanzoni, 2000a, b). Kääb et al. (2013) provide an additional discussion on the 20.8 km wavelength speed variations including comparison to a topographic profile.

The profile in Fig. 10b compares river surface speeds and river widths on 16 May 2017 and 4 November 2018. The four data sets are consistent in the sense of mass conservation: higher discharges in May 2017 compared to November 2018 (see above discharges for Pilot Station) correspond to a combination of larger widths and higher surface speeds. For instance, at sections where the river width is significantly larger in May 2017 than in November 2018, speed differences between May 2017 and November 2018 are smaller (e.g. at roughly 60, 110, or 170 km). Conversely, at sections with relatively small changes in river width, surface speeds change more (e.g. at roughly 30, 90, or 130 km).

4.4 Error budget

The error budget for individual river surface velocity measurements consists of three main components: (i) offsets in the absolute georeference of a set of repeat images, (ii) relative distortions and offsets between repeat images, and (iii) errors from the matching of features between the repeat images. The first category, the uncertainty of the absolute georeference, mostly stems from matching the Planet images onto a reference image. This step is part of the Planet in-house processing and is, in our experience, typically accurate to approximately one pixel or less, but can be larger for partially cloud-covered or snow-covered scenes. Failure or gross uncertainties of this georeference refinement step and subsequent gross georeference errors are flagged by Planet in the image metadata. To the best of our knowledge, an absolute georeference accuracy of a few metres or pixels for the locations of the velocities derived should not be a problem for most applications, in particular when considering that the velocities derived represent a window of several tens of metres (here 90 m × 90 m). The second category of uncertainty, the distortions and offsets between the images matched, can be minimized by co-registration, which is typically possible with sub-pixel accuracy. This uncertainty source is not necessarily eliminated for small-scale higher-order distortions (see Sect. 3) that differ between the stable ground used for co-registration (river shore, flood plain, etc.) and the actual river surface. The parts of this second error component that are not eliminated by image co-registration mix with the third error category, which is the actual matching accuracy for the respective stable ground or river-ice features. This relative matching accuracy between existing co-registered im-

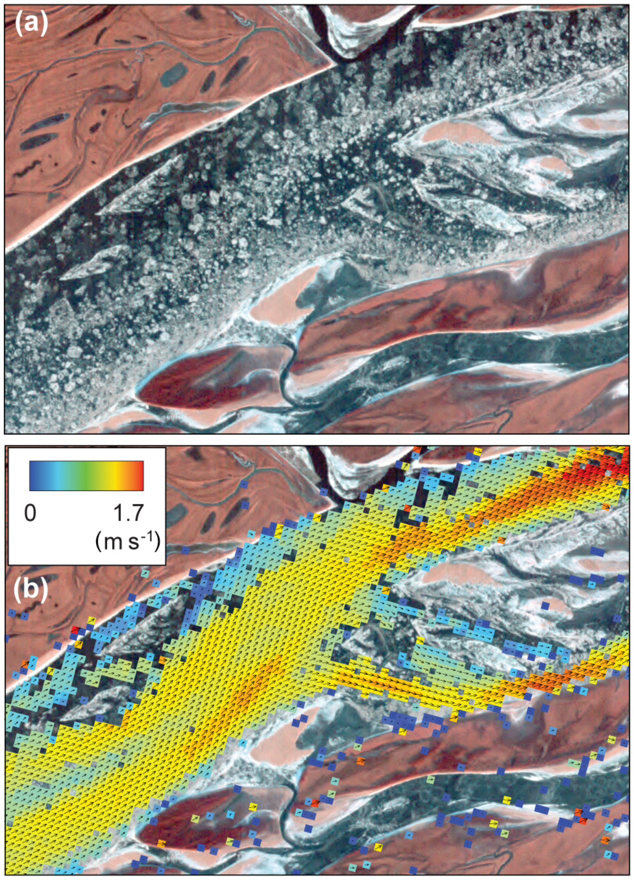

Figure 6. Detailed zoom-in of a section of Fig. 5 (see small rectangle in Fig. 5). **(a)** Planet cubesat image from 1 November 2016, and **(b)** the original matched surface velocities after the constraint of the correlation coefficient. The grid spacing of vectors is 75 m. Matching results are given with the speed colour-coded and with velocity vectors superimposed. The maximum speed was $1.7\,\mathrm{m\,s^{-1}}$.

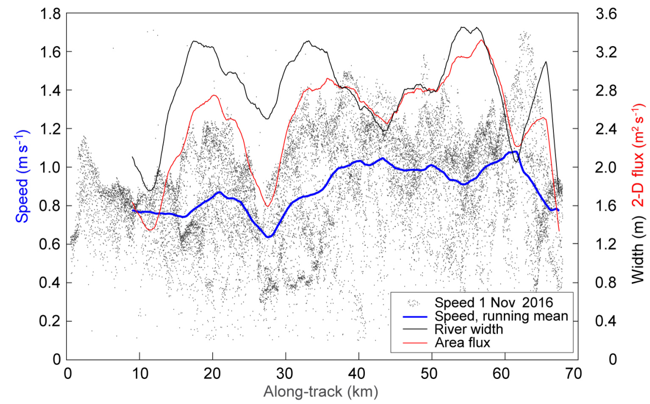

Figure 7. Longitudinal profile of mean speeds and river widths derived from near-simultaneous Planet cubesat images from 1 November 2016 over a reach of the Amur River (Fig. 5). Small dots represent individual speed measurements; the blue line represents the 4 km running mean of individual measurements; the black line represents the river width from velocities (running mean); the red line represents the surface area flux as a product of cross-sectional average speed and river width (running mean).

ages defines the uncertainty of the actual displacements or velocities derived; thus, here we consider it as the error component of largest interest (Kääb et al., 2013) and focus on it in more detail in the following.

Uncertainties of individual velocity measurements or outliers (our above error component iii) stem from uncertainties in the definition of river-ice features over time, i.e. how sharply features that change over time can be matched and how (precisely) is a displacement between slightly modified features defined. This error component includes the representativeness of displacements matched using a $90\,\mathrm{m} \times 90\,\mathrm{m}$ window for actual point-wise velocities, and the degradation of the matching accuracy by rotation or deformation of river-ice features over the minute-scale time lag exploited here (Kääb et al., 2013). We estimate the accuracy of our river-ice velocity measurements in the following three ways: (1) inference from previous studies, (2) stable ground matches, and (3) variance of velocities within homogenous parts of the derived flow field.

1. Based on ASTER data over the Lena river, Kääb et al. (2013) suggest a displacement accuracy of up to one-eighth of a pixel for most optimal imaging and ice conditions, which, in our case, would translate to about 0.4–0.5 m (or $0.005\,\mathrm{m\,s^{-1}}$ for a 90 s time lag).

2. Based on about 27 000 matches on the floodplains around the rivers investigated in this study we obtain a mean displacement dx of -0.1 ± 0.5 m, a dy of -0.2 ± 0.6 m, and a mean displacement length (Pythagoras of individual dx and dy) of 0.4 ± 0.6 m. Besides a good co-registration accuracy of around 0.2 m (i.e. about 1/15 of a pixel), our stable ground tests suggest an accuracy of the individual velocity measurements of ± 0.6 m (one-fifth of a pixel; $0.007\,\mathrm{m\,s^{-1}}$ for 90 s). This latter number agrees well with the accuracy estimates for co-seismic displacement measurements from repeat Planet data of one-fourth of a pixel (Kääb et al., 2017). Figure 10c shows a longitudinal profile of stable ground matches (in $\mathrm{m\,s^{-1}}$; black dots) for the 4 November 2018 data. The stable ground median speed is $0.02\,\mathrm{m\,s^{-1}}$, and the mean is $0.03\,\mathrm{m\,s^{-1}}$. Similar results are found for 16 May 2017. These values can be considered an upper limit for the accuracy of ice-floe measurements as the river ice floes offer better visual contrast for the matching than the areas surrounding the river (see Sect. 4.2), and the image areas outside of the river are likely subject to larger topographic distortions than the river surface (see Sect. 3).

3. Variations of velocities within the homogenous parts of the derived flow fields, i.e. the standard deviation of means over such parts of the flow fields, range be-

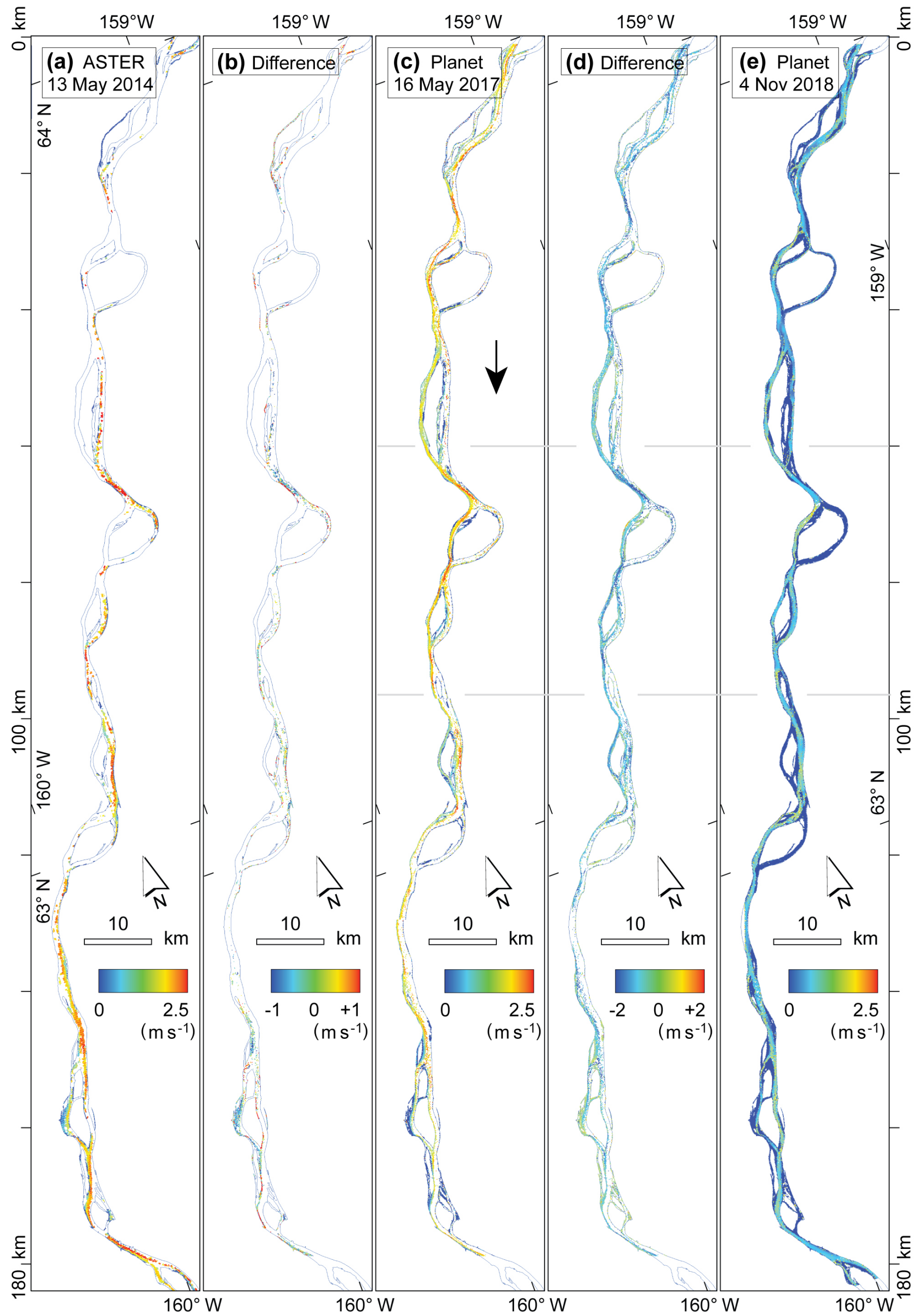

Figure 8. Surface velocities on the Yukon River, Alaska, from near-simultaneous satellite images. The flow direction is roughly from north to south (top to bottom of the figure). Velocities from **(a)** an ASTER stereo pair from 13 May 2014 (55 s time lag), **(c)** two Planet cubesat image strips from 16 May 2017 (15 s), and **(e)** two Planet cubesat image strips from 4 November 2018 (171 s). Panels **(b)** and **(d)** show the differences between **(c)** and **(a)** and the differences between **(e)** and **(c)** respectively. The horizontal grey lines in **(c–e)** indicate the detail shown in Fig. 9.

tween ± 0.3 m in our tests for the shortest time lag in our study (15 s; translating to $0.02\,\mathrm{m\,s^{-1}}$) and ± 3 m for our longest time lag (171 s; $0.02\,\mathrm{m\,s^{-1}}$). Especially for the longer time lags, deformations of the river-ice features matched and rotations of individual ice floes certainly degrade the actual matching accuracy.

From our above three approaches, as a rule of thumb, we suggest an accuracy of the order of $\pm 0.01\,\mathrm{m\,s^{-1}}$ for individual river-ice velocities derived from near-simultaneous PlanetScope data. Note that this accuracy improves following standard error propagation rules, once individual velocities

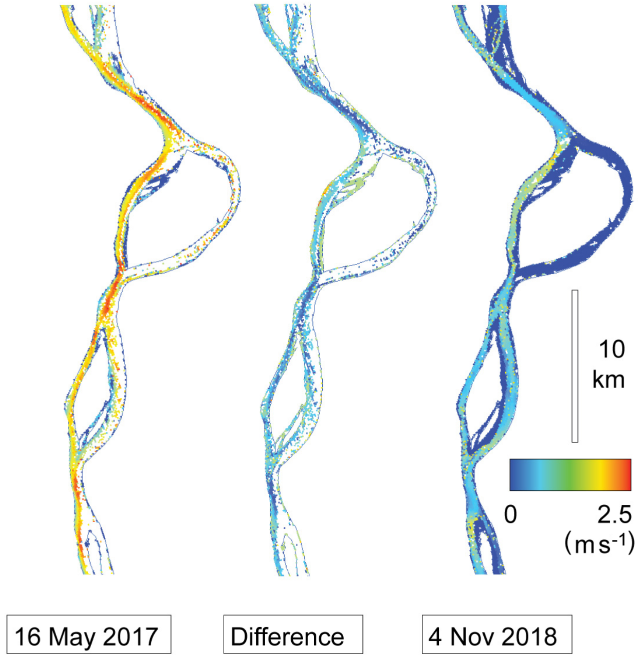

Figure 9. Detail of water surface velocities shown in Fig. 8. For more information see the caption of Fig. 8.

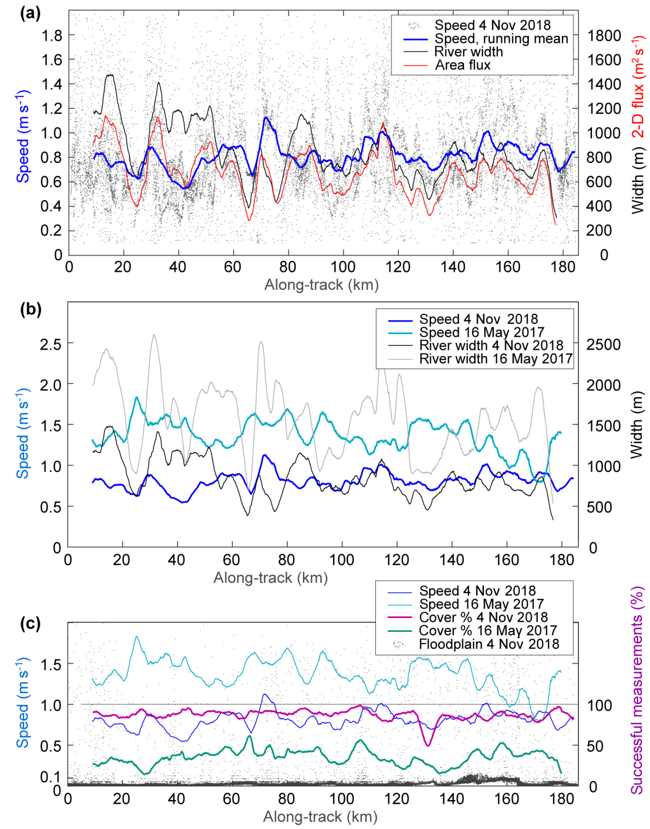

Figure 10. The longitudinal profile of speeds and river widths derived from near-simultaneous Planet cubesat images. **(a)** Measurements from 4 November 2018. Small dots represent the individual speed measurements; the blue line represents the 4 km running mean of individual measurements; the black line represents the river width from velocities (running mean); the red line is the surface area flux as a product of the cross-sectional average speed and river width (running mean). **(b)** The running means of surface speeds and the river width for 4 November 2018 (dark blue and black respectively) and 16 May 2017 (light blue and grey respectively). **(c)** Indicators of result quality. Small dots are speeds on stable ground for 4 November 2018, i.e. outside of the river. The green and turquoise lines are the percentage of successful measurements (i.e. measurements passing the correlation coefficient threshold) compared to the complete river mask. Blue and light blue lines in **(c)** are the speeds as in **(b)**.

are averaged, for instance for cross-sectional or longitudinal means.

As another possible indicator of measurement quality, Fig. 10c shows the percentage of successful matches on the river. Clearly, this percentage is much higher for the 4 November 2018 freeze-up conditions than for the 16 May 2017 break-up conditions on the Yukon River. This indicator can be used in several ways, for instance for masking out the results for reach sections with low values, for developing weighting of the above nominal accuracy, or for analysing unwanted dependencies between results and measurement density. The stable ground matches (dots in Fig. 10c) also exhibit errors in co-registration. For the 4 November 2018 data, a small co-registration problem can be seen at about 140–160 km with elevated speeds. Kääb et al. (2013) demonstrate a procedure to correct such offsets.

5 Discussion, conclusions, and outlook

In this study, we exploit the fact that the cross-track overlaps of the swaths of subsequent PlanetScope cubesats (Figs. 2 and 3) produce near-simultaneous optical acquisitions, separated by approximately 90 s. Over this time lag we track river ice floes and use them as indicators for water surface velocities. Planet cubesats scan the entire land surface of the Earth at daily repeat and with an approximate 3 m spatial image resolution. Our study shows that these data substantially extend the possibilities to measure river-ice and water surface flow from near-simultaneous optical satellite data. Over many rivers that carry river ice, ice floes can be tracked during freeze-up and/or break-up with accuracies of the order of $\pm 0.01\ \mathrm{m\,s^{-1}}$. Freeze-up conditions appear to be particularly well suited for this work due to the longer time periods over which ice floes are present, and the more favourable types and densities of ice floes.

We find three main obstacles when applying the method. By constellation design, the PlanetScope cross-track overlaps (never intended for measuring minute-scale changes and motions!) do not cover the entire Earth surface but only parts of it, depending on latitude, for instance two-thirds of a cubesat swath at 65° N (Fig. 3). Second, cloud cover seems rather typical for the river freeze-up and break-up seasons, and considerably complicates the acquisition of suitable Planet cubesat data – as for any optical satellite instrument. Third, freeze-up for some of the northernmost rivers or river reaches seems to occur during sun angles that are too low to acquire suitable images. As a very rough guess from our Planet cubesat archive searches, we estimate that there is a 50 % chance of getting a least one cubesat image per year with drifting ice visible for a given river location. The chances that the river location is then included in the swath overlap from a subsequent cubesat is lower, and the chances are considerably lower again when considering river locations that are covered several times (per year or in total) by overlaps that enable tracking. However, despite these limitations, the tracking of river ice in near-simultaneous Planet cubesat data substantially increases the possibilities for deriving surface velocities on cold-region rivers compared with the very few occasional optical stereo acquisitions suitable for the same purpose.

The strong visual contrast provided by the bright ice floes on the dark water surface, in combination with the short time lag of around 1 min exploited here, lead to few other motion components apart from translation and represent quite optimal conditions for image matching. Therefore, as our study is focused on evaluating the potential of the Planet cubesat constellation, not on the image matching algorithm, we used standard normalized cross-correlation (NCC) as the tracking method. Future work could test if other tracking methods have advantages over NCC for tracking ice floes in near-simultaneous satellite images. In particular for sea-ice tracking, other matching procedures are used that are optimized to work on sequences of low-resolution satellite data with time lags of hours to days (e.g. Lavergne et al., 2010; Petrou and Tian, 2017). An overview and assessment of state-of-the-art image-based tracking approaches for water flow measurements, in which some are certainly relevant for near-simultaneous Planet cubesat data, is given in Lin et al. (2019).

The parameters provisionally chosen for the moving windows to compute longitudinal flow averages (4 km length, 100 m step width) could easily be adjusted. Our visualizations turn out to be little sensitive to the exact choice of window parameter values. For the long river reaches studied here, the mean river direction defining the initial window orientations is almost identical to the orbit azimuth. Thus, the image matches on the floodplain outside the rivers can easily be transformed into their satellite along-track and cross-track components, which is a preferred coordinate system for analysing the geometric performance and errors in satellite data (Kääb et al., 2013). In the present study we do not find geometric errors of concern, such as satellite jitter, which Kääb et al. (2013) found and corrected in a similar study based on another satellite data type.

As we only use our longitudinal averaging procedure for visualization purposes, it is not optimized for specific applications such as estimating river width, discharge, or parameters of river morphology and flow. In particular, larger voids in the measured velocity field, due to low correlation coefficients, will bias the flow averages per window step. This effect seems strongly reduced for freeze-up conditions as the coverage by ice floes during these conditions typically appears to be much more complete compared with break-up conditions (see Sect. 4.1). River areas without ice floes only lead to voids in the measurements if they are larger than the matching window size (here 30 pixels $\times$30 pixels; 90 m $\times$ 90 m) in at least one dimension, as the matching algorithm used (NCC) is not sensitive to where the matched features are located in the window. A first measure to indicate problems from voids in the velocity field in the profiles is to plot the percentage of void pixels per window position (Fig. 10c). Smaller voids can be filled, whereby the measured velocities enable the application of a directional interpolator, or the matching window sizes can be automatically adapted to the distribution of ice floes – small windows for dense ice floes and larger ones for sparse ice floes (Debella-Gilo and Kääb, 2011a). The effect of voids on derived parameters can be tested by simulating voids for a rather complete data set (e.g. the Yukon River 4 November 2018) from actual voids in another data set (e.g. the Yukon River 16 May 2017) (McNabb et al., 2019).

Another effect to be taken into account is the influence of river branching on the averages. Again, treatment of this effect depends much on application and parameters of interest. For instance, the mean flow speed and surface area flux that we compute are not affected, whereas making connections between our surface flow measurements and river discharge would require taking branching into account. An initial simple procedure for that purpose would be to intersect the moving window at each step with the river outlines and to compute the flow averages for each intersection area separately.

Although not exploited further in this study, we would like to note the existence of a Sentinel-2 scene of 4 November 2018, taken about 1 h after the Planet scenes over Yukon River. Due to this large time lag between the Planet and Sentinel-2 scenes and the related large displacements and deformations/rotations of river-ice features, traditional image matching methods that solve only for translations are complicated, but manual tracking of distinct floes is still clearly possible. Tests show good agreement between the speeds derived over 1 h and those over 171 s. Thus, the fact that most Planet cubesats, Sentinel-2A and 2B, and Landsat 7 and 8 are on similar orbits can create additional opportunities for tracking river-ice movement, for investigating short-term changes in river-ice cover and speed, and for additional or combined multispectral mapping and analysis in combination with the Planet cubesats.

As demonstrated here for a 200 km long reach of the Yukon River, remotely-sensed water velocities over long reaches might offer improved insights into river morphology. For instance, we find a variation in water speeds of approximately 20–21 km wavelength for the Yukon River (and the Lena River; Kääb et al., 2013) that could be compared to according wavelengths found from laboratory experiments and models on bar formation (Lanzoni, 2000a, b).

A major purpose of satellite-based river observations is to estimate discharge in order to spatially or temporally complement the sparse in situ measurements available from gauging stations (Beltaos and Kääb, 2014; Bjerklie et al., 2018; Zakharova et al., 2019; and many others, see references in the cited ones). River velocities from the approach demonstrated here can offer an additional type of input measurement (or a possibility for independent comparison) when linking satellite-based measurements of river height and slope from altimetry data, and measurement of river surface from optical (Allen and Pavelsky, 2018) or radar images, to standard discharge equations (Bjerklie et al., 2018; Zakharova et al., 2019). Such satellite data are available over large regions (Allen and Pavelsky, 2018) and consequently fit well to the river velocities as derived by our approach. Satellite-altimetric river heights will even improve in the (near) future due to the new Sentinel-3 and high-resolution ICESat-2 missions (Brown, 2019), and the upcoming SWOT mission (Durand et al., 2010). Moreover, Landsat 8 and Sentinel-2 combined offer sub-weekly repeat to measure parameters such as river width.

In summary, the water mapping opportunities from the daily repeat Planet data (Cooley et al., 2017) and opportunities to measure ice velocities from them, as demonstrated here, could aid in detecting ice jams and related flooding (Fig. 1), as well as providing a better understanding of the mechanisms involved in ice jam formation. The damages from ice jam floods cause annual economic losses of the order of several hundred million EUR per year in North America and Siberia (Prowse et al., 2007; Rokaya et al., 2018a, b). Finally, while substantially fewer in number, we speculate that near-simultaneous overpasses of tropical and temperate rivers could similarly be exploited, tracking sediment or floating matter in place of ice (Kääb and Leprince, 2014).

Code availability. The image matching code used for this study (Correlation Image AnalysiS, CIAS) is available from http://www.mn.uio.no/icemass (Kääb, 2014).

Data availability. Sentinel-2 data are freely available from the ESA/EC Copernicus Sentinels Scientific Data Hub at https://scihub.copernicus.eu/ (Copernicus Open Access Hub, 2019); Landsat 8 data are available from USGS at http://earthexplorer.usgs.gov/ (USGS EarthExplorer, 2019); ASTER data are available from https://earthdata.nasa.gov/ (NASA Earthdata, 2019); Yukon River discharge data are available from https://waterdata.usgs.gov (USGS Waterdata, 2019). Planet data are not openly available as Planet is a commercial company; however, scientific access schemes to these data exist (https://www.planet.com/markets/education-and-research/).

Author contributions. AK developed the study, carried out most of the analyses, and wrote the paper. BA supported the analyses and edited the paper. JM helped with data acquisition, contributed technical details regarding the Planet constellation and data, and edited the paper.

Competing interests. AK and BA declare that they have no competing interests. JM was programme manager for impact initiatives at Planet. He in no way influenced the results or conclusions of the study.

Acknowledgements. Special thanks are due to two anonymous referees for their detailed and constructive comments, and to the editor of this paper. We are grateful to the data providers for this study: Planet for their cubesat data via the Planet's Ambassadors Program, ESA/Copernicus for the Sentinel-2 data, USGS for the Landsat 8 and river discharge data, and NASA and the ASTER science team at JPL for the ASTER data. Special thanks are due to Michael Abrams for tasking the May 2014 ASTER acquisitions over the Yukon River. This work was funded by the European Research Council under the European Union's Seventh Framework Programme, the ESA project Glaciers_cci, the ESA Living Planet Fellowship to Bas Altena, and the ESA EarthExplorer10 Mission Advisory Group.

Financial support. This research has been supported by the European Research Council (project: FP/2007-2013/ERC; grant no. 32081) and the European Space Agency (projects: 4000125560/18/I-NS and 4000109873/14/I-NB).

Review statement. This paper was edited by Bettina Schaefli and reviewed by two anonymous referees.

References

Allen, G. H. and Pavelsky, T. M.: Global extent of rivers and streams, Science, 361, 585–587, https://doi.org/10.1126/science.aat0636, 2018.

Altena, B. and Kääb, A.: Elevation change and improved velocity retrieval using orthorectified optical satellite data from different orbits, Remote. Sens.-Basel, 9, 300, https://doi.org/10.3390/rs9030300, 2017.

Beltaos, S. and Kääb, A.: Estimating river discharge during ice breakup from near-simultaneous satellite imagery, Cold Reg. Sci. Technol., 98, 35–46, https://doi.org/10.1016/j.coldregions.2013.10.010, 2014.

Bjerklie, D. M., Birkett, C. M., Jones, J. W., Carabajal, C., Rover, J. A., Fulton, J. W., and Garambois, P. A.: Satellite remote sensing estimation of river discharge: Application to the Yukon River Alaska, J. Hydrol., 561, 1000–1018, https://doi.org/10.1016/j.jhydrol.2018.04.005, 2018.

Brown, M.: Ice, Cloud, and Land Elevation Satellite-2 (ICESat-2) Applications: Monitoring Fresh Water Availability, available at: https://icesat-2.gsfc.nasa.gov/sites/default/files/ICESat-2_InlandWater_Whitepaper_040116.pdf, last access: 10 July 2019.

Cooley, S. W., Smith, L. C., Stepan, L., and Mascaro, J.: Tracking dynamic northern surface water changes with high-frequency Planet cubesat imagery, Remote Sens.-Basel, 9, 1306, https://doi.org/10.3390/rs9121306, 2017.

Copernicus Open Access Hub: Copernicus programme, European Commission and European Space Agency, available at: https://scihub.copernicus.eu, last access: 17 October 2019.

d'Angelo, P., Kuschk, G., and Reinartz, P.: Evaluation of Skybox Video and Still Image Products, Int. Arch. Photogram., XL-1, 95–99, https://doi.org/10.5194/isprsarchives-XL-1-95-2014, 2014.

d'Angelo, P., Mattyus, G., and Reinartz, P.: Skybox image and video product evaluation, Int. J. Image Data Fus., 7, 3–18, https://doi.org/10.1080/19479832.2015.1109565, 2016.

Debella-Gilo, M. and Kääb, A.: Locally adaptive template sizes in matching repeat images of Earth surface mass movements, ISPRS J. Photogram., 69, 10–28, https://doi.org/10.1016/j.rse.2010.08.012, 2011a.

Debella-Gilo, M. and Kääb, A.: Sub-pixel precision image matching for measuring surface displacements on mass movements using normalized cross-correlation, Remote Sens. Environ., 115, 130–142, https://doi.org/10.1016/j.rse.2010.08.012, 2011b.

Debella-Gilo, M. and Kääb, A.: Measurement of surface displacement and deformation of mass movements using least squares matching of repeat high resolution satellite and aerial images, Remote Sens.-Basel, 4, 43–67, https://doi.org/10.3390/rs4010043, 2012.

Drusch, M., Del Bello, U., Carlier, S., Colin, O., Fernandez, V., Gascon, F., Hoersch, B., Isola, C., Laberinti, P., Martimort, P., Meygret, A., Spoto, F., Sy, O., Marchese, F., and Bargellini, P.: Sentinel-2: ESA's optical high-resolution mission for GMES operational services, Remote Sens. Environ., 120, 25–36, https://doi.org/10.1016/j.rse.2011.11.026, 2012.

Durand, M., Rodriguez, E., Alsdorf, D. E., and Trigg, M.: Estimating river depth from remote sensing swath interferometry measurements of river height, slope, and width, IEEE J.-Stars, 3, 20–31, https://doi.org/10.1109/Jstars.2009.2033453, 2010.

Foster, C., Hallam, H., and Mason, J.: Orbit determination and differential-drag control of Planet Labs cubesat constellation, in: AIAA Astrodynamics Specialist Conference, August 2015, Vale, CO, available at: https://arxiv.org/pdf/1509.03270.pdf (last access: 17 October 2019), 2015.

Girod, L., Nuth, C., and Kääb, A.: Improvemement of DEM generation from ASTER images using satellite jitter estimation and open source implementation, Int. Arch. Photogramm. Remote Sens. Spatial Inf. Sci., XL-1/W5, 249–253, https://doi.org/10.5194/isprsarchives-XL-1-W5-249-2015, 2015.

Heid, T. and Kääb, A.: Evaluation of existing image matching methods for deriving glacier surface displacements globally from optical satellite imagery, Remote Sens. Environ., 118, 339–355, https://doi.org/10.1016/j.rse.2011.11.024, 2012.

Kääb, A.: Correlation Image Analysis software (CIAS), available at: http://www.mn.uio.no/icemass (last access: 10 July 2019), 2014.

Kääb, A. and Leprince, S.: Motion detection using near-simultaneous satellite acquisitions, Remote Sens. Environ., 154, 164–179, https://doi.org/10.1016/j.rse.2014.08.015, 2014.

Kääb, A. and Prowse, T.: Cold-regions river flow observed from space, Geophys. Res. Lett., 38, L08403, https://doi.org/10.1029/2011GL047022, 2011.

Kääb, A. and Vollmer, M.: Surface geometry, thickness changes and flow fields on creeping mountain permafrost: automatic extraction by digital image analysis, Permafrost Periglac., 11, 315–326, https://doi.org/10.1002/1099-1530(200012)11:4<315::Aid-Ppp365>3.0.Co;2-J, 2000.

Kääb, A., Lamare, M., and Abrams, M.: River ice flux and water velocities along a 600 km-long reach of Lena River, Siberia, from satellite stereo, Hydrol. Earth Syst. Sci., 17, 4671–4683, https://doi.org/10.5194/hess-17-4671-2013, 2013.

Kääb, A., Winsvold, S. H., Altena, B., Nuth, C., Nagler, T., and Wuite, J.: Glacier remote sensing using Sentinel-2. Part I: radiometric and geometric performance, and application to ice velocity, Remote Sens., 8, 598–622, https://doi.org/10.3390/Rs8070598, 2016.

Kääb, A., Altena, B., and Mascaro, J.: Coseismic displacements of the 14 November 2016 M_{w} 7.8 Kaikoura, New Zealand, earthquake using the Planet optical cubesat constellation, Nat. Hazards Earth Syst. Sci., 17, 627–639, https://doi.org/10.5194/nhess-17-627-2017, 2017.

Lanzoni, S.: Experiments on bar formation in a straight flume 1. Uniform sediment, Water Resour. Res., 36, 3337–3349, https://doi.org/10.1029/2000wr900160, 2000a.

Lanzoni, S.: Experiments on bar formation in a straight flume 2. Graded sediment, Water Resour. Res., 36, 3351–3363, https://doi.org/10.1029/2000wr900161, 2000b.

Lavergne, T., Eastwood, S., Teffah, Z., Schyberg, H., and Breivik, L. A.: Sea ice motion from low-resolution satellite sensors: An alternative method and its validation in the Arctic, J. Geophys. Res.-Oceans, 115, C10032, https://doi.org/10.1029/2009jc005958, 2010.

Lin, D., Grundmann, J., and Eltner, A.: Evaluating image tracking approaches for surface velocimetry with thermal tracers, Water Resour. Res., 55, 3122–3136, https://doi.org/10.1029/2018wr024507, 2019.

McFeeters, S. K.: The use of the normalized difference water index (NDWI) in the delineation of open water features, Int. J. Remote Sens., 17, 1425–1432, https://doi.org/10.1080/01431169608948714, 1996.

McNabb, R., Nuth, C., Kaab, A., and Girod, L.: Sensitivity of glacier volume change estimation to DEM void interpolation, The Cryosphere, 13, 895–910, https://doi.org/10.5194/tc-13-895-2019, 2019.

NASA Earthdata: National Air and Space Administration Earthdata, available at: https://earthdata.nasa.gov/, last access: 17 October 2019.

Nuth, C, and Kääb, A.: Co-registration and bias corrections of satellite elevation data sets for quantifying glacier thickness change, The Cryosphere, 5, 271–290, https://doi.org/10.5194/tc-5-271-2011, 2011.

Paul, F., Kääb, A., Maisch, M., Kellenberger, T., and Haeberli, W.: The new remote-sensing-derived Swiss glacier inventory: I. Methods, Ann. Glaciol., 34, 355–361, https://doi.org/10.3189/172756402781817941, 2002.

Pekel, J. F., Cottam, A., Gorelick, N., and Belward, A. S.: High-resolution mapping of global surface water and its long-term changes, Nature, 540, 418–422, https://doi.org/10.1038/nature20584, 2016.

Petrou, Z. I. and Tian, Y. L.: High-resolution sea ice motion estimation with optical flow using satellite spectroradiometer data, IEEE T. Geosci. Remote, 55, 1339–1350, https://doi.org/10.1109/Tgrs.2016.2622714, 2017.

Planet Application Program Interface: In Space for Life on Earth, San Francisco, CA, available at: https://api.planet.com/ and https://www.planet.com/, last access: 1 January 2019.

Prowse, T. D., Bonsal, B., Duguay, C. R., Hessen, D. O., and Vuglinsky, V. S.: River and lake ice, in: Global Outlook for Ice & Snow, United Nations Environment Programme, United Nations Environment Programme (UNEP), Nairobi, 201–214, 2007.

Rokaya, P., Budhathoki, S., and Lindenschmidt, K. E.: Trends in the timing and magnitude of ice-jam floods in Canada, Sci. Rep.-UK, 8, 5834, https://doi.org/10.1038/s41598-018-24057-z, 2018a.

Rokaya, P., Budhathoki, S., and Lindenschmidt, K. E.: Ice-jam flood research: a scoping review, Nat. Hazards, 94, 1439–1457, https://doi.org/10.1007/s11069-018-3455-0, 2018b.

Romeiser, R., Runge, H., Suchandt, S., Sprenger, J., Weilbeer, H., Sohrmann, A., and Stammer, D.: Current measurements in rivers by spaceborne along-track InSAR, IEEE T. Geosci. Remote, 45, 4019–4031, https://doi.org/10.1109/Tgrs.2007.904837, 2007.

USGS EarthExplorer: United States Geological Survey EarthExplorer, available at: https://earthexplorer.usgs.gov/, last access: 17 October 2019.

USGS Waterdata: United States Geological Survey, National Water Information System, available at: https://waterdata.usgs.gov, last access: 17 October 2019.

Zakharova, E. A., Krylenko, I. N., and Kouraev, A. V.: Use of non-polar orbiting satellite radar altimeters of the Jason series for estimation of river input to the Arctic Ocean, J. Hydrol., 568, 322–333, https://doi.org/10.1016/j.jhydrol.2018.10.068, 2019.

Observing the ice of our planet with daily cubesat imagery

Bas Altena

Department of Geosciences, University of Oslo

Keywords: Cryosphere, glaciers, optical remote sensing, kinematics, cubesats

Processes in, at or under a glacier occur at different timescales. For example, gravitational pull makes the ice in the glacier deform and flow like a viscous fluid. The magnitude of this internal deformation is mostly dependent on the ice thickness and its temperature. In a warmer climate, over the course of decades, the thickness might decrease (resulting in slower flow), and the ice might warm up (resulting in easier deformation) (Glen 1954). At an annual timespan it is mostly summer melting that results in an excess of meltwater, draining through surface crevasses to the glacier base. Here it is able to lubricate the ice-rock interface, reducing the friction and so letting the ice slip more easily.

Many processes that result in kinematics of glacial ice are shown in Figure 1. The size of the blobs corresponds to the score for the Deborah-number; that is the amount of relaxation over the observational timespan (Reiner 1964). This number assumes linear behaviour, which holds when continuous forces or slowly oscillating systems influence the movement. For example, the driving stress of a glacier is primarily dependent on the ice thickness, thus its creep flow can be considered continuous. A clear example of an oscillating system is the tidal forcing on ice shelves. For most of these processes the forcing is isolated. When complexity increases, displacements occur because of the interplay between different forces. Consequently, the nature of the signal can be perceived as sporadic.

Earth observation used to be observed at an annual or monthly cadence. Consequently, over long timespans processes of slip and viscosity might be separated. But the temporal and spatial resolution of observations has increased in recent years. Hence it is now possible to look at processes on shorter timescales. More complex processes can be measured and quantified. This opens-up a wealth of new insights, where new information can be extracted from established techniques. One can think of the monitoring of ice cauldrons, or time-dependent supra-glacial melt pond connectivity, precursor motion of calving icebergs, or full fjord circulation, just to name a few.

Glen, J. 1954. Experiments on the deformation of ice. *Journal of Glaciology* 12(2): 111–114.

Reiner, M. 1964. The Deborah number. *Physics today* 17(1): 62.

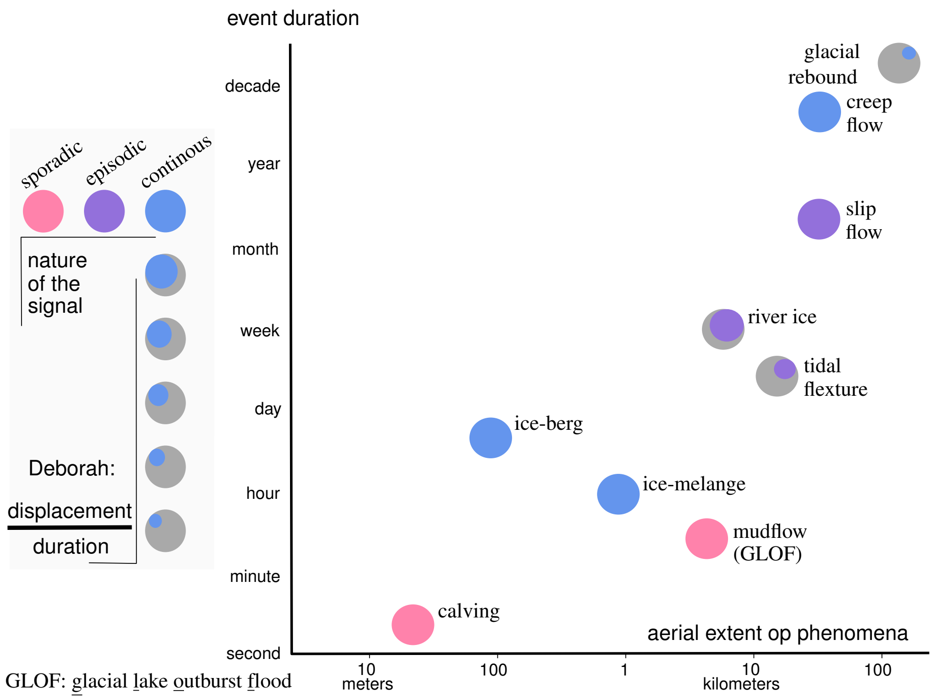

Figure 1: Stoffel diagram of the occurrence, duration and extent of different glacial events or glacier-related processes. Blob sizes correspond to the score for the Deborah-number.

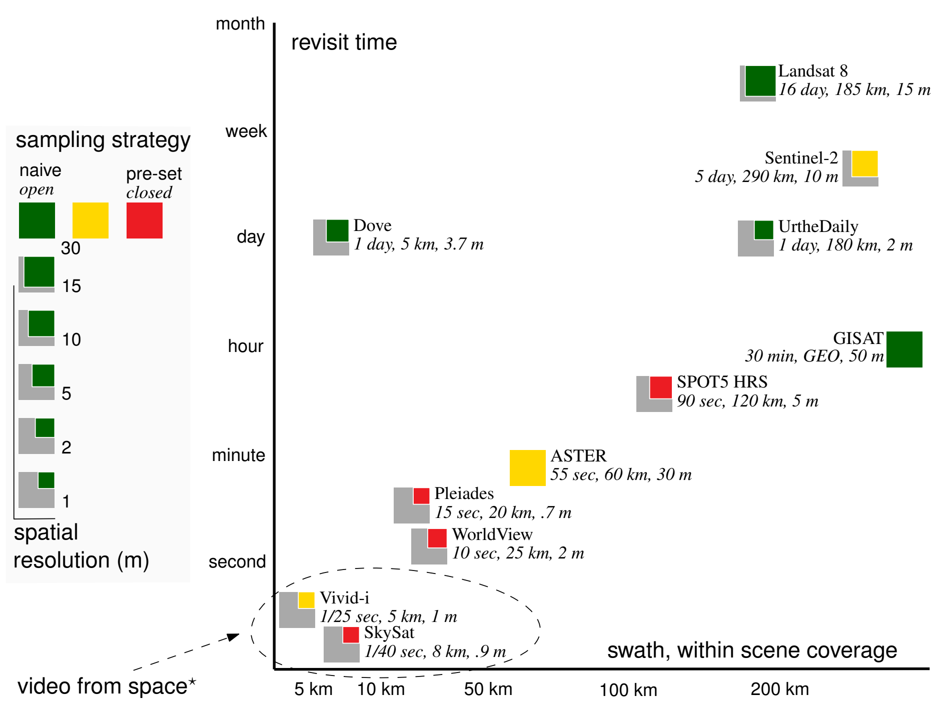

Figure 2: Geometric and temporal characteristics of a selection of present day optical remote-sensing constellations. The Vivid-i and SkySat satellites are video from space, thus for these systems the revisit rate corresponds to the frame rate of the video.*

MONITORING SUB-WEEKLY EVOLUTION OF SURFACE VELOCITY AND ELEVATION FOR A HIGH-LATITUDE SURGING GLACIER USING SENTINEL-2

Bas Altena[1],* Odin Næss Haga[1], Christopher Nuth[1], Andreas Kääb[1]

[1] Department of Geosciences, University of Oslo, 0371 Oslo, Norway
(bas.altena, odinh, christopher.nuth, kaeaeb)@geo.uio.no

Commission III, WG III/9

KEY WORDS: Glaciology, pushbroom photogrammetry, time-series, surface kinematics, Negribreen, Svalbard

ABSTRACT:

Currently, the Sentinel-2 twin satellite constellation of the Copernicus program is in operational mode and generates high repeat acquisitions at high-latitudes during polar day. These pushbroom satellites have a large field-of-view and are therefore ideal for simultaneous extraction of glacier displacement and elevation data. In this study we showcase the capabilities of this system set-up by generating time-series of glacier flow and elevation change over Negribreen, a tidewater glacier in Svalbard which nowadays is in its surge phase.

1. INTRODUCTION

The Sentinel-2 twin satellite constellation is part of the operational Copernicus monitoring system, and acquires medium resolution imagery with a wide field-of-view of 270 kilometers over the Earth surface for most of its sun-lit orbit. For only one satellite, its acquisition coverage at the equator resolves in a repetition rate of 10 days. Convergence of the orbits towards the poles cause this repetition rate to increase, as can be seen in Figure 1. Consequently, locations at high latitudes are observed from different angles, making across-track photogrammetry possible. This potential of Sentinel-2 has been demonstrated before by non-orthorectified images (Gaudel et al., 2017, Lacroix et al., 2018), but was limited to the calculation of a single elevation model.
The scope of this study is to introduce an approach that can exploit such highly redundant datasets at high latitudes, for example to monitor rapid glacier dynamical change. We use a surging glacier in Svalbard to demonstrate this potential because a glacier surge has both strong lateral and vertical changes within a short time period.

A glacier surge involves a rapid increase of glacier velocity, which can be several orders of magnitude faster than during its quiescent phase (Cogley et al., 2011). Surge events are accompanied by large transfer of ice mass from the accumulation area of the glacier towards lower elevations, often resulting in glacier terminus advance. In Svalbard a large fraction of the glaciers are of surge-type (Hamilton , Dowdeswell, 1996). Such classifications come from the observation that surge events seem to occur episodically on multiple glaciers. Sometimes the interval is semi-periodic (Eisen et al., 2005), but because of the long separation time (which can be in the order of several decades), not much is known about surges characteristics or changes thereof. When sufficient topographic data is available, the build-up of mass in the accumulation area during quiescence can be detected through elevation differencing and indicate surge susceptibility

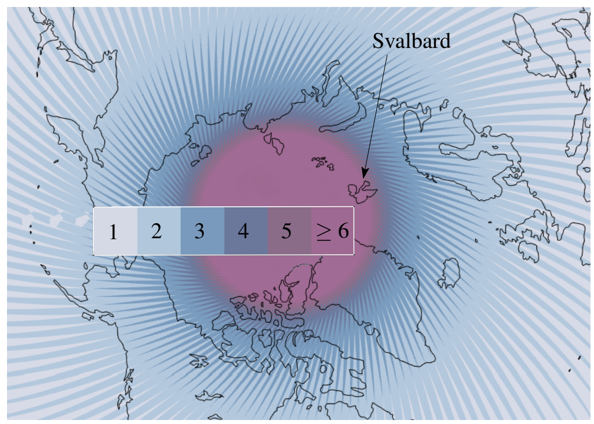

Figure 1. Illustration of the amount of times a point can be seen from the different orbits of Sentinel-2.

beforehand (Sund et al., 2009).

Recently a large glacier on Olav V Land in Northeast Spitsbergen has started to surge (Strozzi et al., 2017). The Negribreen glacier system has surged at least twice before, around 1870 and in 1935 (Lefauconnier , Hagen, 1991). Knowledge about specific characteristics of these previous surges is limited, though recent multibeam bathymetry in front of the glacier reveals the surge extent of the last event seems to have overridden the previous surge remnants (Ottesen et al., 2017).

In this study we investigate the possibility of simultaneously extracting horizontal velocity and vertical elevation change through time from a large collection of repeat multi-angle satellite images. Both parameters are partially independent, as the surface displacement may not reflect the topographic bulge of mass transfer (sometimes described as kinematic wave) often associated with surge events. During a surge, both of these processes may occur at different velocities (Raymond,

*Corresponding author: Bas Altena, bas.altena@geo.uio.no

1987). Hence, this makes the formulation photogrammetrically time-dependent and multi-temporal, as the two signals are super-imposed. To our knowledge this is the first demonstration of such a set-up, but is within the same family of work as (Kaufmann , Ladstädter, 2004, Li et al., 2017), though with different base data and assumptions.

2. DATA

A total of 246 images from the Sentinel-2 archive over Negribreen where manually selected and these are (partly) cloud free and taken during the polar days of 2016, 2017 or 2018. Data is acquired from eight unique relative orbits due to orbit convergence close to the poles (see Table 1), which produces redundant images taken from different zenith distances and with varying satellite bearings (azimuth). Displacements are matched between all possible pairs of cloud-free images that are within 100 days time separation. The network of displacements can be separated into three distinct graphs, because of the polar night and the limit of maximum desired time separation. This results in a total of 7763 displacement fields (see Figure 2) and groups of 1070, 2866, 3827 for the different graphs of 2016 to 2018, respectively. The increase in pairs over time is related to the launch of Sentinel-2B on the 23rd Jan. 2015, its transfer from commissioning phase towards operational and the start of the data transfer through the European Data Relay System.

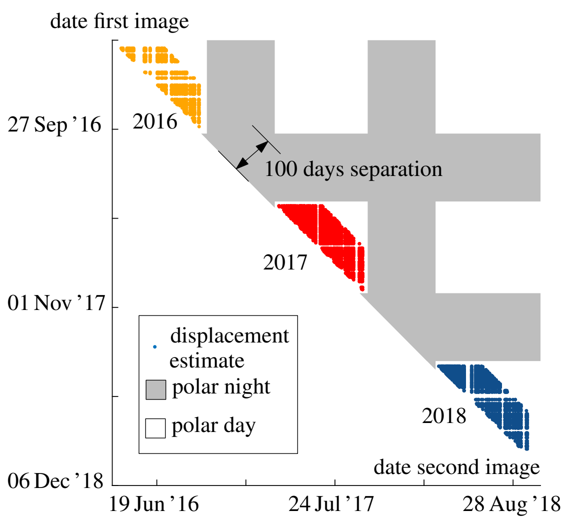

Figure 2. Temporal distribution of velocity fields. The shaded gray regions denotes the polar night when optical imagery is not available. Because of the limited timespan of 100 days, three distinct time periods are formed.

Sentinel-2 data is available in orthorectified form, and are orthorectified using (by necessity) an outdated elevation model (DEM) that does typically not represent glacier surfaces correctly due to their significant changes over time or steep topography(Kääb et al., 2016, Altena , Kääb, 2017, Ressl , Pfeifer, 2018). Therefore, Sentinel-2 data can be considered to be pseudo-orthophotos (Kaufmann , Ladstädter, 2004) for the application of glacier monitoring. Here we use standard image matching procedures (Leprince et al., 2007), in a pyramid structure and with an intermediate post-processing procedure (Westerweel , Scarano, 2005). The search range applied is 2560 meters (2^8 pixels), has three layers where the final template size is 320 meter (2^5 pixels), which is also the separation distance between different templates.

orbit	bearing ϕ [deg]	zenith θ [deg]
009	-136.4	-2.1
038	-126.9	+7.5
052	-134.0	+0.4
066	-141.1	-7.8
081	-124.5	+9.6
095	-131.7	+2.9
109	-138.7	-4.9
138	-129.3	+5.3

Table 1. Mean acquisition angles over Negribreen from different relative Sentinel-2 orbits.

3. METHODOLOGY

Here we adopt the formulation of pushbroom photogrammetry as in (Altena , Kääb, 2017) but extend parameter estimation with a time dependent elevation bias. In this way the vertical difference and horizontal displacement can be formulated as,

$$\underbrace{\left[\begin{array}{cc|cc} \delta t_{pq} & 0 & \tan\theta_p \cdot \cos\phi_p & -\tan\theta_q \cdot \cos\phi_q \\ 0 & \delta t_{pq} & \tan\theta_p \cdot \sin\phi_p & -\tan\theta_q \cdot \cos\phi_q \end{array}\right]}_{[\mathbf{A}_{pq}|\mathbf{C}_p\mathbf{C}_q]} \underbrace{\begin{bmatrix} \vec{v}(x)_{pq} \\ \vec{v}(y)_{pq} \\ \delta h_p \\ \delta h_q \end{bmatrix}}_{\mathbf{x}} = \underbrace{\begin{bmatrix} \vec{d}(x)_{pq} \\ \vec{d}(y)_{pq} \end{bmatrix}}_{\mathbf{y}}. \tag{1}$$

where
$\vec{d}$ = displacement measurement
δt = time interval
$\vec{v}$ = velocity estimate
ϕ = satellite bearing
θ = zenith distance
δh = vertical orthorectification bias
x, y = spatial coordinates
t = temporal coordinate
p, q = time instances

In this formulation the system of equations is ill-posed; there are more unknowns than measurments. When four images are included and all are matched with each other, then theoretically, this system can be solved ($n(n-1) > 2n - 1$ where n is the amount of images). Hence, the construction of the equations given in Eq. 1 can be placed into a larger matrix system as follows,

$$\begin{bmatrix} \vec{d}_{pq} \\ \vec{d}_{qr} \\ \vec{d}_{pr} \end{bmatrix} = \left[\begin{array}{cc|ccc} \mathbf{A}_{pq} & 0 & \mathbf{C}_p & \mathbf{C}_q & 0 \\ 0 & \mathbf{A}_{qr} & 0 & \mathbf{C}_q & \mathbf{C}_r \\ \mathbf{A}_{pr} & \mathbf{A}_{pr} & \mathbf{C}_p & 0 & \mathbf{C}_r \end{array}\right] \begin{bmatrix} \vec{v}_{pq} \\ \vec{v}_{qr} \\ \delta h_p \\ \delta h_q \\ \delta h_r \end{bmatrix}. \tag{2}$$

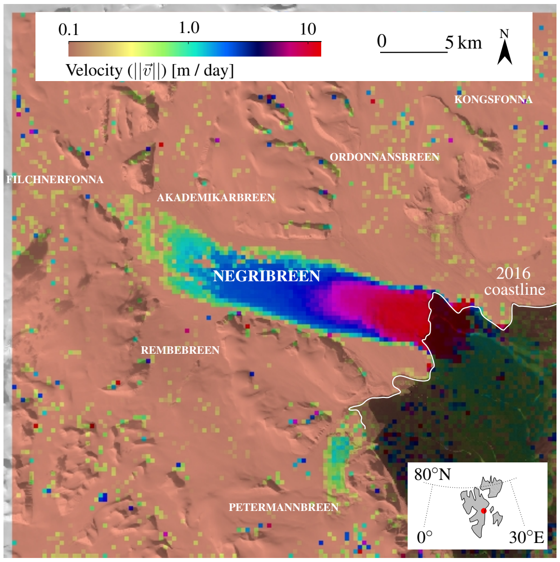

Figure 3. Estimated daily velocity of the Negribreen glacier system for April 2018.

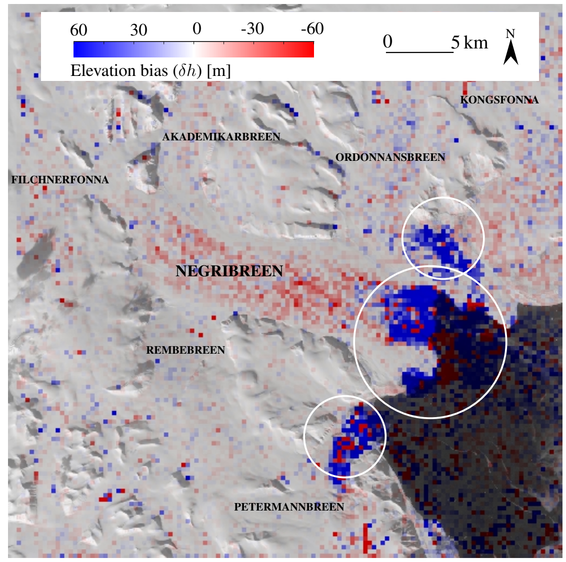

Figure 4. Orthorectification bias (δh, in equation2) over Negribreen glacier system for April 2018.

Recently time-series of displacement estimates from optical remote data has moved from pair-wise snapshot analysis towards network inversion (Bontemps et al., 2018, Altena et al., 2019), with networks formulated as above (though neglecting the geometric component **C**). However, the variance of the displacement estimates are non-Gaussian with heavy tails, consequently ordinary least squares estimation is not practical. When in addition the redundancy number is low, post-processing based on consensus voting might be best (Altena et al., 2019). While with a well connected network of displacements implementation of more advanced robust solvers is possible (Hadhri et al., 2019). Though for this show case, the measurement vector is substantially large ($n > 1000$), as well as, the amount of unknown parameters, which is unfavorable for least squares adjustment, as large matrices need to be inverted. Furthermore, a considerable amount of noise can be present, thus forcing one to use costly optimization methods. For these reasons we applied an adapted RANSAC (Fischler , Bolles, 1981) procedure instead. However, one downside of this methodology is that it hampers the possibility to weight the adjustment through, for example, their time separation.

4. RESULTS

Negribreen (78.5°N 19.1°E) is a 964 km^2 polythermal tidewater glacier in which a large portion of the glacier bed is located below sea level (Dowdeswell et al., 1984). The glacier tongue was stagnant prior to 2016 as horizontal velocity is practically inexistent. This suggests the tongue may have been frozen to the bed, as shown in other tidewater glacier surges (Nuth et al., 2019).

The active surge of Negribreen experiences the greatest flow (change) in the lower part of the glacier, as is shown in Figure 3. Resulting in a terminus advance of a couple of kilometers. Surrounding glaciers have considerably lower velocities and do not seem to be influenced by the surge. The only other fast flow occurs on Petermannbreen, a smaller tidewater glacier to the south which is not anymore connected to this glacier system.

The orthorectification bias (δh), i.e. elevation differences in respect to the reference elevation model, for the spring of 2018 (Figure 4) provides a strong alternating signal of draw down and elevation increase is present on Negribreen. For the interior of Negribreen a slight but clear negative elevation bias is present. At the glacier snout there is a clear elevation increase, in the location which used to be stagnant ice. The elevation increase is confined to a straight funnel, but a strong positive signal is also present at the calving front of Rembebreen. This sharp contrast does co-align with the coastline before the surge initiated. Other elevation increases can be seen at the snout

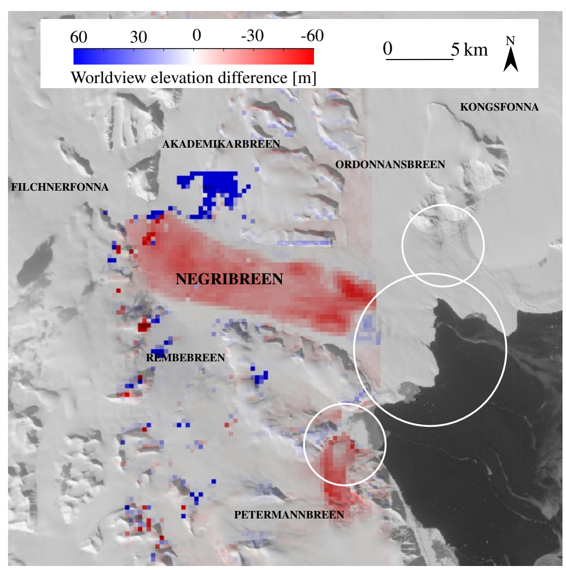

Figure 5. Elevation difference between Apr. 2014 - Aug. 2017, from ArcticDEM strip data.

of Petermannbreen and a partial uplift seems to occur on the lower parts of Ordonnansbreen.

These velocity and elevation patterns reflect the mechanisms described by (Nuth et al., 2019), in which a frozen glacier tongue hinders ice transport. After the glacier tongue destabilized in the spring of 2016, elevations have lowered in the accumulation area of Negribreen. However, the surge presently does not seem to influence other glaciers within the same system, except potentially the build-up of stagnant ice on Ordonnabreen. At the confluence of Negribreen with its neighboring Akademikarbreen and Rembebreen, surface slopes will increase due to elevation loss in the upper part of Negribreen. The resulting increase in driving stress might also be an agent to trigger surge instabilities on these glaciers, if this will be the case needs to be seen.

5. CONCLUSIONS

In this study we explore the possibility of simultaneous estimation of surface displacement and elevation change. This is accomplished with Sentinel-2 data, a high-repeat medium-resolution pushbroom satellite. The methodology is tested over a glacier in Svalbard, which recently entered a highly dynamic flow regime. Initial results hint towards a slow build-up of mass behind the glacier tongue followed by a sudden release. This caused backward propagation of velocity increases up-glacier, but its influence kept constrained to a narrow outlet. However, at the time of writing processing of the time-series is still happening, and interpretation and checking of our results is still necessary and envisioned. Though our initial results seem trustworthy as independent spaceborne elevation models (Porter et al., 2018) show similar spatial patterns and magnitudes, as can be seen in Figure 5. However, the sign of elevation difference is different for Petermannbreen, this might be due to a difference in timespan between the elevation data which are here compared and associated glacier dynamics prior to 2014. Unfortunately, the elevation data of WorldView is currently not covering the full glacier basin, neither is data available for 2018, yet.

The photogrammetric set-up of this system was not initially envisioned for Sentinel-2 (Drusch et al., 2012). However, in this study its potential and usefulness is demonstrated for the application of short-term glacier dynamics. It seems this set-up occupies a niche, which is not covered by any other spaceborne system. In this respect it is an improvement over other operational topographic systems, especially in respect to temporal coverage. Even though its precision might not be at the same level as dedicated photogrammetric missions, its continuous sensing makes temporal information extraction possible. Therefor we see this technique as complementary, and similar to timely but medium resolution topographic extraction methods as with the Planet constellation (Ghuffar, 2018).

The advantage of simultaneous extraction of elevation and kinematics over the same period, from the same sensor, increases the functionality of the data for modeling efforts. Typically, temporal alignment of velocity and topographic data is troublesome and additional interpolation is needed, however this is not the case for this integrated set-up. The set-up of this methodology is most suited for High Arctic glaciers, as at these high latitudes overlap is prominent (see Figure 1). Though this technique is still applicable in the lower Arctic, such as mainland Norway and Alaska, as the maximum intersection angle stays constant. This wide angle field of view for Sentinel-2 in combination with its medium resolution pixel resolution is essential for establishing a favorable base-to-height relation. While other popular sun-synchronous systems have less favorable configurations for the demonstrated photogrammetric extraction, as is listed in Table 2.

Another essential element for succes of this implementation is the improved absolute geo-referencing of Sentinel-2, especially in respect to older satellite systems. In our implementation we assume the lateral displacements can be solely attributed to ortho-rectification caused by an outdated elevation model and glacier movement. While for older satellites this co-registration has to be done on neighboring stable terrain (Rosenau et al., 2015, Fahnestock et al., 2016), or through stacking (Altena , Kääb, 2017), which would introduce an additional constrain within our system of equations. Hence given the advanced instrumentation of Sentinel-2, but also its high repeat, wide-angle and medium pixel resolution, this configuration occupies a sweet spot for monitoring of short term glacier dynamics in the Arctic.

Satellite system	Geometric characteristics			Retrieval precision	
	Height [km]	Width [km]	Pixel [m]	0.5px [m]	0.1px [m]
Resourcesat-2	817	140	23.5	137	27
Landsat 8	705	185	15	57	11
Sentinel-2	786	290	10	27	5
SPOT-5	832	60	5	69	13
PlanetScope	420	20	3	63	12

Table 2. Expected highest precision achievable for height retrieval through different sun-synchronous satellites.

ACKNOWLEDGEMENTS

This research is conducted through support from the European Union FP7 ERC project ICEMASS (320816) and the ESA projects Glaciers_cci (4000109873 14 I-NB) and ICEFLOW (4000125560 18 I-NS). Data from Sentinel-2 is made freely available through the Copernicus program and has been essential for this work.

REFERENCES

Altena, B., Kääb, A., 2017. Elevation change and improved velocity retrieval using orthorectified optical satellite data from different orbits. *Remote Sensing*, 9, 300.

Altena, B., Scambos, T., Fahnestock, M., Kääb, A., 2019. Extracting recent short-term glacier velocity evolution over Southern Alaska and the Yukon from a large collection of Landsat data. *The Cryosphere*, 13, 795-814.

Bontemps, N., Lacroix, P., Doin, M-P., 2018. Inversion of deformation fields time-series from optical images, and application to the long term kinematics of slow-moving landslides in Peru. *Remote Sensing of Environment*, 210, 144–158.

Cogley, J.G., Hock, R., Rasmussen, L.A., Arendt, A.A., Bauder, A., Braithwaite, R.J., Jansson, P., Kaser, G., Möller, M., Nicholson, L., Zemp, M., 2011. Glossary of glacier mass balance and related terms. Technical Report 86, International Association of Cryospheric Sciences, UNESCO-IHP, Paris, France.

Dowdeswell, J.A., Drewry, D.J., Liestøl, O., Orheim, O., 1984. Radio echo-sounding of Spitsbergen glaciers: problems in the interpretation of layer and bottom returns. *Journal of Glaciology*, 30, 16–21.

Drusch, M., Del Bello, U., Carlier, S., Colin, O., Fernandez, V., Gascon, F., Hoersch, B., Isola, C., Laberinti, P., Martimort, P., Meygret, A., Spoto, F., Sy, O., Marchese, F., Bargellini, P., 2012. Sentinel-2: ESA's optical high-resolution mission for GMES operational services. *Remote Sensing of Environment*, 120, 25–36.

Eisen, O., Harrison, W.D., Raymond, C.F., Echelmeyer, K.A., Bender, G.A., Gorda, J.L.D., 2005. Variegated Glacier, Alaska, USA: a century of surges. *Journal of Glaciology*, 51, 399–406.

Fahnestock, M., Scambos, T., Moon, T., Gardner, A., Haran, T., Klinger, M., 2016. Rapid large-area mapping of ice flow using Landsat 8. *Remote Sensing of Environment*, 185, 84–94.

Fischler, M.A., Bolles, R.C., 1981. Random sample consensus: a paradigm for model fitting with applications to image analysis and automated cartography. *Communications of the ACM*, 24, 381–395.

Gaudel, A., Languille, F., Delvit, J.M., Michel, J., Cournet, M., Poulain, V., Youssefi, D., 2017. Sentinel-2: Global reference image validation and application to multitemporal performances and high latitude digital surface model. *International Archives of the Photogrammetry, Remote Sensing & Spatial Information Sciences*, XLII-1/W1, 447–454.

Ghuffar, S., 2018. DEM generation from multi satellite PlanetScope imagery. *Remote Sensing*, 10, 1462.

Hadhri, H., Vernier, F., Atto, A., Trouvé, E., 2019. Time-lapse optical flow regularization for geophysical complex phenomena monitoring. *ISPRS Journal of Photogrammetry and Remote Sensing*, 150, 135-156.

Hamilton, G.S., Dowdeswell, J.A., 1996. Controls on glacier surging in Svalbard. *Journal of Glaciology*, 42, 157–168.

Kääb, A., Winsvold, S.H., Altena, B., Nuth, C., Nagler, T., Wuite, J., 2016. Glacier remote sensing using Sentinel-2. part I: Radiometric and geometric performance, and application to ice velocity. *Remote Sensing*, 8, 598.

Kaufmann, V., Ladstädter, R., 2004. Documentation of the movement of the Hinteres Langtalkar rock glacier. *International Archives of Photogrammetry and Remote Sensing*, 35, 893–898.

Lacroix, P., Bièvre, G., Pathier, E., Kniess, U., Jongmans, D., 2018. Use of Sentinel-2 images for the detection of precursory motions before landslide failures. *Remote Sensing of Environment*, 215, 507-516.

Lefauconnier, B., Hagen, J.O., 1991. *Surging and calving glaciers in eastern Svalbard*. Meddelelser, 116, Norwegian Polar Institute.

Leprince, S., Barbot, S., Ayoub, F., Avouac, J-P., 2007. Automatic and precise orthorectification, coregistration, and subpixel correlation of satellite images, application to ground deformation measurements. *IEEE Transactions on Geoscience and Remote Sensing*, 45, 1529–1558.

Li, R., Ye, W., Qiao, G., Tong, X., Liu, S., Kong, F., Ma, X., 2017. A new analytical method for estimating Antarctic ice flow in the 1960s from historical optical satellite imagery. *IEEE Transactions on Geoscience and Remote Sensing*, 55, 2771–2785.

Nuth, C., Gilbert, A., Köhler, A., McNabb, R., Schellenberger, T., Sevestre, H., Weidle, C., Girod, L., Luckman, A., Kääb, A., 2019. Dynamic vulnerability revealed in the collapse of an Arctic tidewater glacier. *Scientific Reports*, to appear.

Ottesen, D., Dowdeswell, J.A., Bellec, V.K., Bjarnadóttir, L.R., 2017. The geomorphic imprint of glacier surges into open-marine waters: examples from eastern Svalbard. *Marine Geology*, 392, 1–29.

Porter, C., Morin, P., Howat, I., Noh, M-J., Bates, B., Peterman, K., Keesey, S., Schlenk, M., Gardiner, J., Tomko, K., Willis, M., Kelleher, C., Cloutier, M., Husby, E., Foga, S., Nakamura, H., Platson, M., Wethington, M., Williamson, C., Bauer, G., Enos, J., Arnold, G., Kramer, W., Becker, P., Doshi, A., DSouza, C., Cummens, P., Laurier, F., Bojesen, M., 2018. ArcticDEM. *Harvard Dataverse*, V1. doi.org/10.7910/DVN/OHHUKH.

Raymond, C.F., 1987. How do glaciers surge? A review. *Journal of Geophysical Research: Solid Earth*, 92, 9121–9134.

Ressl, C., Pfeifer, N., 2018. Evaluation of the elevation model influence on the orthorectification of Sentinel-2 satellite images over Austria. *European Journal of Remote Sensing*, 51, 693-709.

Rosenau, R., Scheinert, M., Dietrich, R., 2015. A processing system to monitor Greenland outlet glacier velocity variations at decadal and seasonal time scales utilizing the Landsat imagery. *Remote sensing of environment*, 169, 1–19.

Strozzi, T., Paul, F., Wiesmann, A., Schellenberger, T., Kääb, A., 2017. Circum-Arctic changes in the flow of glaciers and ice caps from satellite SAR data between the 1990s and 2017. *Remote Sensing*, 9, 947.

Sund, M, Eiken, T, Hagen, JO, Kääb, A, 2009. Svalbard surge dynamics derived from geometric changes. *Annals of Glaciology*, 50, 50–60.

Westerweel, J., Scarano, F., 2005. Universal outlier detection for PIV data. *Experiments in fluids*, 39, 1096–1100.

Journal of Glaciology (2019), **65**(249) 136–148 doi: 10.1017/jog.2018.98

Closing the mass budget of a tidewater glacier: the example of Kronebreen, Svalbard

CESAR DESCHAMPS-BERGER,[1,2,3] CHRISTOPHER NUTH,[1] WARD VAN PELT,[4] ETIENNE BERTHIER,[2] JACK KOHLER,[5] BAS ALTENA[1]

[1]*Department of Geosciences, University of Oslo, PO Box 1047, Blindern, 0316 Oslo, Norway*
[2]*LEGOS, Université de Toulouse, CNES, CNRS, IRD, UPS, 31400 Toulouse, France*
[3]*CESBIO, UPS, CNRS, IRD, CNES, INRA, 31400 Toulouse, France*
[4]*Department of Earth Sciences, Uppsala University, 75236 Uppsala, Sweden*
[5]*Norwegian Polar Institute, Polar Environmental Centre, NO-9296 Tromsø, Norway*
Correspondence: César Deschamps-Berger <cesar.db@hotmail.fr>

ABSTRACT. In this study, we combine remote sensing, in situ and model-derived datasets from 1966 to 2014 to calculate the mass-balance components of Kronebreen, a fast-flowing tidewater glacier in Svalbard. For the well-surveyed period 2009–2014, we are able to close the glacier mass budget within the prescribed errors. During these 5 years, the glacier geodetic mass balance was -0.69 ± 0.12 m w.e. a^{-1}, while the mass budget method led to a total mass balance of -0.92 ± 0.16 m w.e. a^{-1}, as a consequence of a strong frontal ablation (-0.78 ± 0.11 m w.e. a^{-1}), and a slightly negative climatic mass balance (-0.14 ± 0.11 m w.e. a^{-1}). The trend towards more negative climatic mass balance between 1966–1990 ($+0.20 \pm 0.05$ m w.e. a^{-1}) and 2009–2014 is not reflected in the geodetic mass balance trend. Therefore, we suspect a reduction in ice-discharge in the most recent period. Yet, these multidecadal changes in ice-discharge cannot be measured from the available observations and thus are only estimated with relatively large errors as a residual of the mass continuity equation. Our study presents the multidecadal evolution of the dynamics and mass balance of a tidewater glacier and illustrates the errors introduced by inferring one unmeasured mass-balance component from the others.

KEYWORDS: glaciological instruments and methods, glacier mass balance, remote sensing

1. INTRODUCTION

Glaciers are a major contributor to global sea-level rise in the 20th and 21st century (Vaughan and others, 2013). Between 2003 and 2009, glacier mass losses represented ~30% of the total global sea-level rise (Gardner and others, 2013). Although the relative contribution of the Antarctic and Greenland ice sheets has been increasing, glaciers and ice caps remain a significant contributor to sea level change at present and in the near future (Marzeion and others, 2012; Huss and Hock, 2015). Locally, glaciers feed the downstream hydrological network with fresh water, impacting the physical properties of adjacent water bodies (Bourgeois and others, 2016; Sundfjord and others, 2017). Svalbard glaciers alone represent 5% of the global glacier area (Pfeffer and others, 2014), and accounted for 2% of the total glacier mass loss from 2003 to 2009 (Gardner and others, 2013). About half of this area is represented by tidewater glaciers (Pfeffer and others, 2014). Currently, the terminus of tidewater glaciers are retreating at rates up to several hundreds of metres per year in Alaska (McNabb and Hock, 2014), Greenland (Hill and others, 2017), the Russian Arctic (Carr and others, 2014) and Svalbard (Luckman and others, 2015), suggesting that these maritime glaciers are rapidly evolving and potentially rapidly responding to climatic and oceanic variations. Comparison with old glacier inventories show general terminus retreat of tidewater glaciers over the Svalbard archipelago since the 1930s despite some termini advance at the fronts of surge-type glaciers (Nuth and others, 2013). However, glaciers separated by only a few kilometres experienced very different retreat rates. The diversity of responses to similar forcing highlights the necessity to improve the understanding of tidewater glacier evolution (Carr and others, 2013).

The temporal evolution of glacier mass balance is a direct measure for the health state of a glacier and its contribution to global sea level. The total mass balance of tidewater glaciers is the sum of the climatic mass balance and the frontal ablation (Cogley and others, 2011), neglecting the basal mass balance. Total mass balance is often calculated using two approaches: (1) the geodetic method, which calculates the overall volume change combined with density assumptions to estimate mass change; and (2) the mass budget method, which sums the climatic mass balance and frontal ablation for tidewater glaciers. Frontal ablation comprises calving flux, melt and sublimation of the calving face (Cogley and others, 2011). For land-terminating glaciers, lack of frontal ablation allows cross-validation between climatic mass balance and geodetic mass balance (Zemp and others, 2013). However, similar assessments for tidewater glaciers (hereafter referred to as closure of the mass budget) are complicated by the difficulty to measure frontal ablation, mostly because it requires knowledge of ice thickness at the glacier front. To tackle the lack of measurements of bedrock topography on many glaciers, ice thickness has previously been inverted from surface velocity (Osmanoğlu and others, 2013; McNabb and Hock, 2014; Farinotti and others, 2017). When no surface velocity is available, frontal ablation has been calibrated using the terminus width (Gardner and others, 2011; Enderlin and others, 2014), glacier surface features (Błaszczyk and others, 2009), or seismic events recorded at nearby stations (Köhler and others, 2016). If frontal ablation cannot be measured or inferred using the above strategies, it can be estimated as a residual of the mass-balance equation (Rasmussen and others, 2011; Nuth and others, 2012). Furthermore, observations of all mass budget components are rarely available over a consistent period and region due to limited data availability. Space gravimetry from the GRACE mission provides an independent calculation of regional mass balance (Enderlin and others, 2014), but its low spatial resolution (hundredth of kilometres) is not sufficient to resolve the mass balance for individual glaciers.

In this study, we aim to close the mass budget of Kronebreen, a large dynamically active glacier system in Svalbard, using observations and model results. Previous results suggest that more than 90% of the mass loss is through frontal ablation (Nuth and others, 2012), though without quantitative verification. From 2009 to 2014, a unique dataset allows us to independently measure the three components of the mass budget from observations and models; frontal ablation, climatic mass balance and total mass change (Cogley and others, 2011). We use high-resolution satellite images and digital elevation models (DEMs) to quantify the geodetic mass balance as well as the frontal ablation. For the climatic mass balance, a state-of-the-art climatic mass balance model, calibrated by in situ stake measurements of ablation and accumulation, allows us to spatially and temporally extrapolate limited point observations as well as estimate volume–density fluctuations in the accumulation area. For our two earlier study periods (1966–1990 and 1990–2009), frontal ablation is not easily measurable due to a lack of continuous velocity fields from satellite images. However, datasets available allow the calculation of the geodetic and the climatic mass balances while frontal ablation is estimated as a residual from the mass-balance equation.

2. STUDY AREA

Kronebreen is a polythermal outlet glacier in the vicinity of Ny-Ålesund at 78°N, Svalbard, that drains ice from the Holtedahlfonna plateau (Fig. 1) into Kongsfjorden. Before reaching the fjord, Infantfonna Glacier (77 km^2) joins the main trunk 10 km upstream of the ice front. The Kronebreen glacier complex (KRB) comprises Kronebreen, Holtedahlfonna and Infantfonna. KRB covered 368 km^2 in 2014 with elevations ranging from sea level up to 1400 m a.s.l., among the highest accumulation areas in Svalbard. KRB has a 20 km-long common divide in the north with Isachsenfonna between 400 and 800 m a.s.l. The tidewater terminus of KRB is shared with Kongsvegen, to the south. KRB experienced a dramatic reduction of its calving front width when Kongsvegen surged in 1948 (Lefauconnier, 1992). Thereafter, KRB recovered the main share of the terminus before 1990 (Melvold, 1998). Today, with glacier flow speeds of up to 800 m a^{-1} close to the terminus, KRB is a continuously fast-flowing glacier with a large amount of dynamic ice export to the ocean up to 0.20 Gt a^{-1} (Luckman and others, 2015; Schellenberger and others, 2015). No surge has been observed on KRB, although

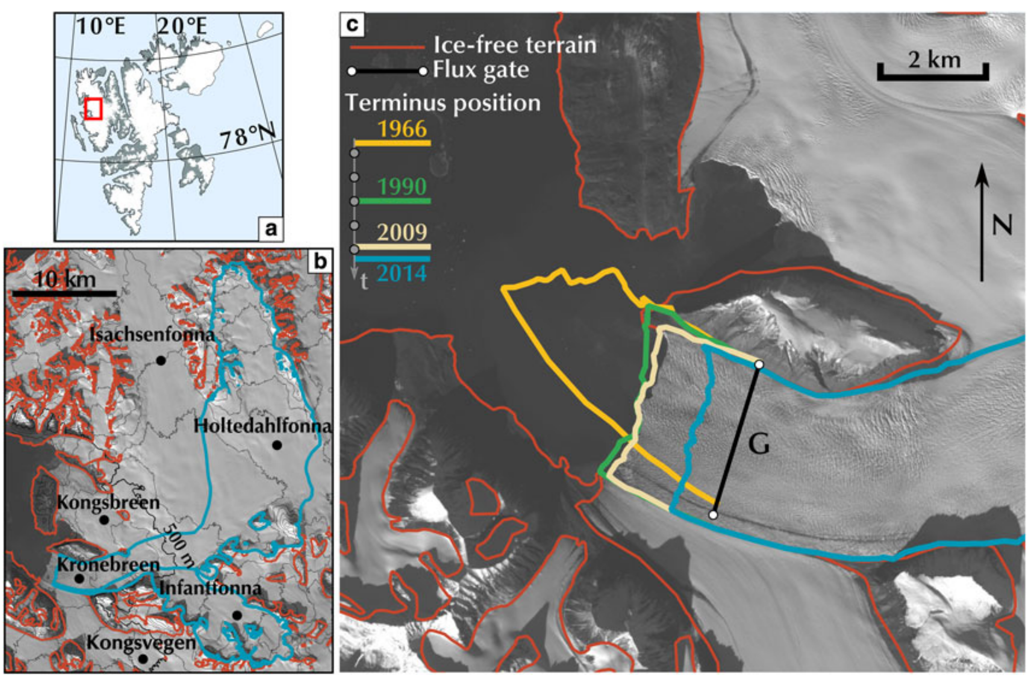

Fig. 1. (a) Study area on the west coast of the Svalbard archipelago. (b) Extent of Kronebreen, Infantfonna and Holtedahlfonna (blue line). Ice-free terrains are outlined in red. KRB is limited in the north by Kongsbreen and Isachsenfonna. It is joined 4 km before the terminus by Kongsvegen. (c) The terminus area. KRB terminus position for 1966 (yellow), 1990 (green), 2009 (beige) and KRB extent in 2014 (blue) are shown. The black line (*G*) shows the position of the flux gate used for the flux calculation. Background image is a SPOT5 image from 2007 (copyright CNES 2007, Distribution Airbus D&S, Korona and others, 2009).

descriptions of its terminus position in 1869 suggested it may have advanced recently from a surge (Melvold, 1998). The glacier terminus position has been generally retreating since the middle of the 20th century. It remained steady since the 1990s but has recently experienced a rapid retreat of more than 1 km between 2012 and 2016. As of 2018, the retreat is ongoing.

3. DATA

3.1. Geodetic volume change

Four Pléiades stereo pairs were acquired between 9 (two pairs), 16 and 25 August 2014 (Fig. 2). The panchromatic images have a resolution of 0.7 m at nadir. None of these acquisitions exhibited image saturation, a result of the 12-bit encoding and the low sun angle at the time of acquisition (Berthier and others, 2014). Four DEMs were calculated with the Ames Stereo Pipeline (Willis and others, 2015; Shean and others, 2016) and merged in a single DEM mosaic after co-registration on their overlapping areas. The DEM of 16 August 2014 is arbitrarily chosen as a reference to which the other DEMs are 3-D co-registered following the method proposed in Nuth and Kääb (2011). Horizontal and vertical shifts of several metres are removed, which reduced the median and normalized median absolute deviation (NMAD, Höhle and Höhle, 2009) of the elevation differences within the three overlapping areas to 1 m or less on the glacierized terrain (Table 1). An alternative DEM mosaic was created in which, after the 3-D co-registration, a correction of a tilt along the longitudinal and latitudinal axes was added. On steeper non-glacierized terrain, the spread of the elevation difference represented by the NMAD is up to 2.6 m, reflecting the sensitivity of DEM precision to surface slopes (Lacroix and others, 2015). In their overlapping areas, we average the elevations of all available DEMs to ensure a seamless mosaic (Fig. 2).

A 2009 DEM was generated from aerial images acquired on 1 August 2009 by the Norwegian Polar Institute (NPI). Images had a ground sampling distance of ~50 cm and an overlap of ~60% in the along-track direction. DEMs were generated using the software Socet GXP (https://www.geospatialexploitationproducts.com/content/socet-gxp/). The final DEM has a pixel spacing of 5 m and an estimated vertical precision of 1–2 m (Norwegian Polar Institute, Terrengmodell Svalbard, 2014).

The 1966 and 1990 DEMs were generated from aerial photographs in a similar way as above (Altena, 2008). Lack of texture in the original images, in particular the ones from 1990, led to a limited coverage of the DEMs in the upper accumulation areas. A kinematic GPS profile from 1996 is used to help constrain upper elevations in the 1990 DEM (Nuth and others, 2012). The 1966, 1990 and 2009 DEMs are referenced to mean sea level using a local geoid–ellipsoid conversion produced by NPI (personal communication from Harald Faste-Aas, 2016).

3.2. Climatic mass balance

The climatic mass balance between 1966 and 2014 is calculated using a coupled surface-energy-balance-snow model to simulate mass and energy exchange between the atmosphere, surface and underlying snow, firn and/or ice on a 100 m regularly spaced grid at a 3 h time resolution (Van Pelt and others, 2012; Van Pelt and Kohler, 2015). The model solves the surface energy balance to calculate surface temperature and melt, and simulates the subsurface evolution of temperature, density and water content. The model is primarily driven by output from the regional climate model HIRLAM (Undén and others, 2002; Reistad and others, 2011), complemented with weather station data from the Ny-Ålesund meteorological station, provided by the Norwegian Meteorological Institute. The model is calibrated by in situ surface mass-balance measurements from stakes along the centreline of KRB. A complete model description, including the model setup, calibration and validation for KRB and Kongsvegen, can be found in Van Pelt and Kohler (2015).

3.3. Frontal ablation

Frontal ablation $\dot{A}_f$ is defined as the combined loss of calving icebergs, subaerial melt, subaerial sublimation and subaqueous frontal melting (Cogley and others, 2011). It can be measured by the sum of the discharge through the terminus position at the end of each studied period (1990, 2009 and 2014) and the mass change resulting from the advance or retreat of the terminus position during a period (e.g. Dunse and others, 2015). We estimate discharge through a single flux gate (Fig. 1) by combining a time series of surface velocity fields from 2009 to 2014 (Köhler and others, 2016) and measurements of glacier thickness from ground-penetrating radar (Lindbäck and others, 2018). From 2009 to 2013, 2 m resolution FORMOSAT-2 images were acquired at 2–5 weeks intervals while monoscopic Pléiades images (0.7 m resolution) were acquired at a roughly monthly interval between April and August 2014. Images were orthorectified using ground control points extracted from a 5 m 2007 SPOT5-HRS orthoimage and DEM (Korona and others, 2009) and the 2014 Pléiades DEM produced for this study

Table 1. Shift vector removed by co-registration between Pléiades DEMs of the 9 and 25 August 2014 and the reference 16 August 2014 DEM (Easting, Northing, *Z*)

	Shift *m*			Median dh *m*		NMAD dh *m*		*N* dh #		Mean slope °	
Scene	Easting	Northing	*Z*	On Gla	Off Gla	On Gla	Off Gla	On Gla	Off Gla	On Gla	Off Gla
9 August 2014 (west)	4.05	−19.00	3.36	−0.01	0.39	0.36	2.06	7.4×10^6	0.6×10^6	1	8
9 August 2014 (north)	−0.98	−1.83	1.19	0.01	–	0.27	–	2.3×10^6	0	0.5	–
25 August 2014	−1.25	−1.36	−3.28	0.03	0.18	1.04	2.60	2.0×10^6	0.6×10^6	2.4	9.4

Statistical metrics of the elevation difference (Median dh and NMAD dh) after co-registration in metres on the glacier and off the glacier (i.e. stable terrain) provide a measure of the uncertainty of the high-resolution satellite product. *N* dh is the number of points in the area qualified.

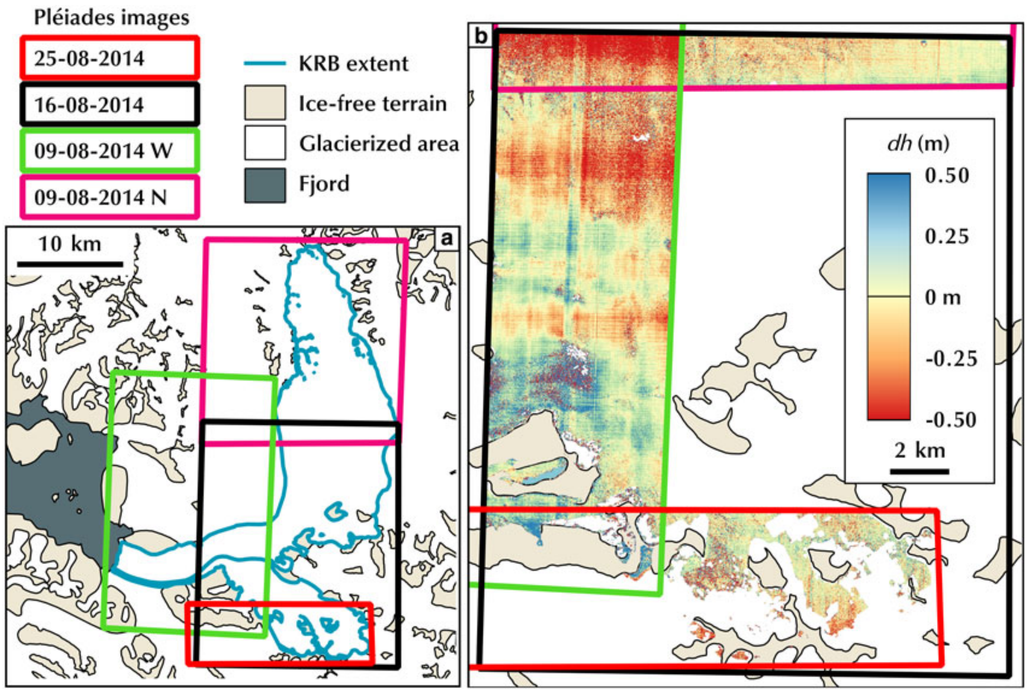

Fig. 2. (a) Extent of the different Pléiades scenes colour-coded with the date of the acquisition. (b) Elevation difference (in metres) between the different Pléiades DEMs over their overlapping areas.

(details in Köhler and others, 2016). The bed elevation and the surface DEM at the beginning of a period are combined to calculate the volume changes due to changes in the terminus position.

3.4. Additional datasets

Glacier outlines are necessary to spatially integrate the components of the mass budget. Masks of the glacierized and non-glacierized terrains in each DEM are based on the multi-temporal inventory derived from the original 1966, 1990 and 2007 DEMs (Nuth and others, 2013), and included in GLIMS (Raup and others, 2007) and the Randolph Glacier inventory (Pfeffer and others, 2014). The glacier outlines are held constant in the accumulation area through the different time periods (i.e. ice divides are assumed stable) and only updated in the glacier terminus area where large changes occurred. Calving front positions were manually digitized from the DEMs or orthophotos. The KRB outline is well constrained by outcrops and nunataks, neighbouring glaciers and the fjord water at the front. Yet the exact location of the ice divide between KRB and Kongsbreen/Isachsenfonna remains uncertain. We test the sensitivity of our results to different locations of the ice divide (see Discussion).

4. METHODS

4.1. Mass-balance equation

The basic formulation of our mass budget approach is:

$$\dot{M} = \dot{B} + \dot{A}_{\mathrm{f}}, \tag{1}$$

where $\dot{M}$ is the total glacier mass balance, $\dot{B}$ is the climatic mass balance (including surface and subsurface processes of internal accumulation and refreezing) and $\dot{A}_{\mathrm{f}}$ is the frontal ablation (including calving flux, melt and sublimation of the calving face). The overdot denotes derivative with respect to time and capital letters quantities summed for the entire glacier. We estimate KRB total mass balance with the geodetic method, $\dot{M}_{\mathrm{g}}$, and the mass budget method, $\dot{M}_{\mathrm{mb}}$. The geodetic method requires a conversion factor, ρ, to convert the total volume change, $\dot{V}$, into mass change (Eqn (2)). Note that ρ is not equivalent to material density in our method.

$$\dot{M}_{\mathrm{g}} = \rho \times \dot{V}. \tag{2}$$

The mass budget method relies on the calculation of the frontal ablation, $\dot{A}_{\mathrm{f}}$ and the climatic mass balance, $\dot{B}$:

$$\dot{M}_{\mathrm{mb}} = \dot{B} + \dot{A}_{\mathrm{f}}. \tag{3}$$

Frontal ablation is the most difficult quantity to estimate as (i) the bed elevation or ice thickness is first required, and (ii) continuous velocity fields are needed, which is generally achieved only for more contemporary periods (post 2000). Therefore, Eqns (1) and (2) can be re-arranged to estimate frontal ablation as a residual, by the difference between the climatic mass balance ($\dot{B}$) and the geodetic mass balance ($\dot{M}_{\mathrm{g}}$):

$$\dot{A}_{\mathrm{f}} = \dot{B} - \dot{M}_{\mathrm{g}}. \tag{4}$$

In this paper, we will distinguish between 'measured' and 'estimated' values. The former are directly derived from observations and from the model, whereas the latter are estimated from the residual of the mass continuity equation (Eqn (4)). All the terms of the mass-balance equation can be independently calculated for the period 2009–2014. These independent approaches are used to test our ability to close the mass budget. If not specified, mass-balance components are expressed as specific mass balance, which means a rate of change per surface unit. Additionally, we estimate emergence velocities for each elevation bin of the glacier from the residual of the observed elevation change and the modelled climatic elevation change. Upward velocities are taken as positive.

4.2. Geodetic mass balance

The geodetic mass balance is the sum of the mass change by change in the terminus position, $\dot{q}_t$, and by surface elevation changes over the glacierized area, $\dot{M}_{\mathrm{gla}}$. These two components are measured, respectively, by subtracting a surface DEM and the bedrock elevation over the retreated area (see Frontal ablation) and by subtracting two surface DEMs over glacier area. The 1966, 1990 and 2009 DEMs are first converted to WGS84 ellipsoidal heights. The 1966, 1990 and 2014 DEMs are then co-registered to the 2009 DEM using the ice-free terrain, which is unevenly distributed within the coverage of the combined DEMs. Co-registration performance is evaluated using the median and NMAD of the elevation differences on the ice-free terrain, ranging in absolute values from 0.02 m to 0.66 m and 0.84 m to 4.42 m, respectively, between two successive DEMs (Table 2).

Glacier volume change upstream of the terminus position at the end of a period is obtained from the elevation differences using a hypsometric approach, which overcomes the existence of small data gaps in maps of elevation differences. In this approach, the glacier is discretized into 50 m elevation bands (i) from which the mean of the differences, $\bar{\dot{h}}_i$, are calculated after removing outliers larger than three times the NMAD around the median. The total glacier volume change is obtained by multiplying the $\bar{\dot{h}}_i$ with the area A_i of each elevation bin and then summing through all the elevation bands:

$$\dot{V} = \sum_i \bar{\dot{h}}_i \times A_i. \tag{5}$$

The total volume of the glacier is calculated similarly by integrating elevation difference between a DEM and the bed elevation over the whole glacier. Elevation data are lacking in the 1990 DEM above 700 m a.s.l. and replaced by a differential GPS profile acquired along the centreline in 1996 with an accuracy of ~0.25 m. The profile is raised by a vertical shift of +3.69 m, the value identified in the 5 km of the 1996 profile that overlaps the 1990 DEM. This assumes that changes from 1990 to 1996 are uniform in the overlapping part, between 670 and 720 m a.s.l., and above.

Finally, the volume changes are converted into water equivalent mass change by multiplying by a volume change to mass change conversion factor ρ (Eqn (2)). Huss (2013) proposed using 850 ± 60 kg m^{-3} for land-terminating glaciers without significant frontal ablation. Here, we use a larger value of 900 ± 100 kg m^{-3} for the glacierized area as we believe that most KRB mass changes occur at higher density (see Discussion). We use the value of ice density for the volume change downstream the terminus position at the end of the period.

The volume change uncertainty $e_{\dot{V}}$ results from error in the elevation difference map $e_{\dot{h}}$ as well as error in the glacier area e_A:

$$e_{\dot{V}} = |\dot{V}|\sqrt{\left(\frac{e_{\dot{h}}}{\dot{h}}\right)^2 + \left(\frac{e_A}{A}\right)^2}. \tag{6}$$

In Eqn (6), we use the statistics of the elevation difference map over ice-free terrain to estimate the random and systematic error in $\dot{h}$. The systematic error is set to the median elevation difference, between 0.02 and 0.66 m (Table 2). We assume the systematic error to be a minimum of 0.5 m, based on the cyclic co-registration of three (or more) DEMs on the ice-free terrain. The sum of the co-registration vectors is non-zero due to the uncertainty of the co-registration method (Paul and others, 2015). We set the random error to the NMAD of elevation difference over all ice-free terrain, between 0.84 and 4.42 m (Table 2). Random error is calculated assuming an autocorrelation distance of 1 km. The random error is several orders of magnitude lower than the systematic error, as the large glacier area, 368 km^2 in 2014, ensures a sufficiently large number of independent points. The relative error of the glacier area, e_A/A, is set to 7% after considering alternative likely glacier limits, in particular for uncertain ice divides (see Fig. 3b and Discussion).

The error of the geodetic mass balance $e_{\dot{M}_g}$ is the root sum of squares of the error of the retreated mass, $e_{\dot{q}_t}$, and the mass change over the glacierized area, $e_{\dot{M}_{gla}}$. For each, error accumulates from errors in the conversion factore_ρ and the volume change rate $e_{\dot{V}}$:

$$e = |\dot{M}|\sqrt{\left(\frac{e_{\dot{V}}}{\dot{V}}\right)^2 + \left(\frac{e_\rho}{\rho}\right)^2}. \tag{7}$$

Table 2. Shift vectors removed by co-registration between the DEMs and the reference 2009 NPI DEM

	To the 2009 DEM			Between two successive DEMs, off glacier		
Date	Easting	Northing	Z	Median dh	NMAD dh	A km^2
1966 DEM	0.18	−30.44	−1.36	−0.44	2.56	107
1990 DEM	−0.03	−29.44	−1.76	−0.66	4.42	120
1996 GPS profile*	0.00	0.00	−3.69	0.00	0.89	114*
2009 DEM	Reference			–	–	–
2014 DEM	−2.49	20.54	−8.67	0.02	0.84	51

Statistics of the elevation difference map of the successive DEMs (1990−1966, 2009−1990, 1996−1990, 2014−2009). The normalized median absolute deviation (NMAD) and area are also provided. All metrics are in metres, except where stated. The 1996 GPS profile* was vertically adjusted to the 1990 DEM, using 114 overlapping points between the profile and the DEM on the glacier.

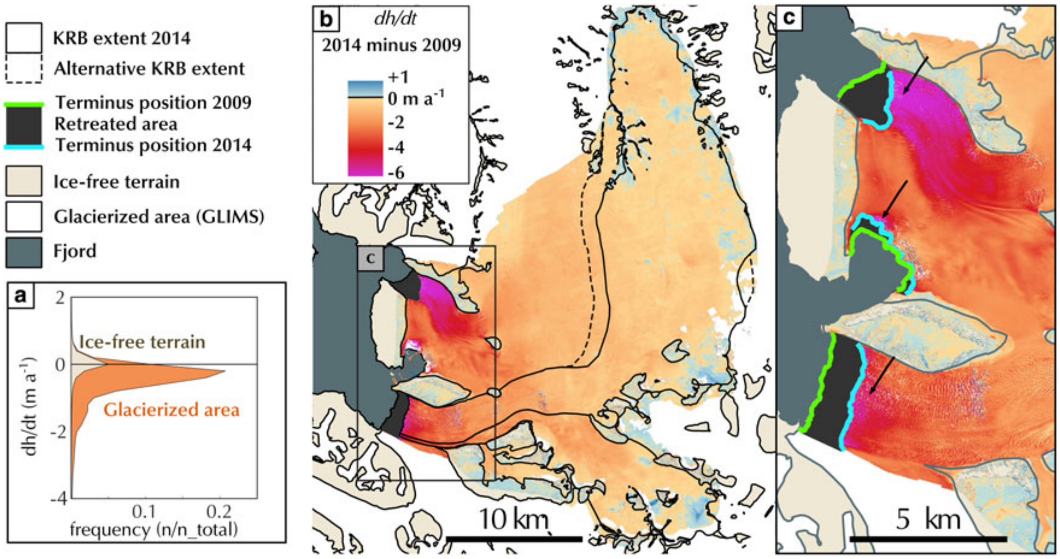

Fig. 3. Elevation difference between the 2009 and 2014 DEMs. (a) Distribution of elevation differences over ice-free terrain (filled beige) and glacierized terrain (filled orange). (b) Map of the elevation differences over the entire study area. Warm colours represent areas of elevation loss while blue colours represent the area of elevation gain. Dashed line represents the alternative mask used for sensitivity analysis. (c) Close-up of the terminus of KRB and Kongsbreen. Arrows point to zones of intense thinning.

We use the relative importance of the mass-balance equation terms and their density to determine the conversion factor uncertainty of ±100 kg m^3 (see Discussion).

4.3. Frontal ablation

Frontal ablation, $\dot{A}_\mathrm{f}$, is calculated from discharge through the terminus position at the end of a period, as the sum of ice discharge at the terminus $\dot{q}_\mathrm{fg}$, and mass loss due to terminus position change $\dot{q}_\mathrm{t}$ similarly to Schellenberger and others (2015):

$$\dot{A}_\mathrm{f} = \dot{q}_\mathrm{fg} + \dot{q}_\mathrm{t}. \tag{8}$$

We calculate a continuous time series of discharge from 2009 to 2014 at a flux gate (G in Fig. 1), ~1 km above the August 2014 terminus position using 48 velocity fields u, and glacier thickness h:

$$\dot{q}_\mathrm{fg} = \int_G h \times u \times \rho_\mathrm{ice}. \tag{9}$$

Velocity fields of the glacier tongue are produced by standard image-matching techniques (COSI-CORR, Leprince and others, 2007; Heid and Kääb, 2012) on the high-resolution optical orthoimages from FORMOSAT-2 and Pléiades. G is selected to be as close as possible to the terminus and where the velocity fields are complete. Downstream of G, image matching is not possible due to iceberg calving. We extract velocities along the flux gate, convert to perpendicular flow and apply a small correction to the cross-section area by linearly interpolating the declining glacier surface elevation between the 2009 and 2014 DEMs. We assume constant speed from the glacier surface to the bedrock because basal sliding likely dominates near the terminus (Bahr, 2015). The discharge through the flux gate G is corrected for the climatic mass balance between the flux gate and the terminus to obtain the actual discharge at the terminus. For this purpose, we apply the modelled surface mass balance of the lowest elevation bin to the surface between the flux gate and the calving front position at the end of the period. Volume loss due to the terminus position change is obtained from the digitized terminus position, the bedrock and the glacier surface elevation at the beginning of the period. Again, a correction is applied, subtracting the climatic mass-balance contribution over the retreated area.

Error in discharge results from errors in the flux gate area, surface velocities and ice density assumption. The error in the flux gate area is a combination of the error of the bedrock elevation and the glacier surface elevation. A typical error for the bedrock is ~20 m (Lindbäck and others, 2018) which dominates the error of the DEMs (~5 m). We compare it to the average thickness at the front, ~140 m, and set the flux gate area error to 15%. The weekly to monthly surface velocity estimates are compared with continuous code-based GPS records at stakes over the same time periods (Schellenberger and others, 2015). Results show a good agreement with a typical displacement difference of ~1.3 m which we conservatively assume as a systematic error leading to a 13 m a^{-1} error for the velocity (3% of the observed speed). We use the density of ice, 914 kg m^{-3}, to convert volume flux into mass flux. High-resolution DEMs of KRB terminus show crevasses with a volume that is ~2–8% of the ice column from bedrock to the surface, justifying an error of 10% for the ice density.

4.4. Climatic mass balance

Output of the climatic mass-balance model is available at a 100 m spatial and 3 h temporal resolution (Van Pelt and Kohler, 2015). The subsurface routine simulates temperature, density and water content evolution on a 50-layer vertical grid with layer depth increasing with distance to the surface. The climatic mass balance is calculated as the sum of precipitation, surface moisture exchange and runoff. Runoff either happens at the upper surface, in case of bare-ice exposure, or at the bottom of the firn/snowpack. The climatic mass balance hence accounts for mass fluxes related to refreezing and subsurface liquid water storage. Average climatic mass balance between dates of DEM collection is calculated by summing 3-hourly values. Glacier-wide climatic mass balances are calculated using a hypsometric approach (Eqn (5)) summed with the climatic mass balance over the retreated area. Additionally, model output of subsurface density profiles at dates of DEM collection are differenced to determine changes in firn column density through time.

The model error is estimated by comparing simulated values with in situ measurements at ablation/accumulation stakes. This centreline error assessment does not quantify potential errors due to spatial extrapolation to the whole glacier and the fact that the model is calibrated to the stake measurements. However, this indicates that the model does not have a systematic bias at the stake positions and that the temporal random error is ~0.25 m a^{-1} (Van Pelt and Kohler, 2015). We combine the estimate of the model error e_b with the area of the glacier error e_A to obtain the total climatic mass-balance error. The error in the model results from the random error divided by the square root of the number of years, and assumes no systematic error:

$$e_{\dot{B}} = |\dot{B}|\sqrt{\left(\frac{e_{\dot{b}}}{\dot{b}}\right)^2 + \left(\frac{e_A}{A}\right)^2}. \quad (10)$$

5. RESULTS

5.1. Closure of the 2009–2014 mass budget

For 2009–2014, we find a glacier-wide geodetic mass balance of -0.69 ± 0.12 m w.e. a^{-1} in which -0.20 ± 0.04 m w.e. a^{-1} derives from retreat of the terminus position. This estimate agrees, within the error limits, with the estimate using the mass budget method (-0.92 ± 0.16 m w.e. a^{-1}), the sum of a slightly negative climatic mass balance at -0.14 ± 0.11 m w.e. a^{-1} and a strong frontal ablation at -0.78 ± 0.11 m w.e. a^{-1} (Fig. 4). The total mass loss, including terminus position change, can be partitioned into 15 ± 12% due to climatic mass balance and 85 ± 12% to frontal ablation, the latter of which comprises 22 ± 5% from retreat of the terminus position and 63 ± 11% from the discharge at the terminus (Table 3).

The uncertainty in the geodetic mass balance includes uncertainties within the retreated area (13%) and in the glacierized area (87%). Over the 2014 glacierized area, the systematic error in the elevation difference map dominates (~62%), followed by the density conversion factor uncertainty (~18%) and the area uncertainty (~7%). We also calculated the geodetic mass balance with an alternative 2014 DEM in which the individual Pléiades DEMs were adjusted for tilts. In this case, geodetic mass balance is 6% less negative than the reference calculation (-0.65 ± 0.11 m w.e. a^{-1}). This indicates the level of sensitivity to DEM co-registration and higher order biases. Climatic mass-balance error is dominated by the temporal random error (~99%).

5.2. Estimation of an unknown mass budget component

Based on the mass-balance equation (Eqn (1)), we successively consider the total mass balance, the frontal ablation and the climatic mass balance as unknown. Each estimated value is consistent with its measured counterpart within the error bars (Fig. 4), implying that we successfully closed the

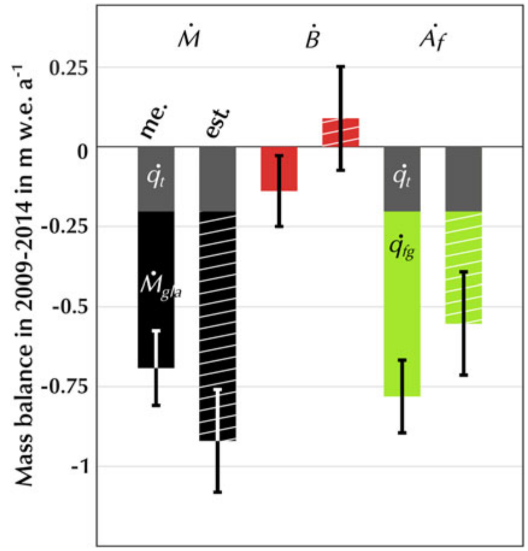

Fig. 4. Total mass balance from the geodetic method, $\dot{M}$ me., from the mass budget method $\dot{M}$ est., and its component the climatic mass balance, $\dot{B}$, and the frontal ablation, $\dot{A}_f$, for the validation period of 2009–2014 measured (flat bar) and estimated (hatched bar). The geodetic mass balance over glacierized area is in black, the climatic mass balance in red, the discharge at the terminus in green and the terminus position change contribution in grey. The mass loss by retreat of the terminus, $\dot{q}_t$, is distinguished from the mass loss by discharge through the terminus, $\dot{q}_{fg}$. The sum of the grey and green bars is the frontal ablation.

mass budget within the error limits for all variables. This validation is particularly valuable when estimating the climatic mass balance since the error of the model is harder to estimate than for observation-based components. The consistency of the estimated and measured climatic mass balance validates the model results and error estimate, but the short duration of the validation period (5 years) and the relatively small amount of refreezing within that period might limit the detection of a systematic model bias (see Discussion).

5.3. Geometry change and geodetic mass balance of KRB since 1966

KRB volume and area decreased during all three epochs, 1966–1990, 1990–2009 and 2009–2014. Glacier area variations are dominated by changes in the terminus position. Most area loss occurred during 1966–1990 and 2009–2014 with respective losses of 3.2 and 5.1 km^2, while glacier area did not change significantly between 1990 and 2009. The cumulative loss from 1966 to 2014 is 9.1 km^3, which represents ~10% of the total glacier volume in 1966 (86 ± 8 km^3) (Lindbäck and others, 2018). Thinning is observed at all elevations (Fig. 5). Below 700 m a.s.l., the elevation change rate varied strongly between epochs with more loss during 1966–1990 and 2009–2014 than 1990–2009. Above 700 m a.s.l. elevation change was -0.40 ± 0.05 m a^{-1} in 1990–2009 and $\sim -0.10 \pm 0.10$ m a^{-1} in the other periods. The elevation difference map of 2009–2014 shows the surface elevation loss pattern in the lower part of KRB (Fig. 3). Only small patches in the higher parts of INF and HOD showed elevation increase. Figure 3c shows that surface lowering is greater upstream of retreating termini

Table 3. The geodetic mass balance, climatic mass balance, discharge at the terminus and retreat mass are presented in m w.e. a^{-1}

		Geodetic mass balance m w.e. a^{-1}	Climatic mass balance m w.e. a^{-1}	Frontal ablation m w.e. a^{-1}	Retreat m w.e. a^{-1}
1966–1990	Measured	-0.40 ± 0.05	0.20 ± 0.05	–	-0.01 ± 0
	Estimated	–	–	-0.60 ± 0.07	–
1990–2009	Measured	-0.46 ± 0.07	0.02 ± 0.06	–	0.0 ± 0
	Estimated	–	–	-0.48 ± 0.09	–
2009–2014	Measured	-0.69 ± 0.12	-0.14 ± 0.11	-0.78 ± 0.11	-0.20 ± 0.04
	Estimated	-0.92 ± 0.16	0.09 ± 0.16	-0.55 ± 0.16	–

According to availability, the measured and/or the estimated value is shown.

(KRB and northern branch of KNB) than stable ones (southern branch of KNB).

The geodetic mass balance of KRB is negative for all periods and has become increasingly so through time. For example, the large decrease from -0.46 ± 0.07 m w.e. a^{-1} for the period 1990–2009 to -0.69 ± 0.12 m w.e. a^{-1} for 2009–2014 is mainly the result of terminus position retreat between 2009 and 2014 (Table 3, Fig. 6). Excluding terminus position retreat, geodetic mass balance decreased most between 1966–1990 and 1990–2009, from -0.39 ± 0.05 to -0.46 ± 0.07 m w.e. a^{-1}, and did not change significantly after. This decrease in geodetic mass balance (excluding terminus position retreat) is small and remains within the error limits.

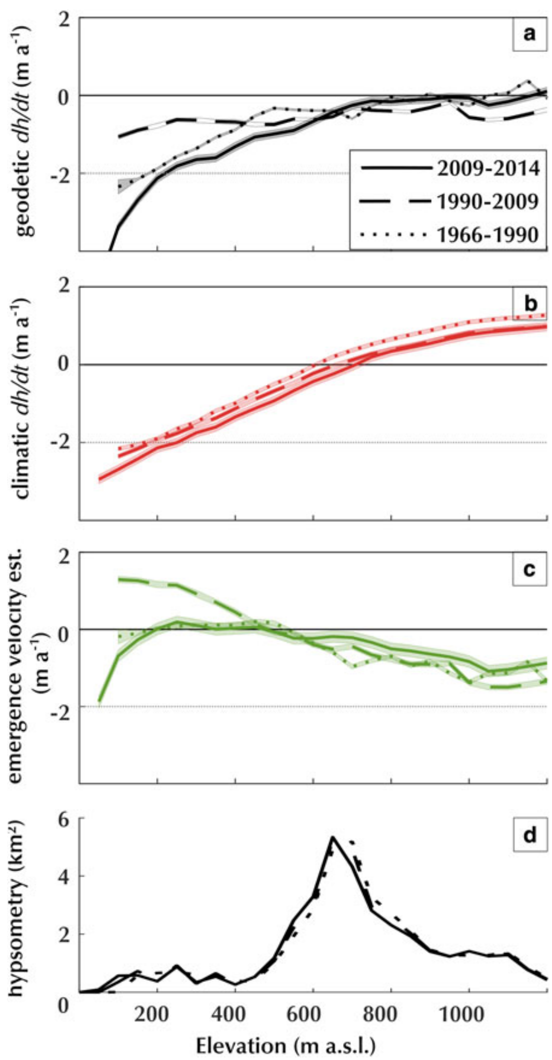

Fig. 5. Surface elevation changes, emergence velocity and hypsometry averaged in 100 m elevation bins. (a) Geodetic elevation change, (b) climatic elevation change, (c) emergence velocity deduced from the difference between (a) and (b). Line style indicates the epoch, dotted line for the 1966–1990 period, dashed line for 1990–2009 period and full line for the 2009–2014 period. Shaded area is the error. (d) Glacier hypsometry.

5.4. Climatic mass balance of KRB

Climatic mass balance decreased between every epoch from $+0.20 \pm 0.05$ m w.e. a^{-1} for 1966–1990 to -0.14 ± 0.11 m w.e. a^{-1} for 2009–2014 (Table 3, Fig. 6). Locally, climatic mass balance for 1990–2009 was similar to the 1966–1990 period in the lowest part of the glacier but indicates more mass loss and less mass gain in every bin above 400 m a.s.l. The 2009–2014 period is uniformly more negative than the 1966–1990 period over all elevation bins by ~0.25 m a^{-1} (Fig. 5). The climatic equilibrium line altitude migrated up-glacier from ~600 m a.s.l. in 1966–1990 to ~700 m a.s.l. in 2009–2014 adding ~100 km^2 to the ablation area (i.e. ~26% of the glacier total area in 1966). Consequently, the accumulation area ratio decreased from 59% in 1966–1990 to 34% in 2009–2014.

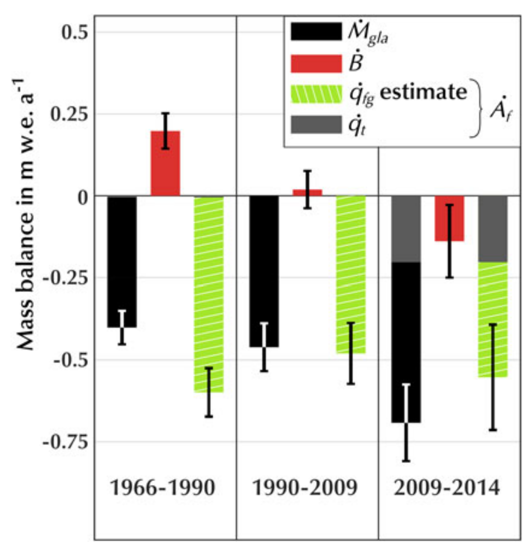

Fig. 6. Mass balance for three study periods measured with the geodetic method (black), separated between climatic mass balance (red), the estimated frontal ablation (green and grey). Grey shows the contribution of the terminus position retreat.

5.5. Frontal ablation of KRB

Frontal ablation is measured only for the 2009–2014 period and is estimated as a residual for all three periods. In 2009–2014, measured frontal ablation (-0.78 m w.e. a^{-1}) is dominated by the discharge at the terminus (-0.58 m w.e. a^{-1}) rather than retreat of the terminus position (-0.20 m w.e. a^{-1}). The rate of mass loss due to the retreat of the terminus position varies from -0.01 ± 0 m w.e. a^{-1} for 1966–1990 to -0.20 ± 0.04 m w.e. a^{-1} for 2009–2014. The terminus position remained stable between 1990 and 2009. The retreat rate from 2009 to 2014 (5 years period) is one order of magnitude higher than in 1966–1990 (24 years period), which suggests that over long-time scales, discharge at the terminus dominates the frontal ablation. Estimated discharge at the terminus decreases in absolute value between 1996–1990 and 2009–2014 (Table 3, Fig. 6), although the magnitude of the decrease lies within the error bars.

5.6. Emergence velocities

Emergence velocities are negative (dynamic thinning) above a bed step at 500 m a.s.l. (Fig. 5), which corresponds also to the area where Holtedahlfonna narrows into Kronebreen tongue (Fig. 1). The elevation at which the emergence velocity becomes zero is stable through all three periods. Below this elevation, the emergence velocity is close to zero for 1966–1990 and 2009–2014. For 2009–2014, we observe negative emergence velocity below 200 m a.s.l., that is, in the last kilometre before the terminus. The period 1990–2009 shows clear positive emergence velocity below 500 m a.s.l.

6. DISCUSSION

6.1. Sensitivity tests

6.1.1. Sensitivity to uncertain glacier boundaries

The glacier boundaries are well defined at low elevations, as the contrast in satellite imagery is strong and the glacier is confined by mountains or moraines. Higher up, the dynamic division between KRB and Isachsenfonna is more uncertain, as no surface feature is visible, nor are surface flow measurement available. Placing the divide relies then on visual interpretation of satellite images. We repeated the mass budget calculations for an alternative mask which included an additional 26 km^2 area between 500 and 1200 m a.s.l. (Fig. 3). The geodetic mass balance and climatic mass balance are modified by at most 0.01 m w.e. a^{-1}. This small sensitivity is explained by the fact that the added area is around the climatic Equilibrium Line Altitude (ELA) (Fig. 3), a region where the elevation change is moderate and, by definition, the climate mass balance close to zero.

6.1.2. Density assumptions for geodetic mass balance

One potential source of error in estimating the geodetic mass balance (Eqn (2)) concerns conversion of the total volume change to total mass change which requires assumptions on material properties and the processes involved in the mass change. Ice melting or iceberg calving leads to mass loss of material at the ice density. Snowfall in the accumulation area leads after long enough time to a volume gain with ice density according to Sorge's law (Bader, 1954). Over the short term, fresh snowfall, snow compaction and water refreezing can result in glacier volume change with densities different from ice density. The conversion factor is the average density of the volume added to and lost by the glacier. It is often taken to be at ice density or lower to account for mass change in the firn layer (Huss, 2013). The conversion factor must therefore be adapted to individual glaciers' settings and history. In Svalbard, internal refreezing of surface meltwater is common (Christianson and others, 2015; Van Pelt and Kohler, 2015) and results in conversion factor higher than ice density. Conversely, migration of the climatic ELA up-glacier exposes firn to melt, whose density is lower than ice. Using our data, we are able to compare the nature and the relative importance of the different mass-balance processes over KRB to constrain the conversion factor range.

KRB ice discharge at the terminus dominates the total mass balance during the three epochs (Table 3) with, for example, ice frontal ablation contributing to 85% of the total mass balance in 2009–2014. Therefore, during recent years, only 15% of the mass change depends on climatic mass-balance processes, whose conversion from volume to mass is most sensitive to the assumed density value. To assess the effect of variations in the conversion factor as a result of climatic mass-balance processes only, we calculate from the model runs the volume change to mass change conversion factor for the climatic mass balance for each pixel, i:

$$\rho_i = \frac{\dot{m}_{i,\mathrm{CMB}}}{\dot{h}_{i,\mathrm{CMB}}},$$

where $\dot{m}_{i,\mathrm{CMB}}$ is the modelled mass change and $\dot{h}_{i,\mathrm{CMB}}$ the modelled elevation change. Below the ELA, the conversion factor is 0.9 since only ice melt occurs here over periods longer than a couple years. Above the ELA, an interesting pattern occurs, whereby the conversion factor is larger than the density of ice. The conversion factor in the accumulation area averages 1 020 kg m^{-3} in the period 1990–2009 and 980 kg m^{-3} in the period 2009–2014 (Fig. 7). This results from internal accumulation through which firn density increases combined with independent elevation change driven by snow accumulation. We stress that this conversion factor, purely derived from the model runs is relevant for the climatic mass balance only and is not to be used directly for the volume-to-mass change conversion of the geodetic method.

6.2. Retrieving ice thickness and flux speed from the discharge

Bedrock elevation data are lacking for many tidewater glaciers. For the well-documented 2009–2014 period, we are able to estimate KRB thickness at the flux gate by using Eqns (4) and (9) and evaluate the results with the measured bedrock elevation (Lindbäck and others, 2018). During 2009–2014, the estimated flux through the flux gate is 0.13 ± 0.06 Gt a^{-1} which, using the observed gate-average speed (482 ± 10 m a^{-1}), leads to an estimated average thickness of 93 ± 40 m. This is significantly smaller than the measured ice thickness of 157 ± 17 m. This indicates that reliable measurements of the ice thickness at a flux gate close to the tidewater glacier terminus remains necessary to retrieve reliable ice discharge and thus total mass balance using the mass budget method.

Similarly, we can estimate the average speed through the flux gate using the observed flux gate area to obtain a speed of 290 ± 130 m a^{-1} which underestimates significantly the

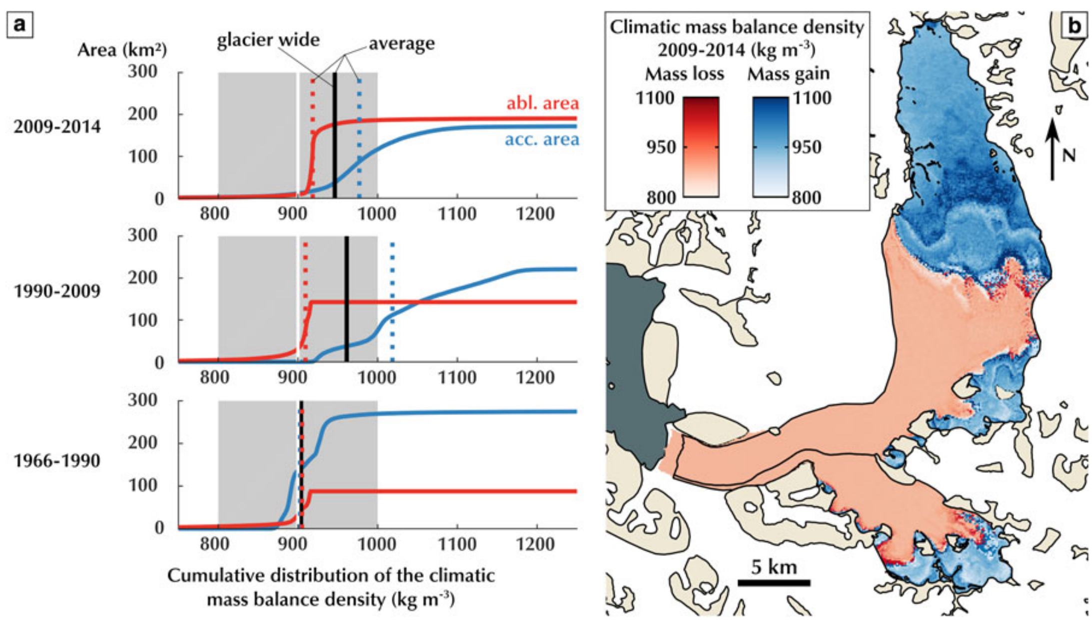

Fig. 7. Volume change to mass change conversion factor in the climatic mass-balance model. (a) Cumulative distribution of the density of the climatic mass loss (red line) and gain (blue line). Vertical line shows the average density of the climatic mass changes for the ablation area (dotted red), accumulation area (dotted blue) and the entire glacier (full black). Vertical white line shows the conversion factor used for calculation of the geodetic mass balance with error range (grey box). (b) Map of the density of the climatic mass change over KRB between 2009 and 2014. Blue shades show mass gain area, red shades show mass loss area.

measured speed of 482 ± 10 m a^{-1}. If we assume that this bias is systematic, we can still interpret the evolution of the estimated average speed through the three epochs as the flux gate area is confidently measured at each date. We observe that the decrease of the glacier thickness at the flux gate does not explain completely the reduction of the estimated flux. A decrease in speed at the terminus is necessary. This slowdown would partially explain the general retreat of the terminus observed since 1966, so far explained by melting below sea level due to the ocean warming temperature (Luckman and others, 2015) and constrained by the bed topography (Lindbäck and others, 2018). However, sporadic measurements of glacier velocity exist from July 1964 to September 1965, May to September 1986 (Lefauconnier and others, 1994) and July 1999 to July 2002 (Kääb and others, 2005) but do not show any temporal trend. Velocities average over 1999–2002 is 435 m a^{-1} at a flux gate ~500 m downstream our flux gate (Kääb and others, 2005) and is lower than our measurement for 2009–2014 (482 ± 10 m a^{-1}). Comparison is hindered by the different position of the gates and the high year-to-year variability in KRB velocity close to the front (Luckman and others, 2015; Schellenberger and others, 2015; Köhler and others, 2016). The significance of the lack of temporal trend is hard to determine as these sporadic measurements cover different time periods, especially given the very variable velocity of KRB through a year and from year to year (Köhler and others, 2016). Future work should investigate whether the LANDSAT, SPOT and ASTER archives can provide continuous measurements of frontal ablation back to 1990.

6.3. Comparison with similar studies

Our geodetic mass balances, excluding terminus position retreat, agree well with Nuth and others (2012) for 1966–1990 but differ for 1990–2007. Nuth and others (2012) estimate $\dot{M}_g = -0.68 \pm 0.09$ m a^{-1} while we found that $\dot{M}_g = -0.46 \pm 0.07$ m a^{-1} for 1990–2009. This difference in the geodetic calculation between the two studies remains unexplained. Climatic mass-balance values simulated in Nuth and others (2012) are systematically more negative by 0.20 m a^{-1} than those in this study (Van Pelt and Kohler, 2015), which would result in larger residual in the mass budget. Accounting for internal accumulation through the sensitivity test in Nuth and others (2012) or the model physics (this study) results in better mass budget closure, suggesting the validity of integrating this phenomenon in the simulation. Nuth and others (2012) evaluated the scenario of having half of the melted water stored in the firn while the model used in this study explicitly calculates internal accumulation.

Our mass balance (excluding terminus position retreat) of -0.46 ± 0.07 m w.e. a^{-1} for 1990–2009 compares well with the mass balance over the northwest region of Svalbard based on ICESat laser altimetry, measured by Moholdt and others (2010) to -0.54 ± 0.10 m a^{-1} for 2003–2009 or -0.49 ± 0.09 m w.e. a^{-1} using a conversion factor of 900 kg m^{-3}, similar to our study. Our mass balance during 1966–2009 (-0.42 ± 0.08 m w.e. a^{-1}) is also consistent with mass-balance measurement of land-terminating glaciers on the south coast of Kongsfjorden: Austre Brøggerbreen, Midtre Lovenbreen and Austre Lovenbreen, located, respectively, 17, 12 and 10 km east of KRB's terminus. James and others (2012) find a specific mass balance of -0.40 ± 0.03 m w.e. a^{-1} for Midtre Lovenbreen during 1966–2005 and -0.58 ± 0.03 m w.e. a^{-1} for Austre Brøggerbreen for 1966–2005, still using our conversion factor. Marlin and others (2017) find a specific mass balance for 1962–2013 for Austre Lovenbreen of -0.44 ± 0.06 m w.e. a^{-1}. Both studies observe an acceleration in the mass loss between the period before and after 1990 (James and others, 2012) and 1995 (Marlin and others, 2017) by ~0.20 m w.e. a^{-1} due to more negative climatic mass balance. Kohler and others (2007) report a similar acceleration in the mass loss of Midtre Lovenbreen. We observe a decrease in climatic mass balance of similar amplitude between 1966–1990 and 1990–2009 on KRB. However, we observe a different trend in the KRB geodetic mass balance, as variations in the frontal ablation add to the decrease in climatic mass balance. KRB experiences a fairly negative total mass balance compared with Austre Brøggerbreen, Midtre Lovenbreen and Austre Lovenbreen, despite its higher elevation; this can be primarily explained by the significant discharge at its front. We speculate that fluctuation in ice discharge might result from the cycle of damming and release of KRB's flow due to Kongsvegen's surge and retreat (Kääb and others, 2005).

6.4. Emergence velocities

The stability of the elevation at which the emergence velocity becomes zero, despite changes downstream of it, suggests that its position is controlled by the shape of the glacier narrowing from a large accumulation zone to a valley glacier (Fig. 5). The fact that it is systematically below the climatic equilibrium line indicates an imbalance between the dynamics of KRB and its climatic conditions. Below this elevation we observe variations in emergence velocities synchronous with the unstable periods of the terminus. There, the emergence velocity is close to zero for 1966–1990 and 2009–2014, at a time when the terminus was retreating, indicating constant flux in time in this area. Conversely, the period of terminus stability 1990–2009 shows clear positive emergence velocity below 500 m a.s.l., indicating dynamical thickening. The negative emergence velocity close to the terminus in 2009–2014 is a sign of dynamic thinning, similar to observations in Novaya Zemlya (Melkonian and others, 2016). This illustrates the propagation of perturbations initiated at the terminus of tidewater glaciers which can lead to unstable retreat and impact upstream flow (Nick and others, 2009). However, our frontal ablation estimations show no significant increase in discharge at the terminus despite the general terminus retreat trend. This suggests that the discharge is more constrained by the flux from upstream rather than the terminus position and stability.

6.5. Closing a tidewater glacier mass-balance budget

Closing a mass budget relies on the absolute value of the mass budget components and on the associated error. With sufficiently large error bars, it would always be possible to close the mass budget. We tried to calculate as carefully as possible each component and evaluate as honestly as possible their errors. However, the closing of the mass budget for KRB is relative as we close within error bars but error bars of estimated values do not overlap the measured value. This can arise from erroneous assumptions in our equations or error estimates. The error associated with the ice flux and the elevation change are validated against independent datasets or over ice-free terrain. The errors on the climatic mass balance are calculated using in situ stake measurements also used to calibrate the model. This might lead to erroneous estimation of the model error either through: (i) the lack of representativity of the stakes climatic mass balance due to spatially variable processes such as wind redistribution, or (ii) poor estimation of internal accumulation processes. These potential biases would accumulate over the studied periods. These errors are hard to detect from stake measurements, which can only indicate local mass changes above the last summer surface. Therefore, a systematic bias in the model cannot be completely disregarded as it would be hard to detect such a bias over a short 5-year period. A longer study period with similar datasets could help to confirm and quantify this possible bias.

7. SUMMARY AND CONCLUSIONS

We close the mass budget of the Kronebreen glacier system within our estimated errors for the period 2009–2014 by combining a unique dataset of satellite remote-sensing-based estimates of glacier volume changes and glacier frontal ablation with climatic mass-balance estimates from an energy-balance model constrained by in situ measurements. However, the closure of the budget is not strong as the errors of the estimated values do not overlap the measured values. Formal errors are largest for the remote-sensing-based estimates of glacier volume change and frontal ablation, rather than the mass-balance model. Retrieving the climatic mass balance from remote-sensing estimates of the geodetic mass balance and frontal ablation results in a positive value for 2009–2014, while the model suggests a negative value. The climatic mass-balance model performs well compared with KRB in situ data, but we are not yet able to rule out a potential systematic bias, for example, from small uncertainties in the parameters calibration or simply calibration from data along the centreline which does not account for accumulation or ablation transverse variability. The latter can induce small biases that accumulate through time. Nevertheless, our sensitivity test of estimating residuals in the mass budget equation from the 2009–2014 dataset allows us to justify the calculation of glacier frontal ablation or climatic mass balance as a residual during the earlier time periods (1966–2009) when observations (in situ or remote sensing) are lacking. The estimated frontal ablation is, however, too uncertain to recover the mean ice thickness or velocity at the terminus when only one of these two variables is known. The inherent errors in the various datasets do not allow us to accurately assess changes of mass balance between epochs; however, it seems likely that KRB geodetic mass balance, excluding terminus position change, remained stable between 1966 and 2014 despite increasingly negative climatic mass balance. This suggests that a decrease in frontal ablation compensated the climatic trend. Future studies with richer DEMs and more extended velocity fields may help constrain the temporality and the combination of processes which drive these phenomena.

ACKNOWLEDGEMENTS

We thank the two anonymous reviewers and Hester Jiskoot, the Scientific Editor, whose comments greatly improved this article. This work was supported by the French Space Agency (CNES), the Programme National de Télédétection Spatiale grant PNTS-2016-01, the Agence Nationale de la Recherche (ANR) Grant ANR-12-BS06-0018 (SUMER), the European Union/ERC (grant 320816) and the European Space Agency, Glaciers _CCI project (4000109873/14/I-NB).

AUTHORS CONTRIBUTION

C.N., E.B and C.D.B designed the study. E.B and C.D.B processed the Pléiades data. W.V.P produced the climatic mass-balance product and helped shape the study. C.N, J.K., E.B. and B.A. produced the flux data. B.A. produced the DEM from aerial photographs. C.D.B led the writing of the manuscript and all co-authors contributed to or commented on the manuscript.

REFERENCES

Altena B (2008) Hypsometric measurements in Holtedahlfonna in 1966 and 1990. (Report Bachelor Internship), Hogeschool Utrecht

Bader H (1954) Sorge's law of densification of snow on high polar glaciers. *J. Glaciol.*, **2**(15), 319–323

Bahr K (2015) *High resolution glacier dynamics from GNSS measurements on Holtedahlfonna, NW Svalbard*. (Master's thesis, University of Oslo)

Berthier E and 10 others (2014) Glacier topography and elevation changes derived from Pléiades sub-meter stereo images. *Cryosphere* **8**(6), 2275–2291 (doi:10.5194/tc-8-2275-2014)

Błaszczyk M, Jania JA and Hagen JO (2009) Tidewater glaciers of Svalbard: recent changes and estimates of calving fluxes. *Pol. Polar Res.*, **30**(2), 85–142

Bourgeois S, Kerhervé P, Calleja M, Many G and Morata N (2016) Glacier inputs influence organic matter composition and prokaryotic distribution in a high Arctic fjord (Kongsfjorden, Svalbard). *J. Mar. Syst.*, **164**, 112–127 (doi:10.1016/j.jmarsys.2016.08.009)

Carr JR, Stokes CR and Vieli A (2013) Recent progress in understanding marine-terminating Arctic outlet glacier response to climatic and oceanic forcing: twenty years of rapid change. *Prog. Phys. Geogr.*, **37**(4), 436–467 (doi:10.1177/0309133313483163)

Carr JR, Stokes C and Vieli A (2014) Recent retreat of major outlet glaciers on Novaya Zemlya, Russian Arctic, influenced by fjord geometry and sea-ice conditions. *J. Glaciol.*, **60**(219), 155–170 (doi:10.3189/2014JoG13J122)

Christianson K, Kohler J, Alley RB, Nuth C and Van Pelt W (2015) Dynamic perennial firn aquifer on an Arctic glacier. *Geophys. Res. Lett.*, **42**(5), 1418–1426 (doi:10.1002/2014GL062806)

Cogley JG and 9 others (2011) *Glossary of glacier mass balance and related terms*. UNESCO-IHP, Paris

Dunse T and 5 others (2015) Glacier-surge mechanisms promoted by a hydro-thermodynamic feedback to summer melt. *Cryosphere*, **9**, 197–215 (doi:10.5194/tc-9-197-2015)

Enderlin EM and 5 others (2014) An improved mass budget for the Greenland ice sheet. *Geophys. Res. Lett.*, **41**(3), 866–872 (doi:10.1002/2013GL059010)

Farinotti D and 36 others (2017) How accurate are estimates of glacier ice thickness? Results from ITMIX, the Ice Thickness Models Intercomparison eXperiment. *Cryosphere*, **11**(2), 949–970 (doi:10.5194/tc-11-949-2017)

Gardner AS and 8 others (2011) Sharply increased mass loss from glaciers and ice caps in the Canadian Arctic Archipelago. *Nature*, **473**(7347), 357–360 (doi:10.1038/nature10089)

Gardner AS and 15 others (2013) A reconciled estimate of glacier contributions to sea level rise: 2003 to 2009. *Science*, **340** (6134), 852–857 (doi:10.1126/science.1234532)

Heid T and Kääb A (2012) Evaluation of existing image matching methods for deriving glacier surface displacements globally from optical satellite imagery. *Remote Sens. Environ.*, **118**, 339–355 (doi:10.1016/j.rse.2011.11.024)

Hill EA, Carr JR and Stokes CR (2017) A review of recent changes in major marine-terminating outlet glaciers in Northern Greenland. *Front. Earth Sci.*, **4**, 1–23 (doi:10.3389/feart.2016.00111)

Höhle J and Höhle M (2009) Accuracy assessment of digital elevation models by means of robust statistical methods. *ISPRS J. Photogramm. Remote Sens.*, **64**(4), 398–406 (doi:10.1016/j.isprsjprs.2009.02.003)

Huss M (2013) Density assumptions for converting geodetic glacier volume change to mass change. *Cryosphere*, **7**(3), 877–887 (doi:10.5194/tc-7-877-2013)

Huss M and Hock R (2015) A new model for global glacier change and sea-level rise. *Front. Earth Sci.*, **3**, 1–22 (doi:10.3389/feart.2015.00054)

James TD and 5 others (2012) Observations of enhanced thinning in the upper reaches of Svalbard glaciers. *Cryosphere*, **6**(6), 1369–1381 (doi:10.5194/tc-6-1369-2012)

Kääb A, Lefauconnier B and Melvold K (2005) Flow field of Kronebreen, Svalbard, using repeated Landsat 7 and ASTER data. *Ann. Glaciol.*, **42**, 7–13 (doi:10.3189/172756405781812916)

Kohler J and 7 others (2007) Acceleration in thinning rate on western Svalbard glaciers. *Geophys. Res. Lett.*, **34**(18), 1–5 (doi:10.1029/2007GL030681)

Köhler A and 5 others (2016) A 15 year record of frontal glacier ablation rates estimated from seismic data. *Geophys. Res. Lett.*, **43** (23), 12,155–12,164 (doi:10.1002/2016GL070589)

Korona J, Berthier E, Bernard M, Rémy F and Thouvenot E (2009) SPIRIT. SPOT 5 stereoscopic survey of polar ice: reference images and topographies during the fourth international polar year (2007–2009). *ISPRS J. Photogramm. Remote Sens.*, **64**(2), 204–212 (doi:10.1016/j.isprsjprs.2008.10.005)

Lacroix P, Berthier E and Maquerhua ET (2015) Earthquake-driven acceleration of slow-moving landslides in the Colca valley, Peru, detected from Pléiades images. *Remote Sens. Environ.*, **165**, 148–158 (doi:10.1016/j.rse.2015.05.010)

Lefauconnier B (1992) Recent fluctuations of glaciers in Kongsfjorden, Spitsbergen, Svalbard (79° N). *Polar Geogr.*, **16** (3), 226–233 (doi:10.1080/10889379209377490)

Lefauconnier B, Hagen JO and Rudant J-P (1994) Flow speed and calving rate of Kongsbreen glacier, Svalbard, using SPOT images. *Polar Res.*, **13**(1), 59–65 (doi:10.1111/j.1751-8369.1994.tb00437.x)

Leprince S, Barbot S, Ayoub F and Avouac JP (2007) Automatic and precise orthorectification, coregistration, and subpixel correlation of satellite images, application to ground deformation measurements. *IEEE Trans. Geosci. Remote Sens.*, **45**(6), 1529–1558 (doi:10.1109/TGRS.2006.888937)

Lindbäck K and 8 others (2018) Subglacial topography, ice thickness, and bathymetry of Kongsfjorden, northwestern Svalbard. *Earth Syst. Sci. Data*, **10**, 1769–178119 (https://doi.org/10.5194/essd-10-1769-2018)

Luckman A and 5 others (2015) Calving rates at tidewater glaciers vary strongly with ocean temperature. *Nat. Commun.*, **6**, 8566 (doi:10.1038/ncomms9566)

Marlin C and 6 others (2017) Change in geometry of a high Arctic glacier from 1948 to 2013 (Austre Lovénbreen, Svalbard). *Geogr. Ann. Ser. A, Phys. Geogr.*, **99**(2), 115–138 (doi:10.1080/04353676.2017.1285203)

Marzeion B, Jarosch AH and Hofer M (2012) Past and future sea-level change from the surface mass balance of glaciers. *Cryosphere*, **6**, 1295–1322 (doi:10.5194/tc-6-1295-2012)

McNabb RW and Hock R (2014) Variations in Alaska tidewater glacier frontal ablation, 1985–2013. *J. Geophys. Res. Earth Surf.*, **119**(2), 153–167 (doi:10.1002/2014JF003276.Received)

Melkonian AK, Willis MJ, Pritchard ME and Stewart AJ (2016) Recent changes in glacier velocities and thinning at Novaya Zemlya. *Remote Sens. Environ.*, **174**, 244–257 (doi:10.1016/j.rse.2015.11.001)

Melvold K (1998) Evolution of a surge-type glacier in its quiescent phase: Kongsvegen, Spitsbergen, 1964–95. *J. Glaciol.*, **44**(147), 394–404

Moholdt G, Nuth C, Hagen JO and Kohler J (2010) Recent elevation changes of Svalbard glaciers derived from ICESat laser altimetry. *Remote Sens. Environ.*, **114**(11), 2756–2767 (doi:10.1016/j.rse.2010.06.008)

Nick FM, Vieli A, Howat IM and Joughin I (2009) Large-scale changes in Greenland outlet glacier dynamics triggered at the terminus. *Nat. Geosci.*, **2**(2), 110–114 (doi:10.1038/NGEO394)

Norwegian Polar Institute: Terrengmodell Svalbard (S0 Terrengmodell), (2014), Tromsø, Norway, Norwegian Polar Institute, (doi:10.21334/npolar.2014.dce53a47)

Nuth C and Kääb A (2011) Co-registration and bias corrections of satellite elevation data sets for quantifying glacier thickness change. *Cryosphere*, **5**(1), 271–290 (doi:10.5194/tc-5-271-2011)

Nuth C, Schuler TV, Kohler J, Altena B and Hagen JO (2012) Estimating the long-term calving flux of Kronebreen, Svalbard, from geodetic elevation changes and mass-balance modelling. *J. Glaciol.*, **58**(207), 119–133 (doi:10.3189/2012JoG11J036)

Nuth C and 7 others (2013) Decadal changes from a multi-temporal glacier inventory of Svalbard. *Cryosphere*, **7**(5), 1603–1621 (doi:10.5194/tc-7-1603-2013)

Osmanoğlu B, Braun M, Hock R and Navarro FJ (2013) Surface velocity and ice discharge of the ice cap on King George Island, Antarctica. *Ann. Glaciol.*, **54**(63), 111–119 (doi:10.3189/2013AoG63A517)

Paul F and 24 others (2015) The glaciers climate change initiative: methods for creating glacier area, elevation change and velocity products. *Remote Sens. Environ.*, **162**, 408–426 (doi:10.1016/j.rse.2013.07.043)

Pfeffer WT and 19 others (2014) The Randolph Glacier Inventory : a globally complete inventory of glaciers. *J. Glaciol.*, **60**(221), 537–552 (doi:10.3189/2014JoG13J176)

Rasmussen LA, Conway H, Krimmel RM and Hock R (2011) Surface mass balance, thinning and iceberg production, Columbia Glacier, Alaska, 1948–2007. *J. Glaciol.*, **57**(203), 431–440 (doi:10.3189/002214311796905532)

Raup B and 5 others (2007) The GLIMS geospatial glacier database: a new tool for studying glacier change. *Glob. Planet Change*, **56** (1–2), 101–110 (doi:10.1016/j.gloplacha.2006.07.018)

Reistad M and 5 others (2011) A high-resolution hindcast of wind and waves for the North Sea, the Norwegian Sea, and the Barents Sea. *J. Geophys. Res. Oceans*, **116**(5), 1–18 (doi:10.1029/2010JC006402)

Schellenberger T, Dunse T, Kääb A, Kohler J and Reijmer CH (2015) Surface speed and frontal ablation of Kronebreen and Kongsbreen, NW Svalbard, from SAR offset tracking. *Cryosphere*, **9**(6), 2339–2355 (doi:10.5194/tc-9-2339-2015)

Shean DE and 6 others (2016) An automated, open-source pipeline for mass production of digital elevation models (DEMs) from very-high-resolution commercial stereo satellite imagery. *ISPRS J. Photogramm. Remote Sens.*, **116**, 101–117 (doi:10.1016/j.isprsjprs.2016.03.012)

Sundfjord A and 5 others (2017) Effects of glacier runoff and wind on surface layer dynamics and Atlantic Water exchange in Kongsfjorden, Svalbard; a model study. *Estuar. Coast. Shelf Sci.*, **187**, 260–272 (doi:10.1016/j.ecss.2017.01.015)

Undén P and 26 others (2002) *HIRLAM-5 scientific documentation*. (Tech. rep.) Swedish Meteorological and Hydrological Institute, Norrkoping.

Van Pelt W and Kohler J (2015) Modelling the long-term mass balance and firn evolution of glaciers around Kongsfjorden, Svalbard. *J. Glaciol.*, **61**(228), 731–744 (doi:10.3189/2015JoG14J223)

Van Pelt W and 5 others (2012) Simulating melt, runoff and refreezing on Nordenskiöldbreen, Svalbard, using a coupled snow and energy balance model. *Cryosphere*, **6**(3), 641–659 (doi:10.5194/tc-6-641-2012)

Vaughan D and 13 others (2013) Observations: cryosphere. in *Climate Change* 2013*: The Physical Science Basis. Contribution of Working Group I to the Fifth Assessment Report of the Intergovernmental Panel on Climate Change*. Cambridge University Press, Cambridge, United Kingdom and New York, NY, USA

Willis MJ, Herried BG, Bevis MG and Bell RE (2015) Recharge of a subglacial lake by surface meltwater in northeast Greenland. *Nature*, **518**(7538), 223–227 (doi:10.1038/nature14116)

Zemp M and 16 others (2013) Reanalysing glacier mass balance measurement series. *Cryosphere*, **7**(4), 1227–1245 (doi:10.5194/tc-7-1227-2013)

MS received 5 June 2018 and accepted in revised form 19 November 2018; first published online 24 January 2019

The Cryosphere, 13, 795–814, 2019
https://doi.org/10.5194/tc-13-795-2019

The Cryosphere

Extracting recent short-term glacier velocity evolution over southern Alaska and the Yukon from a large collection of Landsat data

Bas Altena[1], **Ted Scambos**[2,3], **Mark Fahnestock**[4], **and Andreas Kääb**[1]

[1]Department of Geosciences, University of Oslo, Blindern, 0316 Oslo, Norway
[2]National Snow and Ice Data Center (NSIDC), University of Colorado, Boulder, CO 80303, USA
[3]Earth Science and Observation Center (ESOC), University of Colorado, Boulder, CO 80309, USA
[4]Geophysical Institute, University of Alaska Fairbanks, Fairbanks, AK 99775, USA

Correspondence: Bas Altena (bas.altena@geo.uio.no)

Received: 27 March 2018 – Discussion started: 9 May 2018
Revised: 31 January 2019 – Accepted: 17 February 2019 – Published: 5 March 2019

Abstract. The measurement of glacier velocity fields using repeat satellite imagery has become a standard method of cryospheric research. However, the reliable discovery of important glacier velocity variations on a large scale is still problematic because time series span different time intervals and are partly populated with erroneous velocity estimates. In this study we build upon existing glacier velocity products from the GoLIVE dataset (https://nsidc.org/data/golive, last access: 26 February 2019) and compile a multi-temporal stack of velocity data over the Saint Elias Mountains and vicinity. Each layer has a time separation of 32 days, making it possible to observe details such as within-season velocity change over an area of roughly 150 000 km^2. Our methodology is robust as it is based upon a fuzzy voting scheme applied in a discrete parameter space and thus is able to filter multiple outliers. The multi-temporal data stack is then smoothed to facilitate interpretation. This results in a spatiotemporal dataset in which one can identify short-term glacier dynamics on a regional scale. The goal is not to improve accuracy or precision but to enhance extraction of the timing and location of ice flow events such as glacier surges. Our implementation is fully automatic and the approach is independent of geographical area or satellite system used. We demonstrate this automatic method on a large glacier area in Alaska and Canada. Within the Saint Elias and Kluane mountain ranges, several surges and their propagation characteristics are identified and tracked through time, as well as more complicated dynamics in the Wrangell Mountains.

1 Introduction

Alaskan glaciers have a high mass turnover rate (Arendt, 2011) and contribute considerably to sea level rise (Arendt et al., 2013; Harig and Simons, 2016). Monitoring changes in ice flow is thus of importance, especially since the velocity of these glaciers fluctuates considerably. Many of the glaciers have been identified as surge type based on direct observations or from their looped moraines (Post, 1969; Herreid and Truffer, 2016). Furthermore, glacier elevation change in this region is heterogeneous (Muskett et al., 2003; Berthier et al., 2010; Melkonian et al., 2014), providing another indication of complicated responses. Gaining a better understanding of causes of glacier mass redistribution is necessary in order to separate surging and seasonal variation from longer-term trends.

Glacier velocity monitoring through satellite remote sensing has proven to be a useful tool to observe velocity change on a basin scale. Several studies have focused on dynamics of individual glaciers in Alaska at an annual or seasonal resolution (Fatland and Lingle, 2002; Burgess et al., 2012; Turrin et al., 2013; Abe and Furuya, 2015; Abe et al., 2016). Such studies can give a better understanding of the specific characteristics of a glacier and which circumstances are of importance for this behavior and response. Region-wide annual or "snapshot" velocities have also been estimated over the Saint Elias mountain range in previous studies (Burgess et al., 2013; Waechter et al., 2015; Van Wychen et al., 2018). The results give a first-order estimate of the kinematics at hand. With frequent satellite data coverage, one study found it is possible to detect the time of glacier speedups to within a week (Altena and Kääb, 2017b), although this study did not include an automated approach. In the most recent work, regional analyses have been conducted over sub-seasonal (Moon et al., 2014; Armstrong et al., 2017) and multi-decadal (Heid and Kääb, 2012a; Dehecq et al., 2015) periods. With such data one is able to observe the behavior of groups of glaciers that experience similar climatic settings. Consequently, surges and other glacier-dynamics events can be put into a wider spatiotemporal perspective.

Since the launch of Landsat 8 in 2013 a wealth of high-quality medium-resolution imagery has been acquired over the cryosphere on a global scale. Onboard data storage and rapid ground-system processing have made it possible to almost continuously acquire imagery. The archived data have enormous potential to advance our knowledge of glacier flow. Extraction of glacier velocity is one of the stated mission objectives of Landsat 8 (Roy et al., 2014). The high data rate far exceeds the possibilities for manual interpretation. Fortunately, automatically generated velocity products are now available (Scambos et al., 2016; Rosenau et al., 2016), though at this point sophisticated quality control and post-processing methods are still being developed.

Up to now, most studies of glacial velocity have had an emphasis on either spatial or temporal detail. When temporal detail is present, studies focus on a single glacier or a handful of glaciers (Scherler et al., 2008; Quincey et al., 2011; Paul et al., 2017). Conversely, when regional assessments are the focus, studies limited themselves to cover a single period with only annual resolution (Copland et al., 2009; Dehecq et al., 2015; Rosenau et al., 2015). Most studies rely on filtering in the post-processing of vector data by using the correlation value (Scambos et al., 1992; Kääb and Vollmer, 2000) or through median filtering within a zonal neighborhood (Skvarca, 1994; Paul et al., 2015). Some sophisticated post-processing procedures are available (Maksymiuk et al., 2016) but rely on coupling with flow models. Alternatively, geometric properties, such as reverse correlation (Scambos et al., 1992; Jeong et al., 2017) or triangle closure (Altena and Kääb, 2017a), can be taken into account during the matching to improve robustness and reduce post-processing efforts.

While glacier velocity data are increasingly available, in general post-processing is not at a sufficient level to directly exploit the full information content within these products. In this study we describe the construction of a post-processing chain that is capable of extracting temporal information from stacks of noisy velocity data. Our emphasis is on discovering temporal patterns over a mountain-range scale. Analysis of the details of glacier-dynamics patterns identified by this processing will be considered in later work. For a single glacier, it is certainly possible to employ manual selection of low-noise, good-coverage velocity datasets. However, such a strategy will not be efficient when multiple glaciers or mountain ranges are of interest. In this contribution we want to develop the methodological possibilities further and try to construct glacier velocities at a monthly resolution over large areas. Therefore, our implementation focuses on automatic post-processing, without the help of expert knowledge or human interaction. Our method retains spatial detail present in the data and does not simplify the flow structure to flow lines. This methodology can generate products that improve our knowledge about the influence and timing of tributary and neighboring ice flow variations.

We start by discussing the data used and provide background on the area under study. We then introduce the spatiotemporal structure of the data, followed by an explanation of our process for vector "voting" and vector field smoothing. The final section highlights our results and our validation and assessment of the performance of the method.

2 Data and study region

2.1 GoLIVE velocity fields

The Global Land Ice Velocity Extraction from Landsat 8 (GoLIVE) velocity fields used in this study are based upon repeat optical remote-sensing imagery and are distributed through the National Snow and Ice Data Center (NSIDC; https://nsidc.org/data/golive, last access: 26 February 2019) (Scambos et al., 2016). These velocity fields are derived from finding displacements between pairs of Landsat 8 images, using the panchromatic band with 15 m resolution. A high-pass filter of 1 km spatial scale is applied before processing. Normalized cross-correlation is applied between the image pairs on a sampling grid with 300 m spacing (Fahnestock et al., 2016; Scambos et al., 1992) and a template size of 20 pixels (or 300 m). The resulting products are grids with lateral displacements, the absolute correlation value, signal-to-noise ratio and ratio between the two best matches. At the time of writing, displacement products can cover a time interval from 16 days up to 96 days. For a detailed description of the processing chain see Fahnestock et al. (2016).

The Landsat 8 satellite has a same-orbit revisit time of 16 days and a swath width of 185 km. Only scenes which are at least 50 % cloud-free are used (as determined by the provided estimate in the metadata for the scenes). Consequently, not every theoretical pair combination is processed, and no pairs of overlapping images with different orbits (paths) are used (see Altena and Kääb, 2017a) to avoid more complicated viewing geometry adjustments. Georeference errors are compensated for by the estimation of a polynomial bias surface through areas outside glaciers (i.e., assumed stable). The glacier mask used for that purpose is from the Randolph Glacier Inventory (RGI) (Pfeffer et al., 2014). The resulting grids come in Universal Transverse Mercator (UTM) projection and if orthorectification errors are minimal, displacements for precise georeferencing require only horizon-

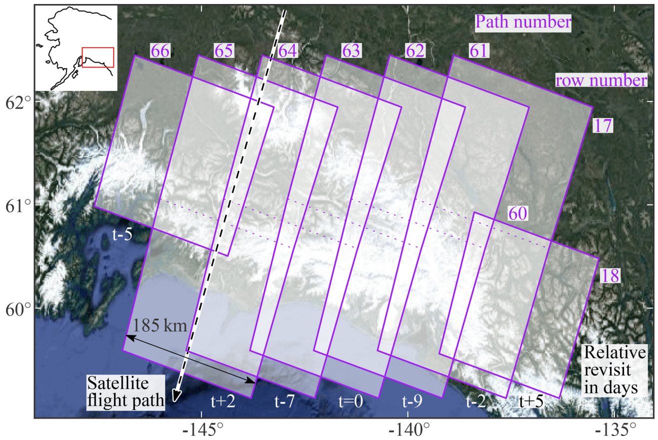

Figure 1. Nominal Landsat 8 footprints used over the study region. The purple text annotates the different satellite paths of Landsat, while the white text indicates the relative overpass time in days with respect to path 63.

tal movement of a few meters (generally < 10 m). In total we use 12 Landsat path–row tiles to cover our study area (Fig. 1).

2.2 Study region

The region of interest covers the Saint Elias, Wrangell and Kluane mountain ranges, as well as some parts of the Chugach range. Many surge-type glaciers are located in the Saint Elias Mountains (Post, 1969; Meier and Post, 1969). These ranges host roughly 42 000 km^2 of glacier area with roughly 22 % of the glacier area connected to marine-terminating fronts draining into the Gulf of Alaska (Molnia, 2008). The glaciers in this area are diverse, as a wide range of thermal conditions (cold and warm ice) and morphological glacier types (valley, ice fields, marine terminating) occur in these mountain ranges (Clarke and Holdsworth, 2002). This diversity is in part due to the large precipitation gradient over the mountain range. The highest amount of precipitation falls in summer or autumn. The study area covers mountain ranges with two distinct climates. Along the coast one finds a maritime climate with a small annual temperature range. These mountains function as a barrier, and the mountain ranges behind, in the interior, have a more continental climate (Bieniek et al., 2012).

3 Methodology

GoLIVE and other similar velocity products are derived from at least two satellite acquisitions. When images from multiple time instances are used, combinations of displacements, with different (overlapping) time intervals, can be constructed. In order to be of use for time series analysis, detailed velocity fields with different time spans need to be combined into a dataset with regular time steps. To reduce the noise, the temporal configuration of overlapping products can be used to synthesize am improved multi-temporal velocity field.

3.1 Temporal network configuration

At the latitude of southern Alaska, scenes from adjacent tracks have an overlap of 60 %. Looking at one track only (or Landsat path), the 16-day revisit makes several matching combinations of integer multitudes of 16 days possible. For example, suppose that over a 64-day period (Δt), five images are acquired from one satellite track and their potential pairing combinations can be illustrated as a network (Fig. 2). In this network, every acquisition (at time t) is a node, and these nodes are connected through an edge that represents a matched pair leading to a collection of displacements (d) with associated similarity measures (ρ).

When velocities over different time spans are estimated, this network has in theory a great amount of redundancy. However in practice this is complicated, as combinations of images are not processed when there is too much obstruction by clouds. Furthermore, individual displacements can have gross errors, as an image match was not established due to surface change or lack of contrast and thus loss of similarity. Consequently, when data from such a network are combined to synthesize one consistent velocity time series, the estimation procedure needs to be able to resist multiple outliers or be able to identify whether displacement estimates could be extracted at a reliable level at all.

The network shown in Fig. 2 can be seen as a graph; nodes correspond to time stamps and edges to matched image pairs. Such a graph can be transformed into an adjacency matrix ($\mathbf{A}_\mathrm{G}$, see Fig. 2). In this matrix the columns and rows represent different time stamps. The edges can be directed, indicating which acquisition is the master (reference) or the slave (search) image during the matching procedure. For the GoLIVE data, the oldest acquisition is always the reference image; hence within the matrix only the upper triangular part has filled entities. The spacing of the time steps is 16 days and the number of days is set into the corresponding entries when a time step is covered by an edge. Individual days are specified so that adjacency matrices from different tracks which have different acquisition dates can be merged. If partial overlap of an edge occurs, then the time steps are proportionally distributed. For example, for a small network of three nodes, velocity (v) can be estimated through least-squares adjustment of the displacements (d) through the following systems of equations (Altena and Kääb, 2017a):

$$\boldsymbol{y} = \mathbf{A}\boldsymbol{v}, \text{ where } \quad \boldsymbol{y} = \begin{bmatrix} d_{12} \; d_{23} \\ d_{13} \end{bmatrix}, \quad \mathbf{A} = \begin{bmatrix} \Delta t_{12} & 0 \\ 0 & \Delta t_{23} \\ \Delta t_{12} & \Delta t_{23} \end{bmatrix}, \quad \boldsymbol{v} = \begin{bmatrix} v_{12} \\ v_{23} \end{bmatrix}. \tag{1}$$

Here the subscript denotes the time span given by the starting and ending time stamps of the interval. This relational

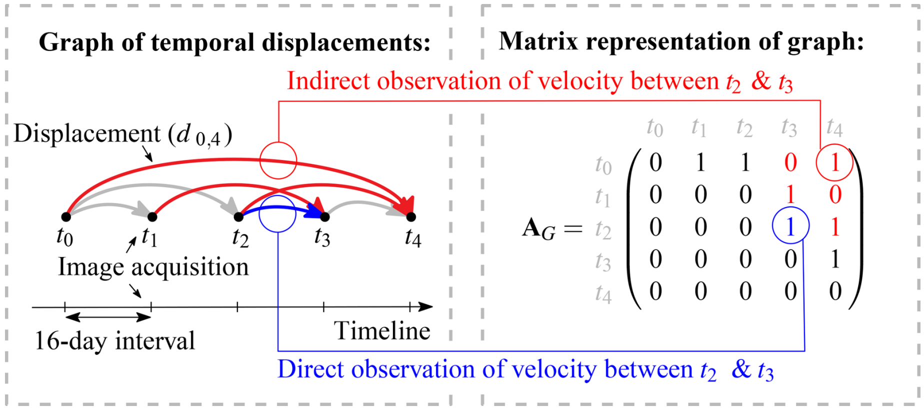

Figure 2. Graphical and matrix representation of a network. Here acquisition pairs within a network are illustrated and written down in an adjacency matrix ($\mathbf{A}_\mathrm{G}$). The dark gray squares indicate acquisitions within a period to be estimated. The connecting colors symbolize an open (red) or closed (blue) selection of displacements to be used for the velocity estimation over this period ($\boldsymbol{v}$).

structure of displacements is similar to a leveling network. When the adjacency matrix is converted to an incidence matrix, then this matrix is the design matrix (**A**) (Strang and Borre, 1997). This makes the generation of such network adjustments easily implemented.

This formulation of the temporal network makes it possible to estimate the unknown parameters, i.e., the temporal components of the velocity time series, through different formulations. This is illustrated in Fig. 2, in which a velocity (between t_2 and t_3) is estimated. Displacements that fall between the two images can be used for the estimation (here blue), which we here call a “closed” network. But as can be seen in the figure as red connections, other displacements from outside the time span are overarching and stretching further than the initial time interval. Such measurements can be of interest as they can fill in gaps or add redundancy, but the glacier flow record obtained will be aliased compared to the real motion. Consequently, we call such a network configuration an “open” network (here red).

3.2 Voting

The velocity dataset we use (like any) contains a large number of incorrect or noisy displacements. Typically, the distribution of displacements has a normal distribution but with long tails. Moreover, a least-squares adjustment is very sensitive to outliers contained in the data to be fitted. Therefore, direct least-squares computation of velocity through the above network is not easily possible and some selection procedure is needed to exclude gross errors. Outlier detection within a network such as in Eq. (1) can be performed through statistical testing (Baarda, 1968; Teunissen, 2000), assuming measurements (d) are normally distributed. However, such procedures are less effective when several gross errors are present within the set of observations. Extracting information from highly contaminated data is therefore an active field of research. For example, robust estimators change the normal distribution to a heavy-tailed distribution. Nevertheless, such estimations typically still start with a normal least-squares adjustment based on the full initial set of observations, and only in the next step are the weights iteratively adjusted according to the amount of misfit. Hence, such methods are still restricted to robust a priori knowledge or a dataset with relatively small amounts of contamination by gross errors.

Another common approach to cope with the adjustment of error-rich observations is through sampling strategies such as least median of squares (Rousseeuw and Leroy, 2005), or random sampling and consensus (RANSAC) (Fischler and Bolles, 1981). A minimum number of observations are picked randomly to solve the model. The estimated parameters are then used to assess how the initial model fits with respect to all observations. Then the procedure is repeated with a new set of observations. The sampling procedure is stopped when a solution is within predefined bounds, or executed a defined number of times after which the best set is taken. Such methods are very popular as they can handle high contamination of data (up to 50 %) and still result in a correct estimate. Put differently, the breakdown point is 0.5 (Rousseeuw and Leroy, 2005). However, we use a different approach as these methods implement polynomial models. Our dataset benefits from including conditional equations as well.

The equations that form the model can be seen as individual samples that populate the parameter space. In such a way the individual relations within the equation propagate into points, lines or surfaces depending on their dimensions and relation given by the equation. Hence, measurements can be transformed into a shape that is situated within the parameter space (which has a finite extent and resolution). The collection of shapes will be scattered throughout this parameter space, but such shapes converge at a common point, which is most likely the correct parameter values. This transforma-

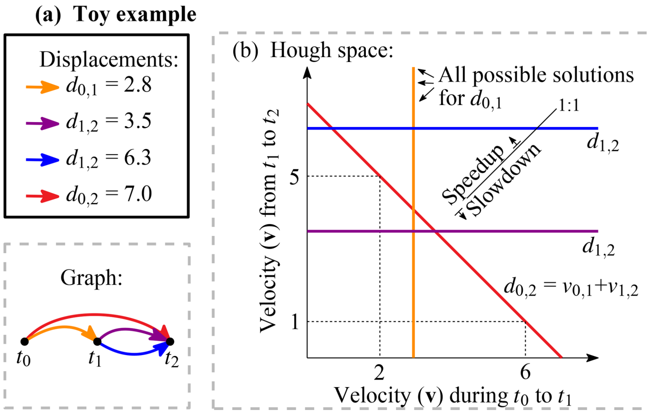

Figure 3. On the left is a graphical representation of Landsat 8 acquisitions at different times (t) illustrated as nodes and matching solutions with displacements ($\boldsymbol{d}$) are shown as edges, within a network. The subscript for the displacement denotes the time interval. The velocities ($\boldsymbol{v}$) are estimated through the collection of all these displacements. On the right the mathematical representation or its parameter (Hough) space for voting of displacements over two time instances is shown; in this case the parameter space of only $\boldsymbol{v}_{0,1}$ and $\boldsymbol{v}_{1,2}$ are shown.

tion is the Hough transform and is commonly used in image processing for the detection of lines and circles.

However, the Hough transform is discrete while the measurements are noisy; thus the shapes should also be fuzzy. In this study we follow this latter direction and after discretizing the displacement-matching search space, we exploit a voting strategy. Because the shapes in parameter space are blurred, a fuzzy Hough transform (Han et al., 1994) is implemented. Our matching search space is simply the linear system of equations of the network described above. To illustrate the system, an example of a network with four displacements ($\boldsymbol{d}$) is shown in Fig. 3. These displacements can be placed within a discrete grid that spans a large part of the parameter space (in this example two dimensional). For the short time span displacements, this results in vertical or horizontal lines (blue, purple and orange). The lines originate from the ambiguity, which is also in the entries of the design matrix ($\mathbf{A}$) as 0 entries. For the overarching displacement (in red) the displacement is a combination of both velocities. Only the total displacement is known; thus the line results in a diagonal orientation ($5+2$ can be a solution as well as $1+6$, or a non-integer combination).

In this toy example, the lines concentrate around 3 for both velocities, but with a slight preference to the upper left. This location indicates a slight speedup between these two time spans. For this case, the blue line is an outlier; it does not contribute to crossings in this zone and instead creates single crossings with other correct displacements at other locations within the parameter space. Apart from the blue line, the other crossings are concentrated around a zone but do not perfectly intersect at a single point. This is due to noise present in every displacement measurement. To simulate this noise, the lines are perturbed with a Gaussian function, as for the toy example shown in Fig. 4a. In this case, every observation will fill the parameter space with a discretized weighting function. This fuzziness in the Hough space makes it possible to find the intersection while noise is present. The dimension of the Hough space depends on the formulation of the network. In principle it can have any dimension; in one dimension this is a simple histogram, but in higher dimensions this will translate into a line which radially decreases in weight. For this study we implement a three-dimensional Hough space, which for our toy example will look like Fig. 4b; though due to visualization limitations, the fuzzy borders are not included.

The advantage of a Hough search space is the resistance to multiple outliers. It builds support and is not reliant on the whole group of observations. When a second or third dimensional space is used, the chances of random (line) crossing decrease significantly in the parameter space, and such events will stand out when multiple measurements do align. Random measurement errors can be incorporated through introducing a distribution function. In our implementation this is a Gaussian distribution, but other functions are possible as well. The disadvantage of the fuzzy Hough transform is its limitation in implementing a large and detailed search space, as the dimension and resolution depend on the available computing resources.

The fuzzy Hough transform functions as a selection process to find observations which are to a certain extent in agreement. With this selection of inliers the velocity can finally be estimated through ordinary least-squares estimation. The model is the same as used to construct the network. However, the observations without consensus (i.e., outliers) are not used. The remaining observations can, nevertheless, still be misfits, such as from shadow casting, as no ice flow behavior is prescribed in the design matrix of Eq. (1).

3.3 Smoothing

Because the voting and least-squares adjustment in our implementation has no neighborhood constraints but is rather strictly per matching grid point, the velocity estimates contain systematic, gross and random errors, though reduced with respect to the initial dataset. This least-squares adjustment with voted displacements results in a spatiotemporal stack of velocity estimates that have a regular temporal spacing. However, due to undersampling as a result of cloud cover or lack of consensus among the displacement acquisitions, the stack might have holes or ill-constrained estimates. We apply a spatial–temporal smoothing taking both spatial and temporal information into account using the Whitacker approach that tries to minimize the following function (S),

$$S = \sum_i w_i (\hat{x}_i - x_i)^2 + \lambda \sum_i (\Delta^2 x_i)^2. \tag{2}$$

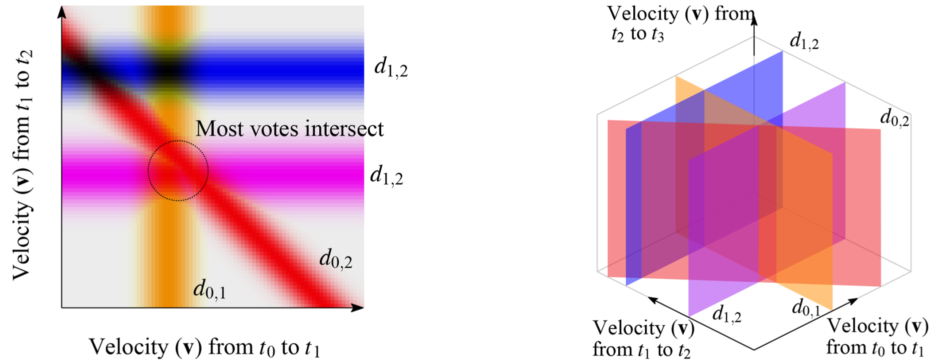

(a) Two-dimensional fuzzy Hough space

(b) Three-dimensional Hough space

Figure 4. Two modifications used in this study, which deviate from the standard Hough transform as given by the toy example in Fig. 3. **(a)** The change from a clear ideal line towards fuzzy weights. **(b)** The extension towards a higher dimension, in this case the lines transform to planes that intersect with each other.

This formulation is the one-dimensional case, in which for every location (x, where i denotes the index of the grid) an estimate (denoted by $\hat{\cdot}$) is searched for that minimizes S. Here Δ denotes the difference operator; thus $\Delta x_i = x_{i+1} - x_i$. Similarly, Δ^2 is the double difference, describing the curvature of a signal ($\Delta^2 x_i = x_{+1} - 2x_i + x_{i-1}$). For the implementation of this method we use the procedure presented by Garcia (2010). This routine has an automatic procedure to estimate the smoothing parameter (λ) and has robust adaptive weighting (w). Its implementation uses a discrete cosine transform (DCT), which eases the computational load. The discrete cosine transform operates both globally and locally, and in multiple dimensions. In order to include all data at once, the vector field is configured as a complex number field.

The smoothing parameter (λ) operates over both space (two dimensions) and time (one dimension), but the smoothing parameter is a single scalar. In this form it would be dependent on the choice of grid resolutions in time and space. In order to remove this dependency and fulfill the isotropy property, the spatial and temporal dimensions are scaled. For this scaling estimation we construct an experimental variogram and look at its distribution (Wackernagel, 2013). A subsample of the dataset with least-squares velocity estimates is taken for this purpose, which is situated over the main trunk and tributaries of Hubbard Glacier. Along the spatial axis, the variogram in Fig. 5a shows spatial correlation up to about 10 km. This sampling interval is then used to look at the spatiotemporal dependencies, as illustrated in Fig. 5b. At around a year in temporal distance one can see a clear correlation which corresponds to the seasonal cycle of glacier velocity. From this variogram a rough scaling was estimated, and the anisotropy was set towards a factor of 4. In our case the pixel spacing is 300 m and the time separation is 32 days.

4 Results

4.1 Method performance

Two different temporal networks (combinations of time intervals) can be formulated in order to calculate a velocity estimate, as is described in Sect. 3.1. The open configuration includes a greater number of velocity estimates from image pairs, but this has consequences. It results in a more complete dataset, with coherent velocity fields, but when short-term glacier dynamics occur, temporal resolution of the event may be aliased.

Our methodology thrives when several displacement estimates are present; otherwise testing is not possible. This prerequisite is especially apparent when a closed configuration is used; then the collection of displacements are reduced. In order to show this dependency a slice is shown in Fig. 6. In this time interval the western side has several overlapping displacement estimates in space and time, while this is limited at the eastern side. The exact distribution of the available data for this time interval is also highlighted in Fig. A1, within Appendix A. The lack of data can be seen at the western border of both estimates. On the eastern side the glacier velocity structure is more clearly visible, especially in the open configuration.

In Fig. 7 more details of the two different configurations are shown. By including more imagery as with an open configuration, the velocity estimates are more complete, as can be seen along the outlets of Guyot Glacier. In the same subsection, the completeness increases and so does the consistency, which is most apparent in the coherent low velocities over stable ground. With more displacement vectors in the configuration, smaller-scale details, such as tributaries flowing into the large Kaskawulsh Glacier, become more evident.

The spatiotemporal least-squares estimates still have, to some extent, variation in direction and amplitude as well as outliers. Therefore spatial–temporal smoothing is applied, in

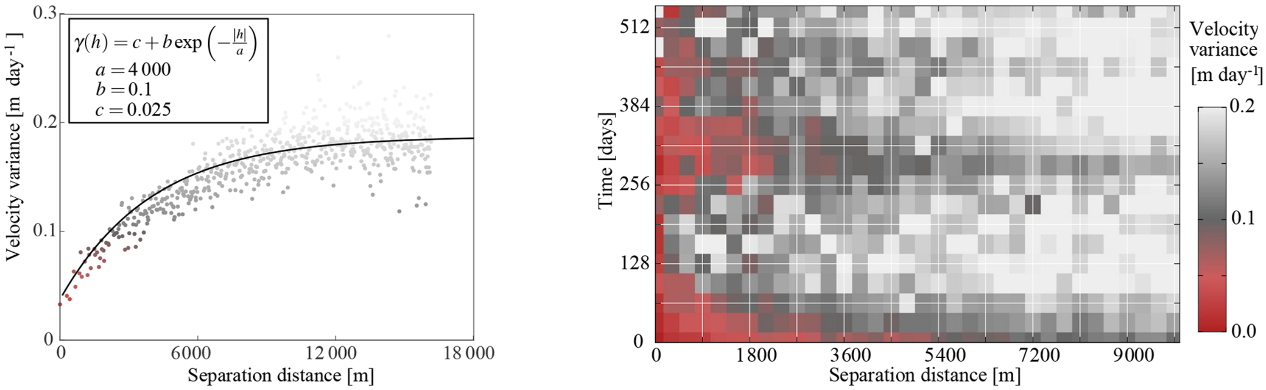

(a) Experimental variogram in the spatial domain

(b) Spatiotemporal experimental variogram

Figure 5. Experimental variograms over a slice of the stack and over a subset of the spatiotemporal stack. The color bar along the axis of **(a)** is used for the coloring of **(b)**. The aspect ratio of panel **(b)** is at the resolution of the produced data cube (32 days by 300 m). In order to make this isotropic, the vertical axis needs to enlarge, so the spread in variance is similar in any direction (isotropic).

order to extract a better overview from the data, as is described in Sect. 3.3. The results of this smoothing for the same time interval as in Fig. 6 are shown in Fig. 7.

In the smoothing procedure the surroundings of glaciers, which are stable or slow-moving terrain, are included. Consequently, high speedups such as on the surge bulge on the Steele Glacier are dampened, as in this case it has a confined snout within a valley. They do not disappear, as the signal is strong and persistent over time, but damping does occur. An aspect of concern is the retreat of the high-velocity termini of many outlet glaciers; their fronts with large velocities seem to retreat in the smoothed version, while this is not the case for the original least-squares estimate (see example in Appendix B). This effect is caused by surrounding zero-valued water bodies. Damping also occurs at turns such as at Hubbard Glacier, where the mask reduces the effect of stable terrain but has no specific glacial properties. The isotropy function included in the smoother might work for a local neighborhood but breaks down for fast-moving outlets. For this smoother, weights are given in relation to a neighborhood. However for glacier flow, the magnitude might be more similar in the direction of flow lines, while in the cross-flow direction the flow orientation might be more similar. This relation is not included in the smoother, causing damping of the gradients. There is a trade-off between the damping effect of the smoothing and the advantage of having a clear image over large areas.

Because the surrounding terrain, which has no movement, impacts the smoothed glacier velocity estimates, in particular for surge and calving fronts (i.e., for strong spatial velocity gradients), the smoothing can be supported by a glacier mask. In our case, this mask is a rasterization of the Randolph Glacier Inventory (Pfeffer et al., 2014), with an additional dilation operation, to take potential advance or errors in the inventory into account. The difference in result using this masking procedure is shown in Fig. 7, with some highlights. In general, the mask does compensate a little bit for the damping, but because the regions are mostly covered with ice its effect is small.

4.2 Validation over stable terrain

A first component for validation is an analysis of the stable ground and the effect of the smoothing of the voted estimates. The non-glaciated terrain is taken from a mask. A similar mask, also based on the Randolph Glacier Inventory, is used within the GoLIVE pipeline. Here, displacements over land and non-glaciated terrain are used to co-align the imagery (Fahnestock et al., 2016), as geo-location errors might be present in the individual Landsat images. The fitting is performed through a polynomial fit; in general these offsets should be random with a zero mean.

The distribution of these stable terrain measurements, more than 65 million in total, are illustrated in Fig. 8. Similar to the visual inspection already illustrated in Fig. 6b, the distributions also show a clear improvement, even though the voted estimates still seem to be noisy with significant outliers.

4.3 Validation of post-processing procedures

The voting used in our procedure is assessed through validation with an independent velocity estimate. Terrestrial measurements are limited in the study area; hence we use satellite imagery from RapidEye satellites over a similar time span. Data from this constellation have a resolution of 5 m and through processing in a pyramid fashion, a detailed flow field can be extracted. This velocity field functions as a baseline dataset to compare the GoLIVE and the synthesized data. Here we will look at a section of Klutlan Glacier, which flows from west to east and is thus aligned with one map axis. The velocity of this glacier is, due to its surge, of significant mag-

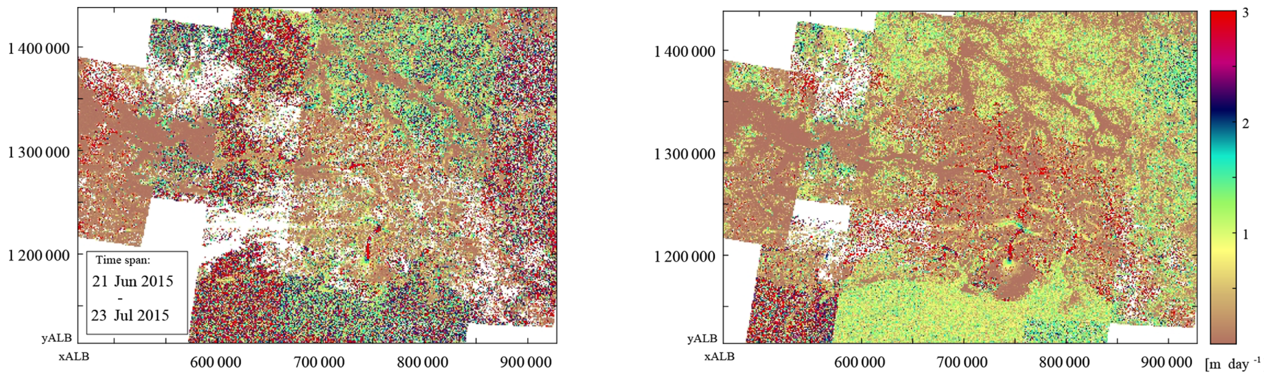

(a) Closed network selection (b) Open network selection

Figure 6. Least-squares estimates of velocities for the region shown in Fig. 1 with different network configurations. See Fig. 3 for a toy example of the terminology. The study region is spread over several UTM zones; hence the dataset is in Albers equal-area projection (ALB) with North American Datum 83. White regions correspond to data without an estimate.

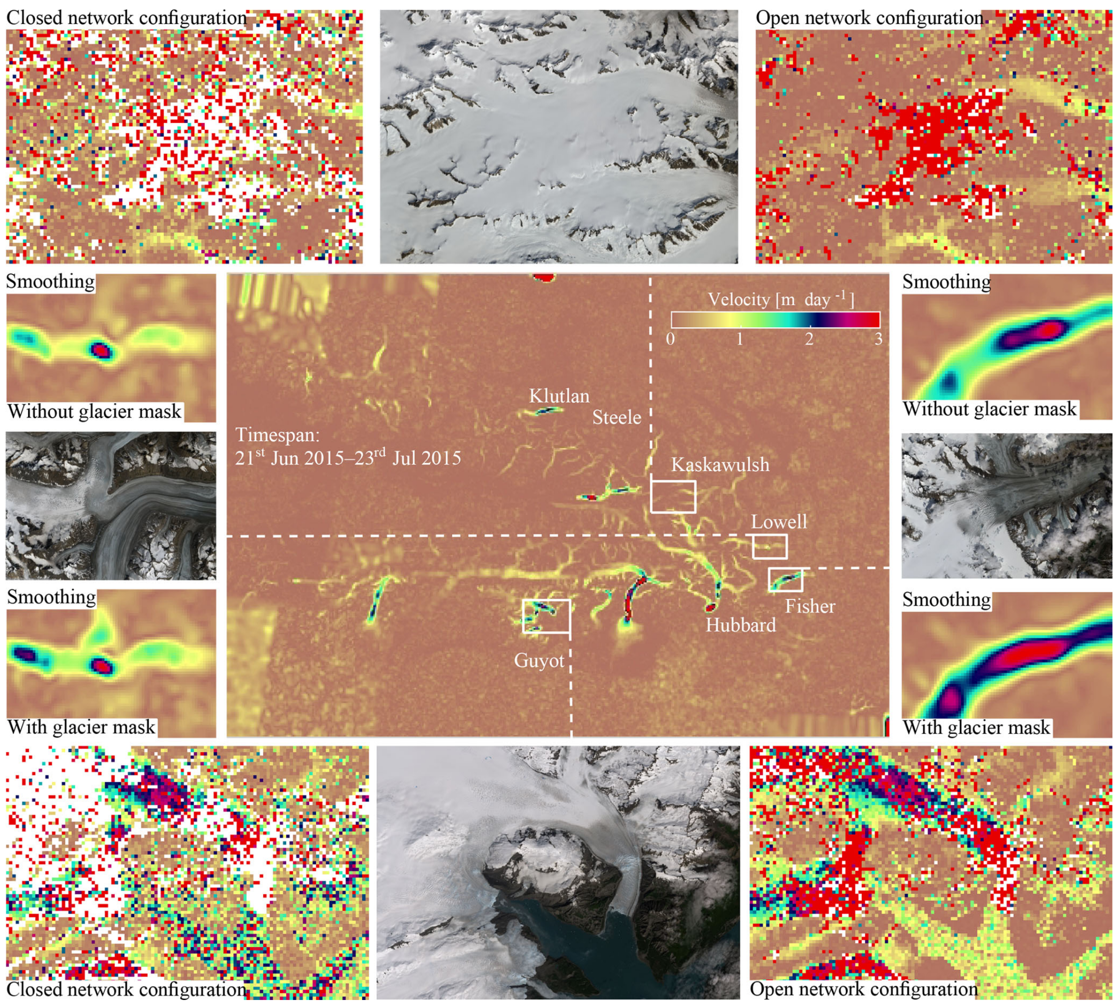

Figure 7. Overview map of different sections for the time interval, which is similar to Fig. 6 (i.e., 21 June till 23 July 2015). The surrounding zoom-ins are from the same time period but with different configurations (open vs. closed) or smoothing settings (glacier mask vs. no mask).

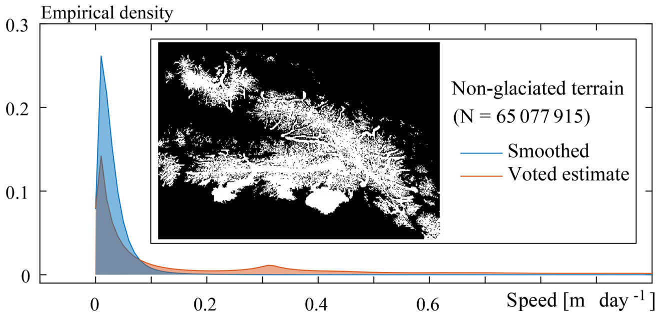

Figure 8. Distribution of the speed over stable terrain, for displacements extracted from the voting process, or after spatial temporal smoothing. The mask used is within the inset.

nitude and therefore will have a wide spread in the voting space.

The two RapidEye images used over Klutlan Glacier were taken on 7 September and on 7 October 2016. To retrieve the most complete displacement field of the glacier, we used a coarse-to-fine image matching scheme. The search window decreased stepwise (Kolaas, 2016) and the matching itself was carried out through orientation correlation (Heid and Kääb, 2012a). At every step a local post-processing step (Westerweel and Scarano, 2005) was implemented to filter outliers. The resulting displacement field over one axis (that is x, the general direction of flow) for this period is illustrated in Fig. 9a.

For the voting of the Landsat 8-based GoLIVE data, an overlapping time period was chosen, from 11 September up to 13 October 2016, nearly but not exactly overlapping with the RapidEye pair. An open configuration was used, meaning all GoLIVE displacement fields covering this time period were used, resulting in a total of 36 velocity fields involved in the voting. The voted estimates and scores are illustrated in Fig. 9c and e. Voting scores are high over the stable terrain but low over the glacier trunk. To some extent this can be attributed to the surge event. The median over the stack and the median of absolute differences (MAD) are shown in two panels on the right side of Fig. 9d and e. These two measures are frequently used to analyze multi-temporal datasets (Dehecq et al., 2015).

When looking at this time period for the GoLIVE data, a clear displacement field is shown, as both images (11 September, 13 October) from Landsat 8 were cloud-free. The pattern is in close agreement with the RapidEye version. When looking at the voted estimate a similar pattern is observable but more corrupted. In some respects the median estimate captures the direction of flow but overestimates the velocity, probably due to the surge that occurs. The spread might confirm this, as shown by the MAD, as this is considerable and will not help to justify which displacement is correct. Furthermore, the voted estimate is an estimate over a short interval, while the median estimate is calculated over the full stack.

To better assess these results, the distribution of both two-dimensional displacement fields is illustrated in Fig. 10a and b. Two groups of displacement regimes are clearly visible, a cluster showing little movement and a group of displacements with a dominant movement eastwards. The voted distribution has more spread, and outliers are present, but in general the mapping has the correct direction and magnitude. When the x-component of these displacements is compared against the RapidEye displacements, the median of this difference is $0.45\,\mathrm{m\,day^{-1}}$ for the voting and $0.27\,\mathrm{m\,day^{-1}}$ for the good GoLIVE pair. A similar trend can be seen in Fig. 10c, which again shows the distributions are similar. The illustrated validations do show the voting scheme is able to capture the general trend of the short-term glacier flow through a large stack of corrupted velocity fields. While the voted estimate is worse than the clean GoLIVE estimate, we stress that the chosen GoLIVE dataset is one clean example within a large collection of partly corrupted displacement fields. Hence it is a step towards efficient information extraction, though the implemented voting has many potential areas for improvement.

4.4 Glaciological observations

When looking at the spatiotemporal dataset some patterns that have been observed by others also appear in our dataset. For example, the full extent of Bering Glacier slows down, as highlighted by Burgess et al. (2012); however our time series covers a period when the full deceleration towards a quiescent state can be seen. This observation of a slowdown can also be made for Donjek Glacier (Abe et al., 2016) and Logan Glacier (Abe and Furuya, 2015); see supplementary video. In the time period covered by our study some surges appear to be initiated. For example, our dataset captures a surge traveling along the main trunk of Klutlan Glacier (see Figs. B1 and B2 in the Appendix B).

For the surge of Klutlan Glacier, the dataset shows the evolution of its dynamics, as can be seen by some velocity time stamps in Fig. 11. The surge initiation seems to happen in the central trunk of the glacier, and the surge front progresses downwards from there (with steady bulk velocities of around $4\,\mathrm{m\,day^{-1}}$). The surge also propagates upwards mainly into the westernmost basin. The eastern basin does increase in speed but to a lesser extent, while the middle basin of this glacier system does not seem to be affected significantly. The up-glacier velocity increase is limited and does not reach the headwalls of any basin. In Landsat imagery of late 2017, there is no indication of any heavily crevassed terrain in the upper parts of these basins, which supports the hypothesis of a partially developed surge.

When looking at the velocities over the flow line of the Klutlan Glacier, as in Fig. 12a, both the extension downstream as well as the upstream progression of the surge can

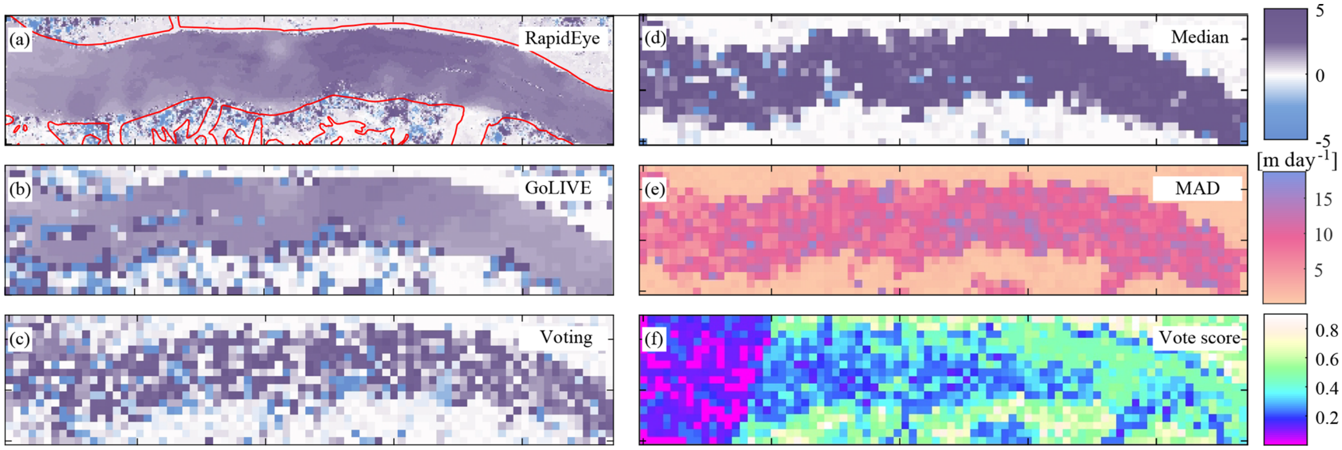

Figure 9. Monthly displacement in the x direction over the Klutlan Glacier (for location see Fig. 7) using several data sources and velocity assessment schemes. Panel **(a)** shows velocities derived from two RapidEye images. Glacier borders are outlined in red. Panel **(b)** shows displacement estimates from a GoLIVE dataset (input) and the resulting voted estimate **(c)** of a combination of 36 GoLIVE datasets (output). The corresponding voting score of these estimates is shown in **(f)**. Panels **(d)** and **(e)** show the median and the median of absolute deviation (MAD), respectively, over the full dataset. These last two results would typically be used for data exploration.

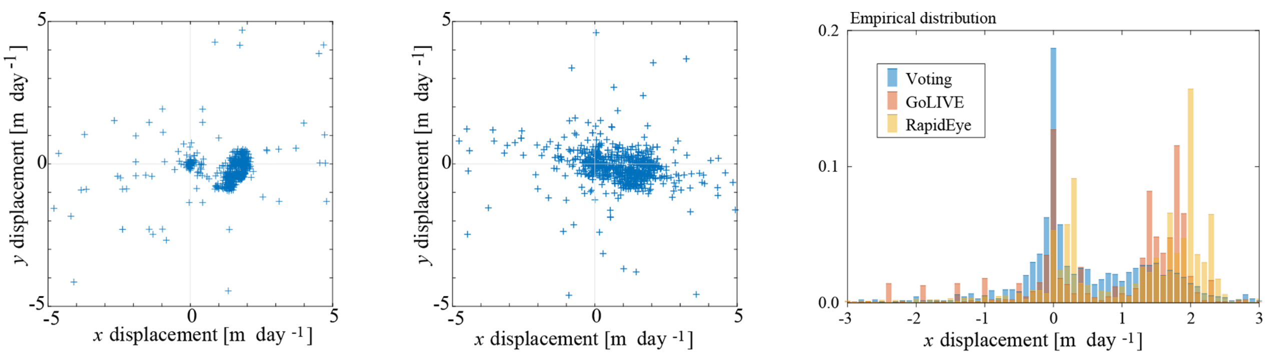

(a) Velocity distribution GoLIVE (b) Velocity distribution voting (c) Distribution x displacement

Figure 10. Panels **(a)** and **(b)** show the distribution of velocities for a section of Klutlan Glacier; their map views are shown in Fig. 9. In panel **(c)** the same x-component data as in Fig. 9 are shown, but now the distributions are shown.

be seen. Most clearly, the surge front seems to propagate downwards with a steady velocity but appears to slow down around the 50 km mark (see dashed line in Fig. 12a), as shown by the break in slope. Here, the glacier widens into a lobe at the terminus. This can suggest ice thickness is homogeneous here or ice thickness does not seem to play an important role in surge propagation.

At the end of the summer of 2016 the tributary just north of the 20 km mark of Klutlan Glacier seems to increase in speed. This can be confirmed by tracing the extent of the looped moraines, as in Fig. 12b. In the same imagery the medial moraines of the meeting point of all basins are mapped as well. Here, the moraine bands before and after the event align well at the junction, indicating a steady or similar contribution over the full period, or an insignificant effect, as the surge has not been developing into very fast flow. In contrast, the lower part of this glacial trunk has moraine bands that do not align.

The surge behavior we observe for Klutlan Glacier, especially the propagation, can be observed at other glaciers within the study area. For Fisher Glacier, a similar increase in speed is observed within the main trunk that later propagates downstream as well as upstream. This also seems to be the case for Walsh Glacier, where a speed increase in the eastern trunk leads to a surge on the northern trunk and a glacier-wide acceleration. On its way the fast-flowing ice initiates surges in tributaries downflow, but the surge extent also moves upslope and tributaries that were further up-glacier from the initial surge start to speed up. This is also seen for Steele Glacier, which develops a surge and Hodgson Glacier is later entrained into the fast flow as well.

These events are best observed with the help of an animation (see Supplement) but the initial identification was per-

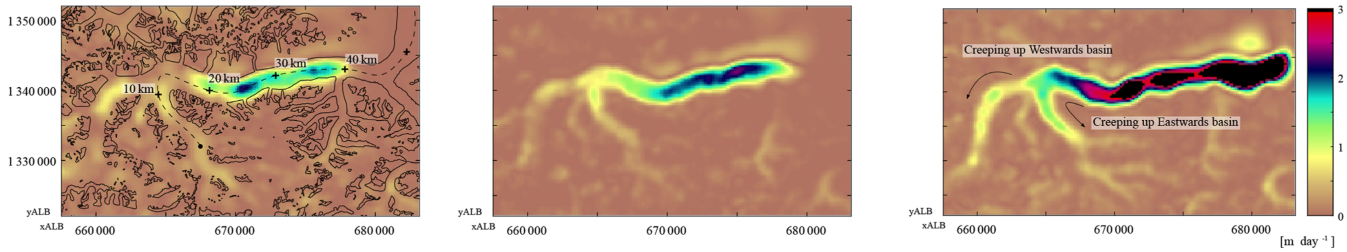

(a) 20 Jul 2014–21 Aug 2014 (b) 1 Mar 2015–2 Apr 2015 (c) 23 Jun 2016–25 Jul 2016

Figure 11. Snapshots of ice speeds at different time instances from a data compilation for the summer 2016 surge occurring on Klutlan Glacier (for location see Fig. 7). The used GoLIVE data configuration is shown in Fig. A1, and the data are from the smoothed dataset.

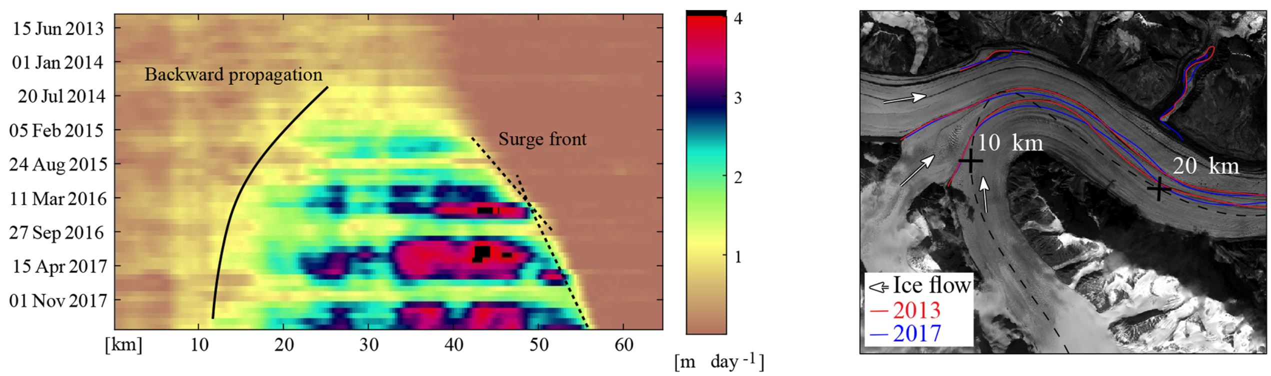

(a) Speed along flow line of Klutlan Glacier, line given in Figure 11a. (b) Moraine positions

Figure 12. The speed over the central flow line of Klutlan Glacier. The markings of this flow line are shown in panel **(a)**. In panel **(b)** the convergence of different basins of the Klutlan Glacier is shown; data are from a RapidEye acquisition on 5 September 2013 and 23 September 2017. For comparison the 2013 image is overlain with the two moraine positions.

formed through a simple visualization of the spread of flow speed (see Fig. 13). Here the surging glaciers stand out, as do most of the tidewater glaciers, which have a highly dynamic nature at their fronts. Dynamics in smaller tributaries are visible as well; for example, a tributary of the Chitina Glacier seems to have pushed itself into the main trunk within a 2-year time period; see Fig. C1 in Appendix C.

5 Discussion

Synthesized velocity time series estimated from our post-processing chain of GoLIVE image-pair velocity determinations are dependent on the number and distribution of measured displacements (see Appendix A). It may be possible to improve these time series in several ways. Surface features imaged in the same season have similar appearances, allowing good displacement fields to be produced from images which are a year apart, as is typical working practice (Heid and Kääb, 2012b; Dehecq et al., 2015). Annual displacements fields could be helpful when areas are cloud covered for long periods, as these estimates can function as gap fillers in the least-squares estimation. Because the adjustment model assigns equal weighting to individual displacements if no other information is available, some velocity changes might be missed or blurred in time. Such a drawback might be overcome with spatial constraints, such as an advection pattern imposed on the data, although this would increase the amount of post-processing.

Another limitation of our method concerns the glacier kinematics that are constrained by our model. In the current implementation the deviation (σ) is dependent on the time interval. From a measurement perspective this makes sense, but the model does not inherently account for speed change. For long time intervals the fuzzy function forces the deviation to become small. This reduces the ability to obtain a correct match when glacier-dynamics changes are occurring. It might be helpful to explore the improvement when a fixed deviation is set instead. In addition, low scores over glaciated terrain might indicate that the deviation of the displacement is set too tight. When this deviation is given higher bounds, the score increases, and such behavior can then be used as a meaningful measure.

The smoothing parameter used is a single global parameter that assumes isotropy. In order to fulfill this property the spatiotemporal data have been scaled accordingly. However, when severe data gaps are present, the velocity dataset still shows jumps. This will improve when more data are avail-

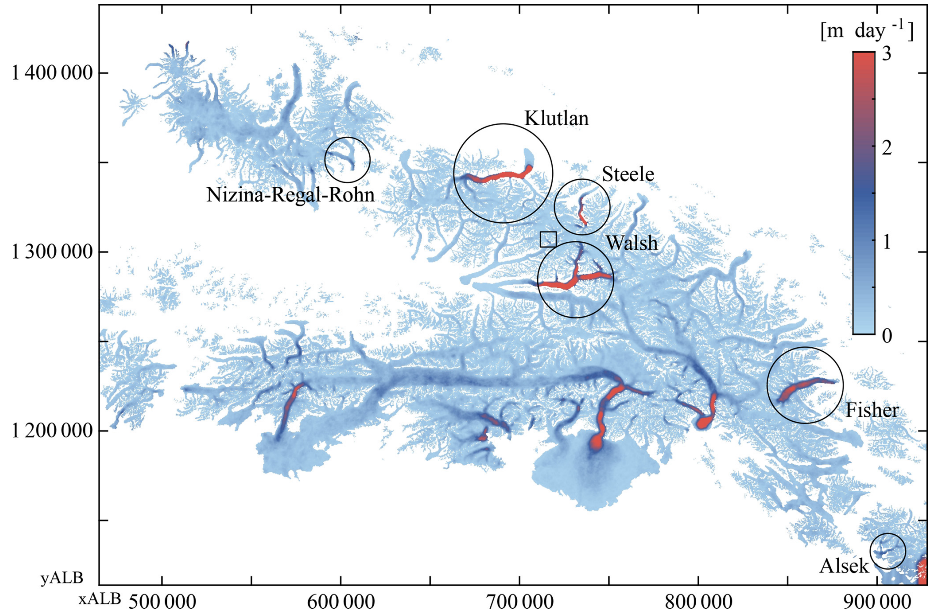

Figure 13. Spread of variation in flow speed (using the difference between the 20th and 80th percentiles) over the observed period (2013–2018). Different dynamic glaciers are encircled, and the square indicates the tributary glacier shown in Fig. C1.

able, for example by including Sentinel-2 data or incorporating across-track matching (Altena and Kääb, 2017a). An increase in votes will result in a better population of the vote space, as can be seen in Fig. 6. In addition, the voting score, that is, the consensus score in the Hough space, can be used as the initial weighting for the smoothing procedure (w in Eq. 2). This might reduce the number of iterations used by the robust smoother. Improvement can be made to the smoother, as our initial implementation has a simple neighborhood function and has no knowledge of glacier-specific properties.

The input data have some possibility of systematic effects that propagate into the synthesized velocity time series. PyCORR-generated displacement is based upon pattern matching methods applied to optical images. Normalized cross-correlation is most sensitive to large intensity variations within the image chips (Debella-Gilo and Kääb, 2011; Fahnestock et al., 2016). Thus specifically for glacierized regions, a low solar illumination angle in winter can cause the pattern matching to fix on shadow edges. Similarly, snow cover and melt-out edges (which occur in autumn and spring) can cause false correlations due to strong contrast in the image chips. To reduce these effects the GoLIVE correlator uses high-pass-filtered imagery (Scambos et al., 1992). Setting the scale of the filter is a subtle trade-off, as shading and shadowing of smaller surface topography are correlatable features and are particularly useful in low-sun-angle conditions (e.g., late fall–winter–early spring). In high-radiometry satellite instruments such as Landsat 8 (and 9), Sentinel 2, and WorldView, information is present in the imagery over shadow cast terrain (Kääb et al., 2016). Hence, in principle, frequency-based orientation correlation (Heid and Kääb, 2012a) might perform better for this specific issue.

6 Conclusions

In 5 years the increase in the number of high-quality optical satellite systems has made it possible to extract detailed and frequent velocity fields over glaciers, ice caps and ice sheets. The GoLIVE dataset is a repository of such velocity fields derived from Landsat 8, available at low latency for analysis by the community. Discovery and exploration of this resource can be complicated due to its vast and growing volume and the complexity of spatiotemporal changes of glacier flow fields. In this study we introduce an efficient post-processing scheme to combine ice velocity data from different overlapping time spans. The presented methodology is resistant to multiple outliers, as voting is used instead of testing. However, since cloud cover or changes in surface characteristics can hamper velocity estimation and spatial flow relations are not incorporated, the resulting synthesized time series still have gaps or outliers. We use a data-driven spatiotemporal smoother to address this issue and enhance the visualization of real glacier flow changes.

Our synthesized time series has a monthly (32 days) temporal interval and 300 m spatial resolution. The time series spans 2013 to 2018 and covers the Saint Elias Mountains and vicinity. Within this study area, we identify several surges of different glaciers at different times and their development over time can be observed. Such details can even be extracted for small tributary glaciers. More surprisingly, velocities for the snow-covered upper glacier areas are, in general, estimated accurately. Thus our synthesized time series can provide an overview of where and when interesting glacier dynamics are occurring.

This study is a demonstration of the capabilities of the new GoLIVE-type remote-sensing products combined with an advanced data filtering and interpolation scheme. We demonstrate that our method can be implemented with ease for a large region, covering several mountain ranges. The derived smoothed time series data contain many subtle additional changes that could be investigated. If this time series is combined with digital elevation model (DEM) time series (Wang and Kääb, 2015), it becomes possible to look at changes in ice mass in great detail.

The presented velocity time series has a high temporal dimension, especially with respect to the sensor 16-day orbit repeat cycle. Though temporal or spatial data gaps are still present (due to the short temporal interval, cloud cover or visual coherence loss) this might partly be addressed by enlarging the temporal resolution or through additional data, such as from Sentinel-2 (Altena and Kääb, 2017a). Fortunately, harmonization with other velocity datasets can be easily implemented because our procedure uses only geometric information and is not dependent on sensor type. With our framework it is thus possible to make a consistent time series composed of a patchwork of optical or SAR remote-sensing products.

Data availability. The Global Land Ice Velocity Extraction from Landsat 8 (GoLIVE) data are available at http://nsidc.org/data/golive (last access: 26 February 2019) (https://doi.org/10.7265/N5ZP442B, Scambos et al., 2016).

Appendix A: Velocity pairs used

The GoLIVE velocity fields used in this study are numerous. In order to obtain an overview of the data used, the velocity pairs are plotted as a network of edges through time, in Fig. A1. Every red arch corresponds to a displacement estimate over a certain period, with a specific footprint (a given path–row combination; see Fig. 1 for localization). The general statistics of the collection of used GoLIVE displacement pairs are given in the Table A1.

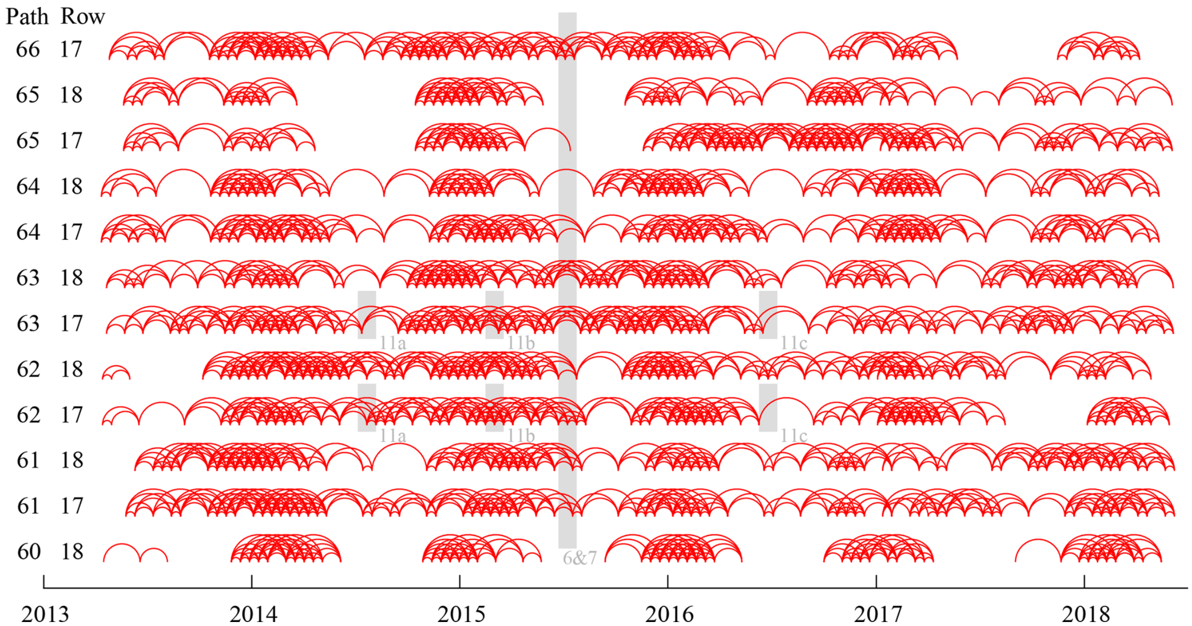

Figure A1. Node network of the velocity fields used in this study, a total of 2736 velocity fields. The gray bars span the time interval used for the generation of the different velocity products used in the figures in the main text. The specific numbering is given by their annotation, which is also in gray.

Table A1. Number of GoLIVE displacement products used in the generation of the product, ordered by location through path, row and by relative time interval.

Time interval	60	61		62		63		64		65		66	Path
in days ↓	18	17	18	17	18	17	18	17	18	17	18	17	Row
16	34	45	43	43	47	41	43	41	38	42	29	41	
32	34	40	37	46	49	46	39	38	34	40	27	39	
48	33	46	43	41	47	43	40	43	31	38	28	38	
64	27	47	42	41	42	44	40	36	26	38	25	38	
80	26	41	37	42	45	47	38	41	31	37	22	35	
96	21	38	38	38	43	42	40	40	35	30	21	35	

Appendix B: Corrections performed by smoothing

In the following section plots are given of speed variations over selected areas of interest; the locations are denoted in Fig. 11a by black crosses. Every plot has a box plot with the least-squares estimate of a selection of observations. This selection was made through consensus, by voting as described in the paper. The gray lines indicate the smoothed spatiotemporal velocity. These are multiple lines, as not one estimate is used, but a surrounding area of a 5×5 pixel wide neighborhood is taken. This is carried out in order to have sufficient data points and see the spread of the observations and the influence of the smoother. A comparison between both estimated and smoothed versions is shown in the right graph of each figure, where the white line indicates the 1 : 1.

Figure B3 shows the velocity evolution of the ocean-terminating part of Hubbard Glacier (see Fig. 7 for specific localization). This glacier is seen from paths 61 and 62 and is in row 18. Data come from the GoLIVE dataset and an open configuration is used for the estimation of the velocity. Aliasing occurs in both the slow-moving part (0–4 km) and the fast-moving part (5–7 km). The availability of displacement data from GoLIVE is highest in the winter, as can be seen in Fig. A1. Late in 2015 the Hubbard Glacier seems to slow down completely. However, at the same period the number of GoLIVE displacement data is relatively sparse. When a lack of data occurs, it is very difficult to establish consensus and extract information. To some degree this seems to occur for other years in autumn as well.

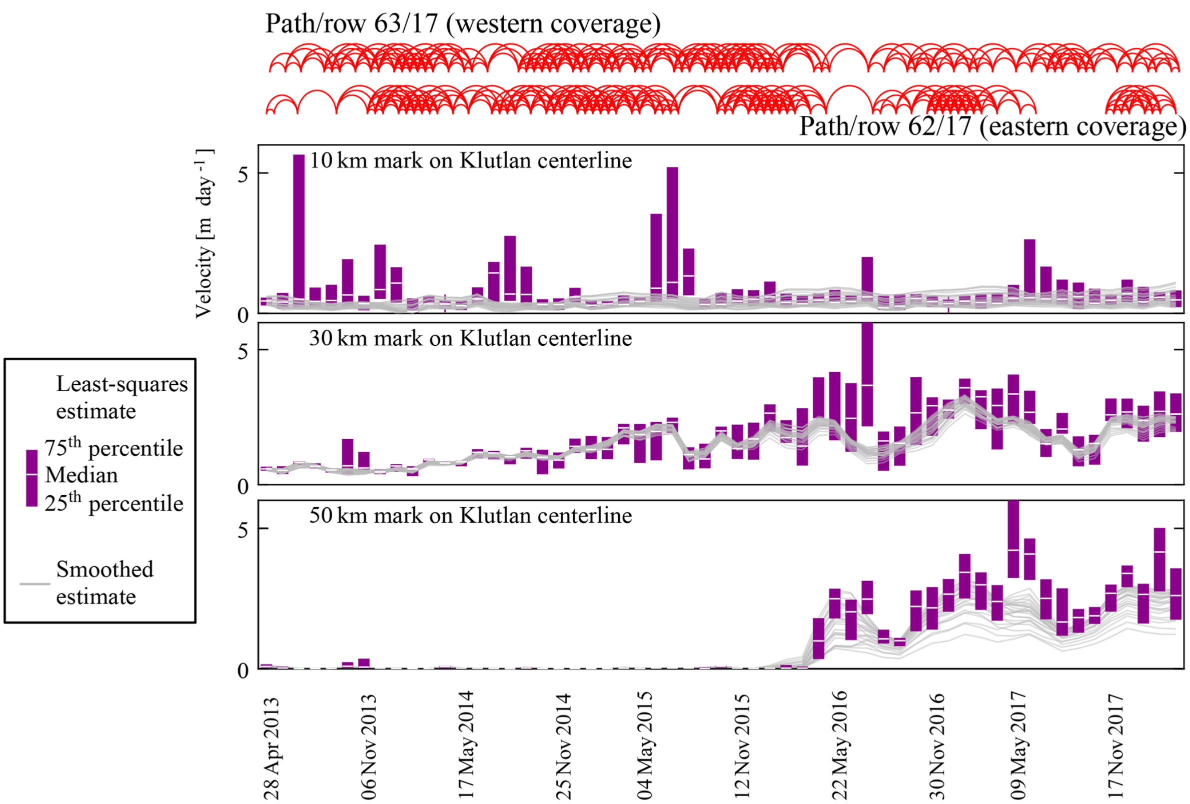

Figure B1. Temporal evolution of three locations along the flow line of Klutlan Glacier. The data from the specific marker and its direct neighborhood are shown. In purple is the box plot of these data while in gray the smoothed estimates are plotted. For the location of the reference marks, please see Fig. 11a. Above the figures, the network configuration of the GoLIVE data for the two covering Landsat scenes is given.

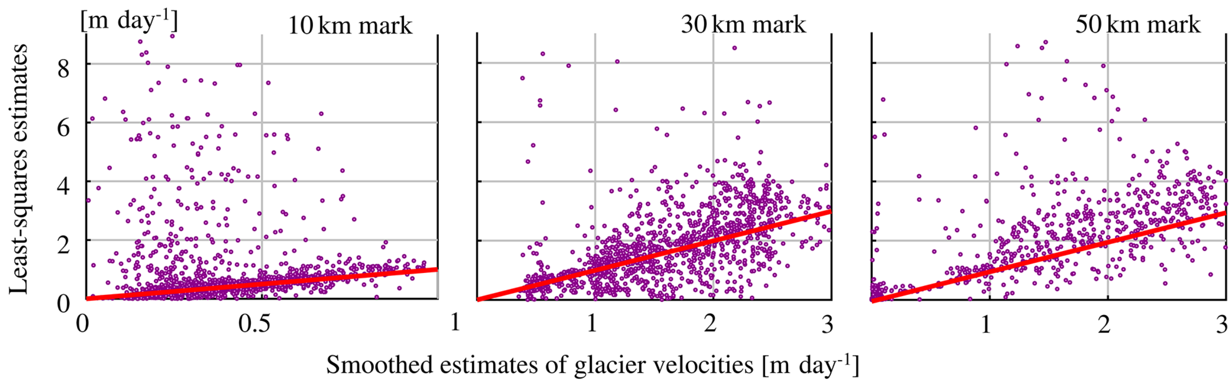

Figure B2. The temporal data shown in Fig. B1 are combined and the least-squares consensus is plotted against the smoothed estimate. The slanted line in all figures corresponds to the 1 : 1 line.

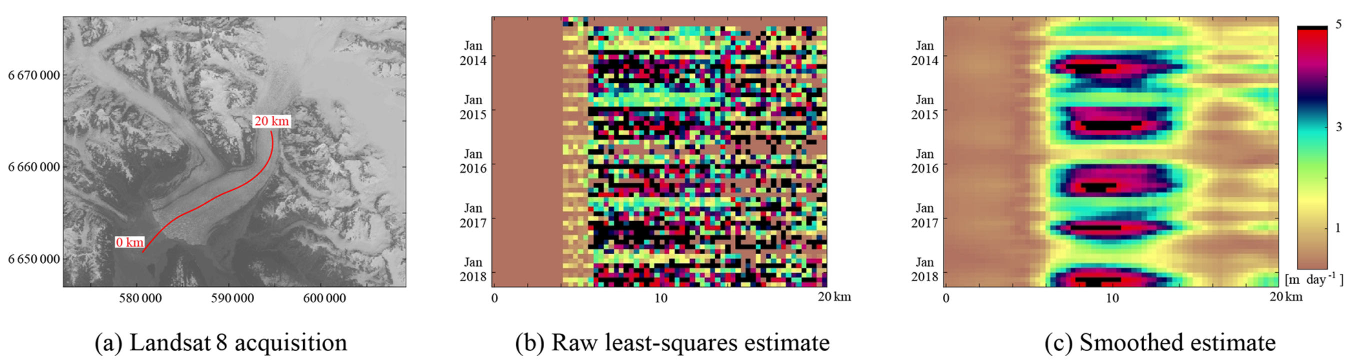

Figure B3. (a) Landsat 8 acquisition on 5 September 2013 over Hubbard Glacier; in red is the centerline used for the sampling which is plotted in panels **(b)** and **(c)**. **(b)** Velocity estimates using the data of displacements that had consensus during the voting step. **(c)** Smoothed estimate of velocity evolution over time, using spatial and temporal data and assisted by an off-glacier mask.

Appendix C: Tributary dynamics

From the constructed multi-temporal time series the variance of a low and high quantile can be estimated. This gives an overview of ice masses with a highly dynamic nature. Through this simple analysis, an unknown tributary surge was identified. The push of this tributary into the medial moraine and its velocity record over time can be seen in Fig. C1.

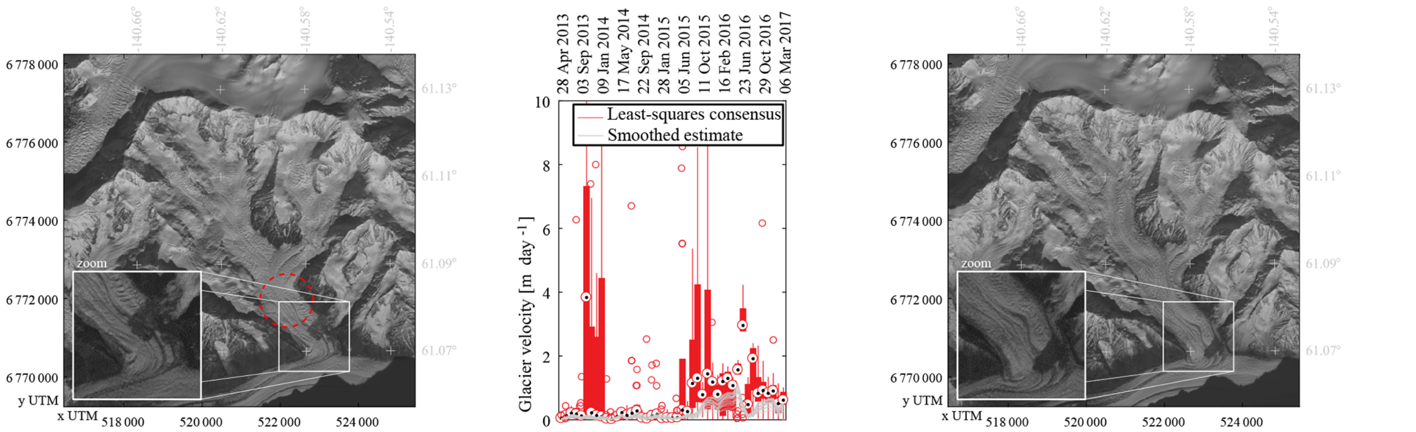

(a) 24 Sep 2014 (b) Estimated velocities (c) 23 Sep 2017

Figure C1. A tributary of Chitina Glacier surged in the period 2015–2016. Images are both acquired by Landsat 8; its location is indicated by a square in Fig. 13. The location of the time series in panel **(b)** is indicated by a red dashed circle in panel **(a)**.

Supplement. The supplement related to this article is available online at: https://doi.org/10.5194/tc-13-795-2019-supplement.

Author contributions. BA led the development of this study. All authors discussed the results and commented on the paper at all stages.

Competing interests. The authors declare that they have no conflict of interest.

Acknowledgements. This work was initiated during the International Summer School in Glaciology in Alaska, organized by the University of Alaska Fairbanks. The research of Bas Altena and Andreas Kääb was conducted through support from the European Union FP7 ERC project ICEMASS (320816) and the ESA projects Glaciers_cci (4000109873 14 I-NB) and ICEFLOW (4000125560 18 I-NS). This work was supported by USGS award G12PC00066. The GoLIVE data processing and distribution system is supported by NASA Cryosphere award NNX16AJ88G. The authors are grateful to Planet Labs Inc. for providing RapidEye satellite data for this study via Planet's Ambassadors Program. We would like to thank editor Bert Wouters and the four reviewers for their constructive feedback.

Edited by: Bert Wouters
Reviewed by: four anonymous referees

References

Abe, T. and Furuya, M.: Winter speed-up of quiescent surge-type glaciers in Yukon, Canada, The Cryosphere, 9, 1183–1190, https://doi.org/10.5194/tc-9-1183-2015, 2015.

Abe, T., Furuya, M., and Sakakibara, D.: Brief Communication: Twelve-year cyclic surging episodes at Donjek Glacier in Yukon, Canada, The Cryosphere, 10, 1427–1432, https://doi.org/10.5194/tc-10-1427-2016, 2016.

Altena, B. and Kääb, A.: Elevation change and improved velocity retrieval using orthorectified optical satellite data from different orbits, Remote Sensing, 9, 300, https://doi.org/10.3390/rs9030300, 2017a.

Altena, B. and Kääb, A.: Weekly glacier flow estimation from dense satellite time series using adapted optical flow technology, Front. Earth Sci., 5, 53 pp., https://doi.org/10.3389/feart.2017.00053, 2017b.

Arendt, A., Luthcke, S., Gardner, A., O'neel, S., Hill, D., Moholdt, G., and Abdalati, W.: Analysis of a GRACE global mascon solution for Gulf of Alaska glaciers, J. Glaciol., 59, 913–924, https://doi.org/10.3189/2013JoG12J197, 2013.

Arendt, A. A.: Assessing the status of Alaska's glaciers, Science, 332, 1044–1045, https://doi.org/10.1126/science.1204400, 2011.

Armstrong, W. H., Anderson, R. S., and Fahnestock, M. A.: Spatial patterns of summer speedup on South central Alaska glaciers, Geophys. Res. Lett., 44, 1–10, https://doi.org/10.1002/2017GL074370, 2017.

Baarda, W.: A testing procedure for use in geodetic networks, vol. 2, Publications on Geodesy, Rijkscommissie voor Geodesie, 1968.

Berthier, E., Schiefer, E., Clarke, G. K., Menounos, B., and Rémy, F.: Contribution of Alaskan glaciers to sea-level rise derived from satellite imagery, Nat. Geosci., 3, 92–95, https://doi.org/10.1038/ngeo737, 2010.

Bieniek, P. A., Bhatt, U. S., Thoman, R. L., Angeloff, H., Partain, J., Papineau, J., Fritsch, F., Holloway, E., Walsh, J. E., Daly, C., Shulski, M., Hufford, G., Hill, D. F., Calos, S., and Gens, R.: Climate divisions for Alaska based on objective methods, J. Appl. Meteorol. Clim., 51, 1276–1289, https://doi.org/10.1175/JAMC-D-11-0168.1, 2012.

Burgess, E. W., Forster, R. R., Larsen, C. F., and Braun, M.: Surge dynamics on Bering Glacier, Alaska, in 2008–2011, The Cryosphere, 6, 1251–1262, https://doi.org/10.5194/tc-6-1251-2012, 2012.

Burgess, E. W., Forster, R. R., and Larsen, C. F.: Flow velocities of Alaskan glaciers, Nat. Commun., 4, 2146, https://doi.org/10.1038/ncomms3146, 2013.

Clarke, G. K. and Holdsworth, G.: Glaciers of the St. Elias mountains, US Geological Survey professional paper, in: Satellite Image Atlas of Glaciers of the World – North America, edited by: Williams, R. S. and Ferrigno, J. G., USGS Professional Paper 1386-J2002, 2002.

Copland, L., Pope, S., Bishop, M. P., Shroder, J. F., Clendon, P., Bush, A., Kamp, U., Seong, Y. B., and Owen, L. A.: Glacier velocities across the central Karakoram, Ann. Glaciol., 50, 41–49, https://doi.org/10.3189/172756409789624229, 2009.

Debella-Gilo, M. and Kääb, A.: Sub-pixel precision image matching for measuring surface displacements on mass movements using normalized cross-correlation, Remote Sens. Environ., 115, 130–142, https://doi.org/10.1016/j.rse.2010.08.012, 2011.

Dehecq, A., Gourmelen, N., and Trouvé, E.: Deriving large-scale glacier velocities from a complete satellite archive: Application to the Pamir–Karakoram–Himalaya, Remote Sens. Environ., 162, 55–66, https://doi.org/10.1016/j.rse.2015.01.031, 2015.

Fahnestock, M., Scambos, T., Moon, T., Gardner, A., Haran, T., and Klinger, M.: Rapid large-area mapping of ice flow using Landsat 8, Remote Sens. Environ., 185, 84–94, https://doi.org/10.1016/j.rse.2015.11.023, 2016.

Fatland, D. R. and Lingle, C. S.: InSAR observations of the 1993–95 Bering Glacier (Alaska, USA) surge and a surge hypothesis, J. Glaciol., 48, 439–451, https://doi.org/10.3189/172756502781831296, 2002.

Fischler, M. A. and Bolles, R. C.: Random sample consensus: a paradigm for model fitting with applications to image analysis and automated cartography, Commun. ACM, 24, 381–395, https://doi.org/10.1145/358669.358692, 1981.

Garcia, D.: Robust smoothing of gridded data in one and higher dimensions with missing values, Comput. Stat. Data An., 54, 1167–1178, https://doi.org/10.1016/j.csda.2009.09.020, 2010.

Han, J., Kóczy, L., and Poston, T.: Fuzzy Hough transform, Pattern Recogn. Lett., 15, 649–658, https://doi.org/10.1016/0167-8655(94)90068-X, 1994.

Harig, C. and Simons, F. J.: Ice mass loss in Greenland, the Gulf of Alaska, and the Canadian Archipelago: Seasonal cycles and decadal trends, Geophys. Res. Lett., 43, 3150–3159, https://doi.org/10.1002/2016GL067759, 2016.

Heid, T. and Kääb, A.: Evaluation of existing image matching methods for deriving glacier surface displacements globally from optical satellite imagery, Remote Sens. Environ., 118, 339–355, https://doi.org/10.1016/j.rse.2011.11.024, 2012a.

Heid, T. and Kääb, A.: Repeat optical satellite images reveal widespread and long term decrease in land-terminating glacier speeds, The Cryosphere, 6, 467–478, https://doi.org/10.5194/tc-6-467-2012, 2012b.

Herreid, S. and Truffer, M.: Automated detection of unstable glacier flow and a spectrum of speedup behavior in the Alaska Range, J. Geophys. Res.-Earth, 121, 64–81, https://doi.org/10.1002/2015JF003502, 2016.

Jeong, S., Howat, I. M., and Ahn, Y.: Improved multiple matching method for observing glacier motion with repeat image feature tracking, IEEE T. Geosci. Remote, 55, 2431–2441, https://doi.org/10.1109/TGRS.2016.2643699, 2017.

Kääb, A. and Vollmer, M.: Surface geometry, thickness changes and flow fields on creeping mountain permafrost: automatic extraction by digital image analysis, Permafrost Periglac., 11, 315–326, https://doi.org/10.1002/1099-1530(200012)11:4<315::AID-PPP365>3.0.CO;2-J, 2000.

Kääb, A., Winsvold, S. H., Altena, B., Nuth, C., Nagler, T., and Wuite, J.: Glacier remote sensing using Sentinel-2. part I: Radiometric and geometric performance, and application to ice velocity, Remote Sensing, 8, 598, https://doi.org/10.3390/rs8070598, 2016.

Kolaas, J.: Getting started with HydrolabPIV v1.0, Research report in mechanics 2016:01, University of Oslo, http://urn.nb.no/URN:NBN:no-53997 (last access: 26 February 2019), 2016.

Maksymiuk, O., Mayer, C., and Stilla, U.: Velocity estimation of glaciers with physically-based spatial regularization. Experiments using satellite SAR intensity images, Remote Sens. Environ., 172, 190–204, https://doi.org/10.1016/j.rse.2015.11.007, 2016.

Meier, M. F. and Post, A.: What are glacier surges?, Can. J. Earth Sci., 6, 807–817, https://doi.org/10.1139/e69-081, 1969.

Melkonian, A. K., Willis, M. J., and Pritchard, M. E.: Satellite-derived volume loss rates and glacier speeds for the Juneau Icefield, Alaska, J. Glaciol., 60, 743–760, https://doi.org/10.3189/2014JoG13J181, 2014.

Molnia, B. F.: Glaciers of Alaska, Alaska Geographic Society, USGS Professional Paper 1386-K, https://doi.org/10.3133/pp1386K, 2008.

Moon, T., Joughin, I., Smith, B., Broeke, M. R., Berg, W. J., Noël, B., and Usher, M.: Distinct patterns of seasonal Greenland glacier velocity, Geophys. Res. Lett., 41, 7209–7216, https://doi.org/10.1002/2014GL061836, 2014.

Muskett, R. R., Lingle, C. S., Tangborn, W. V., and Rabus, B. T.: Multi-decadal elevation changes on Bagley ice valley and Malaspina glacier, Alaska, Geophys. Res. Lett., 30, 1857, https://doi.org/10.1029/2003GL017707, 2003.

Paul, F., Bolch, T., Kääb, A., Nagler, T., Nuth, C., Scharrer, K., Shepherd, A., Strozzi, T., Ticconi, F., Bhambri, R., Berthier, E., Bevan, S., Gourmelen, N., Heid, T., Jeong, S., Kunz, M., Lauknes, T. R., Luckman, A., Boncori, J. P. M., Moholdt, G., Muir, A., Neelmeijer, J., Rankl, M., VanLooy, J., and Van Niel, T.: The glaciers climate change initiative: Methods for creating glacier area, elevation change and velocity products, Remote Sens. Environ., 162, 408–426, https://doi.org/10.1016/j.rse.2013.07.043, 2015.

Paul, F., Strozzi, T., Schellenberger, T., and Kääb, A.: The 2015 Surge of Hispar glacier in the Karakoram, Remote Sensing, 9, 888, https://doi.org/10.3390/rs9090888, 2017.

Pfeffer, W. T., Arendt, A. A., Bliss, A., Bolch, T., Cogley, J. G., Gardner, A. S., Hagen, J.-O., Hock, R., Kaser, G., Kienholz, C., Miles, E., Moholdt, G., Mölg, N., Paul, F., Radić, V., Rastner, P., Raup, B. R., Rich, J., Sharp, M. J., and the Randolph consortium: The Randolph Glacier Inventory: a globally complete inventory of glaciers, J. Glaciol., 60, 537–552, 2014.

Post, A.: Distribution of surging glaciers in western North America, J. Glaciol., 8, 229–240, https://doi.org/10.3189/S0022143000031221, 1969.

Quincey, D., Braun, M., Glasser, N., Bishop, M., Hewitt, K., and Luckman, A.: Karakoram glacier surge dynamics, Geophys. Res. Lett., 38, 504, https://doi.org/10.1029/2011GL049004, 2011.

Rosenau, R., Scheinert, M., and Dietrich, R.: A processing system to monitor Greenland outlet glacier velocity variations at decadal and seasonal time scales utilizing the Landsat imagery, Remote Sens. Environ., 169, 1–19, https://doi.org/10.1016/j.rse.2015.07.012, 2015.

Rosenau, R., Scheinert, M., and Ebermann, B.: Velocity fields of Greenland outlet glaciers, Technische Universität Dresden, Germany, available at: http://data1.geo.tu-dresden.de/flow_velocity/ (last access: 26 February 2019), 2016.

Rousseeuw, P. and Leroy, A.: Robust regression and outlier detection, vol. 589, John wiley & sons, https://doi.org/10.1002/0471725382, 2005.

Roy, D., Wulder, M., Loveland, T., Woodcock, C., Allen, R., Anderson, M., Helder, D., Irons, J., Johnson, D., Kennedy, R., Scambos, T., Schaaf, C., Schott, J., Sheng, Y., Vermote, E., Belward, A., Bindschadler, R., Cohen, W., Gao, F., Hipple, J., Hostert, P., Huntington, J., Justice, C., Kilic, A., Kovalskyy, V., Lee, Z., Lymburner, L., Masek, J., McCorkel, J., Shuai, Y., Trezza, R., Vogelmann, J., Wynne, R., and Zhu, Z.: Landsat-8: Science and product vision for terrestrial global change research, Remote Sens. Environ., 145, 154–172, https://doi.org/10.1016/j.rse.2014.02.001, 2014.

Scambos, T., Dutkiewicz, M., Wilson, J., and Bindschadler, R.: Application of image cross-correlation to the measurement of glacier velocity using satellite image data, Remote Sens. Environ., 42, 177–186, https://doi.org/10.1016/0034-4257(92)90101-O, 1992.

Scambos, T., Fahnestock, M., Moon, T., Gardner, A., and Klinger, M.: Global Land Ice Velocity Extraction from Landsat 8 (GoLIVE), Version 1, NSIDC: National Snow and Ice Data Center, Boulder, Colorado USA, https://doi.org/10.7265/N5ZP442B, http://nsidc.org/data/golive (last access: 26 February 2019), 2016.

Scherler, D., Leprince, S., and Strecker, M. R.: Glacier-surface velocities in alpine terrain from optical satellite imagery – Accuracy improvement and quality assessment, Remote Sens. Environ., 112, 3806–3819, https://doi.org/10.1016/j.rse.2008.05.018, 2008.

Skvarca, P.: Changes and surface features of the Larsen Ice Shelf, Antarctica, derived from Landsat and Kosmos mosaics, Ann. Glaciol., 20, 6–12, https://doi.org/10.3189/172756494794587140, 1994.

Strang, G. and Borre, K.: Linear algebra, geodesy and GPS, Wellesley-Cambridge Press, 1997.

Teunissen, P.: Testing theory, Series on Mathematical Geodesy and Positioning, Delft Academic Press, 2000.

Turrin, J., Forster, R. R., Larsen, C., and Sauber, J.: The propagation of a surge front on Bering glacier, Alaska, 2001–2011, Ann. Glaciol., 54, 221–228, https://doi.org/10.3189/2013AoG63A341, 2013.

Van Wychen, W., Copland, L., Jiskoot, H., Gray, L., Sharp, M., and Burgess, D.: Surface velocities of glaciers in Western Canada from speckle-tracking of ALOS PALSAR and RADARSAT-2 data, Can. J. Remote Sens., 44, 57–66, https://doi.org/10.1080/07038992.2018.1433529, 2018.

Wackernagel, H.: Multivariate geostatistics: An introduction with applications, Springer Science & Business Media, https://doi.org/10.1007/978-3-662-05294-5, 2013.

Waechter, A., Copland, L., and Herdes, E.: Modern glacier velocities across the Icefield Ranges, St Elias Mountains, and variability at selected glaciers from 1959 to 2012, J. Glaciol., 61, 624–634, https://doi.org/10.3189/2015JoG14J147, 2015.

Wang, D. and Kääb, A.: Modeling glacier elevation change from DEM time series, Remote Sensing, 7, 10117–10142, https://doi.org/10.3390/rs70810117, 2015.

Westerweel, J. and Scarano, F.: Universal outlier detection for PIV data, Exp. Fluids, 39, 1096–1100, https://doi.org/10.1007/s00348-005-0016-6, 2005.